ON THE UNCERTAINTY QUANTIFICATION AND NON-LINEAR HYPER ELASTIC SIMULATION OF BIOLOGICAL TISSUES

By

Behrouz Shamsaei

James C. Newman III
Professor of Computational Engineering
(Chair)

William K. Anderson
Professor of Computational Engineering
(Committee Member)

Abdollah Arabshahi
Research Professor of Computational Engineering
(Committee Member)

John V. Matthews, III
Associate Professor of Mathematics
(Committee Member)

ON THE UNCERTAINTY QUANTIFICATION AND NON-LINEAR HYPER ELASTIC SIMULATION OF BIOLOGICAL TISSUES

By

Behrouz Shamsaei

A Dissertation Submitted to the Faculty of the University
of Tennessee at Chattanooga in Partial Fulfillment of
the Requirements of the Degree of Doctor of
Philosophy in Computational Engineering

The University of Tennessee at Chattanooga
Chattanooga, Tennessee

August 2016

ABSTRACT

In this dissertation, a computational structural mechanics capability is developed for the simulation of biological tissues. These tissues may exhibit either linear or nonlinear material responses and, therefore, the resultant theory and computational implementation are presented. Various discretization methods of the systems of equations are possible, and in the current work Continuous Galerkin (CG) and the Discontinuous Galerkin (DG) approaches are employed. Additionally, due to natural variations in biophysical properties from person to person, uncertainty quantification may be used to ascertain the impact on deterministic simulation results when assuming mean values of these properties. To this end, a hyper elastic formulation for the nonlinear, transversely isotropic behavior of soft and hard tissue is utilized for the simulation and failure analysis of the proximal femur. Both linear and nonlinear material results are compared. The uncertainty in the failure analysis due to the selected biophysical properties is then examined using the First-Order Second-Moment (FOSM) method. Additionally, within Computational Fluid Dynamics (CFD) it is often necessary to adaptively move the mesh (e.g. moving boundary simulations, shape design optimization, generation of higher-order grids near curved boundaries, etc.). In these regards, linear elasticity is commonly used for adaptation by viewing the mesh as a solid. In some cases, such as for anisotropic meshes or for extremely large boundary movement, this approach to mesh movement has experienced difficulties in producing valid grids for simulation purposes. Thus,

using the developed capability, the potential benefits of utilizing nonlinear material behavior for mesh movement is additionally examined.

DEDICATION

This work is dedicated to my lovely wife, Faranak that stood with me during this journey, to my precious parents, for their encouragement and support, and to my future kid/s that I may or may not have for giving me this motivation for working hard.

ACKNOWLEDGEMENTS

I use this opportunity to express my gratitude to my adviser, Dr. James C. Newman, for his friendly guidance and support during my research. Besides my advisor, I would like to express my deepest appreciation to Dr. Timothy W. Swafford who provided me the possibility to work at the SimCenter. I would like to thank the rest of my thesis committee, Dr. William Kyle Anderson, Dr. Mat Matthews, and Dr. Abi Arabshahi, for their insightful comments and encouragement. I thank my fellow friends Dr. Arash Ghasemi and Dr. Ethan Hereth for the stimulating discussions and the good times we had. Also I thank my wife Dr. Faranak Behzadi for all the support she provided for me during my research and my life. I would like to thank Dr. Georg N. Duda from Julius Wolff Institute and Berlin-Brandenburg, Center for Regenerative Therapies, for proving the loading data of femur during the gait cycle.

TABLE OF CONTENTS

CHAPTER

APPENDIX

LIST OF TABLES

LIST OF FIGURES

LIST OF SYMBOLS

Ω,	Computational domain
$\partial\Omega$,	Boundary of computational domain
$\partial\Omega_N$,	Neumann Boundary of computational domain
$\partial\Omega_D$,	Dirichlet Boundary of computational domain
$\partial\Omega_i$,	Union of interior edges
$\boldsymbol{F}$,	body force scalar or vector
κ,	A coefficient in Poisson equation
u,	Deformation scalar or vector
u_D,	Deformation on Dirichlet boundary conditions
u_N,	Deformation on Neumann boundary conditions
d,	Dimension
E,	interval, triangle or tetrahedron
$V(\mathcal{T}_h)$,	Defined broken space
$\Sigma(\mathcal{T}_h)$,	Defined broken space
$P(E)$,	Polynomial space
$\bar{\sigma}$,	Auxiliary trace of stress
q,	Auxiliary coefficient or vector
w,	Auxiliary variable
v,	Auxiliary variable
τ,	Auxiliary vector
$\mathbf{n}$,	Normal vector

$\hat{u}$,	Numerical flux
$\hat{\sigma}$,	Numerical flux
[.],	Jump operator
{.},	Average operator
dx,	Differential space
ds,	Differential distance
α,	A constant coefficient
η,	Penalty term
$\mathbf{x}$,	Auxiliary vector
$\mathbf{y}$,	Auxiliary vector
$\mathbf{M}$,	Auxiliary matrix
Ψ,	Helmholtz free energy
$\bar{w}$,	energy density function
$\bar{d}$,	Variation operator
C,	Right Cauchy-Green deformation tensor
B,	Left Cauchy-Green deformation tensor
F,	Deformation gradient tensor
x,	Deformed configuration
X,	Un-deformed configuration
η,	Eulerian/Almansi strain tensor
γ,	Lagrangian/Green strain tensor
ε,	Infinitesimal strain tensor
PK^2,	Second Piloa-Kirchhoff stress tensor
S,	Second Piloa-Kirchhoff stress tensor
PK^1,	First Piloa-Kirchhoff stress tensor
P,	First Piloa-Kirchhoff stress tensor

σ,	Cauchy stress tensor
f,	Force vector
A,	Area in un-deformed configuration
a,	Area in deformed configuration
$\boldsymbol{N}$,	Unit normal in un-deformed configuration
$\boldsymbol{n}$,	Unit normal in deformed configuration
K,	Stiffness tensor
λ,	First Lame constant
μ,	Second Lame constant
G,	Shear modulus
E,	Young modulus
ν,	Poisson’s ratio
J,	Jacobian of element
J_e,	Jacobian of face
W,	Weight of Gauss point in element integration
W_e,	Weight of Gauss point in face integration
δ,	Kronecker operator/variation operator
R,	Residual
$\mathcal{T}$,	Subdivision of domain
l,	Velocity gradient tensor
$\bar{v}$,	Volume in Eulerian coordinate
$\bar{V}$,	Volume in Lagrangian coordinate
I,	Identity tensor

CHAPTER 1

INTRODUCTION

Constitutive laws are essential for studying the mechanical behavior and simulation of physical materials. These equations are defined to represent the response of a material due to applied loading. Elasticity equations utilize a particular form of these constitutive equations, and are used for simulation and computational prototyping. Whether linear or non-linear, elasticity equations are used in a large number of computational fluid and structural problems. For these reasons, this dissertation is devoted to investigate some implementation schemes and applications of linear and non-linear elasticity equations. The fundamentals of continuum mechanics in solid structures are introduced and elasticity equations for linear and non-linear materials are discussed in a general manner. Then, finite element discretization and analysis for elasticity equations are investigated. Subsequently, some applications of these equations in mesh deformation and simulation of large strain materials such as biological tissues are investigated.

The outline of this dissertation is as follows: the fundamentals of elasticity equations in solid structures are discussed in the chapter(2) where the equations are derived in a general framework of minimization of total potential function. The difference between the linear and non-linear elasticity is further investigated by defining different potential functions.

In chapter(3), two different schemes for computational implementation of linear elasticity in a finite element framework, i.e. Continuous Galerkin (CG) and Discontinuous Galerkin (DG) are discussed.

Elastic materials are often formulated in the Lagrangian frame of reference and this concept is used in the mesh deformation procedure in computational fluid dynamics when there is a need to modify the mesh. Hence, chapter(4) is dedicated to comparing the linear and non-linear elasticity algorithms in a mesh deformation procedure.

Biological soft tissues such as muscles and flesh, and hard tissues like bones show highly non-linear and anisotropic mechanical properties. These materials are inherently non-linear and often show different behavior in the fiber direction as opposed to the direction normal to fibers. This phenomenon is addressed in chapter(5) and linear and non-linear elasticity relations for these problems are described for simulation of the proximal femur.

Biological parameters in the human anatomy are distributed data, thus the chapter(6) is devoted to take into account this distribution of data. Equations of failure in the proximal femur during the gait cycle are investigated. Uncertainty quantification is used to quantify the failure results in the proximal femur based on unknown or distributed biological parameters. Summary of this research and suggestions about the extension of this work is provided in the last chapter.

CHAPTER 2

FUNDAMENTAL OF LINEAR AND NONLINEAR ELASTICITY

Elasticity equations represent the conservation of momentum and are mathematically similar to Poisson equation with the difference being these are coupled multi-variable second order boundary value equations. In the next section some fundamental background material concerning elasticity, from continuum mechanics perspective, are reviewed.

2.1 Deriving elasticity relation from fundamentals of continuum mechanics

The solution of the deformation of materials under internal and external forces and boundary conditions is obtained when the total deformation energy Ψ of the domain is minimized. In structural mechanics this energy functional is referred to as Helmholtz free energy; the deformation energy density or deformation energy density function $\bar{w}$ is defined as

$$\Psi = \int_{\Omega} \bar{w} \, d\Omega \tag{2.1}$$

The material is at rest when the variation of Ψ vanishes, meaning $\delta\left(\Psi\right) = 0$.

2.1.1 Strain tensors

Deformation energy density $\bar{w}$ depends on the local deformation of the material and the local material properties, so to define the dependency of $\bar{w}$ to deformation, the deformation gradint tensor F is introduced as

$$\mathrm{F}_{i,j} = \frac{\partial x_i}{\partial X_j} \tag{2.2}$$

where x_i and X_j are the components of deformed coordinate (*Eulerian*) and original undeformed reference coordinate (*Lagrangian*), respectively. Figure(2.1) illustrates the undeformed and deformed configurations and the respective coordinate systems for a continuum particle.

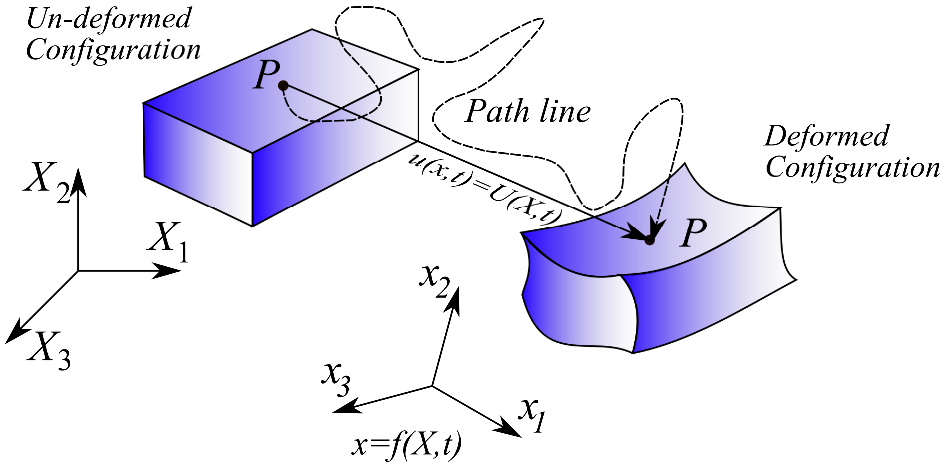

Figure 2.1 Deformation of continuum particle

The Right Cauchy-Green deformation tensor C and the left Cauchy-Green deformation tensor B are expressed as

$$\mathrm{C} = \mathrm{F}^{T}\mathrm{F}, \quad \mathrm{B} = \mathrm{F}\mathrm{F}^{\mathrm{T}} \tag{2.3}$$

These definitions are used to define the strain tensors in the Lagrangian and Eulerian coordinates. Large or finite strain tensor is the measure of change in the length of material $ds^2 = dx^2 - dX^2$ with respect to dx^2 or dX^2. These measures, and resultant displacements, are depicted in figure(2.2). The *Eulerian/Almansi* strain tensor η and *Lagrangian/Green* strain tensor γ can be written as

$$\gamma = \frac{1}{2}(\mathrm{C} - I), \quad \eta = \frac{1}{2}(\mathrm{I} - \mathrm{B}^{-1}) \tag{2.4}$$

The strain tensors can be written as a function of displacement $u = x - X$ as well.

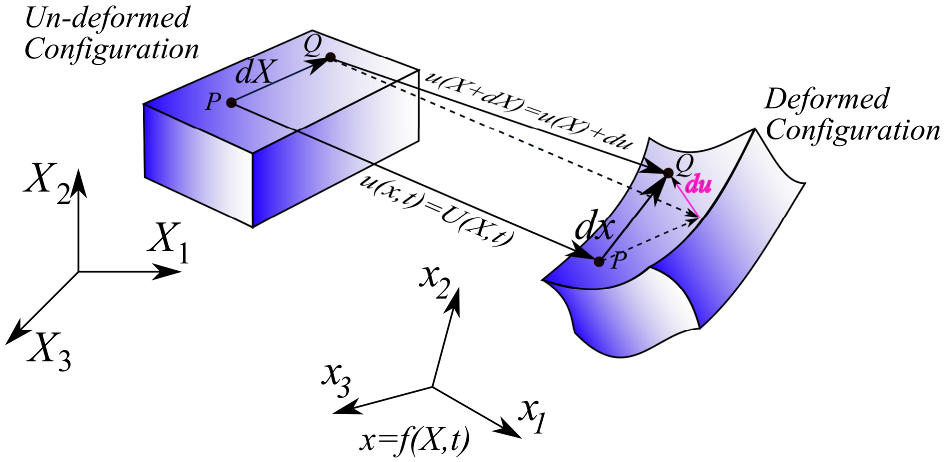

Figure 2.2 Displacement of continuum particle

After algebraic manipulation the Eulerian and Lagrangian strain tensors in terms of displacement gradients become

$$\gamma = \frac{1}{2}\left(\frac{\partial u_i}{\partial X_j} + \frac{\partial u_j}{\partial X_i} + \frac{\partial u_k}{\partial X_i}\frac{\partial u_k}{\partial X_j}\right), \quad \eta = \frac{1}{2}\left(\frac{\partial u_i}{\partial x_j} + \frac{\partial u_j}{\partial x_i} - \frac{\partial u_k}{\partial x_i}\frac{\partial u_k}{\partial x_j}\right) \tag{2.5}$$

Considering the principle of material frame indifference for isotropic materials results in the strain energy density function depending only on the left or the right Cauchy deformation tensors or equivalently the invariants of these tensors. Similarly, strain energy density function only depends on invariants of, for example C tensor, which are

$$\begin{aligned}
&\bar{w}\left(I_1,\, I_2,\, I_3\right), \;\; \det(\mathrm{F}) = J \\
&I_1 = \mathrm{tr}(\mathrm{C}) = \lambda_1^2 + \lambda_2^2 + \lambda_3^2 \\
&I_2 = \tfrac{1}{2}\left(\mathrm{tr}(\mathrm{C})^2 - \mathrm{tr}(\mathrm{C}^2)\right) = \mathrm{C} : \mathrm{C} = \lambda_1^2\lambda_2^2 + \lambda_2^2\lambda_3^2 + \lambda_3^2\lambda_1^2 \\
&I_3 = \det(\mathrm{C}) = (J)^2 = \lambda_1^2\lambda_2^2\lambda_3^2
\end{aligned} \tag{2.6}$$

where *det* and *tr* refer to the determinant and trace of a tenor, J is the Jacobian and $\frac{d(v)}{d(V)}$ represents the volume change between the deformed and reference configurations, and λ_i's are the eigenvalues of tensor C. Differentiating of these invariants with respect to C gives

$$\frac{\partial I_1}{\partial \mathrm{C}} = \mathrm{I}, \quad \frac{\partial I_2}{\partial \mathrm{C}} = 2\mathrm{C}, \quad \frac{\partial I_3}{\partial \mathrm{C}} = I_3\mathrm{C}^{-1} \tag{2.7}$$

For small deformations, after neglecting the higher order terms, the *Eulerian/Almansi* and *Lagrangian/Green* strain tensor are equivalent with the small or infinitesimal strain tensor ε, that is

$$\gamma = \eta = \varepsilon = \tfrac{1}{2}\left(\tfrac{\partial u_i}{\partial X_j} + \tfrac{\partial u_j}{\partial X_i}\right) = \tfrac{1}{2}\left(\tfrac{\partial u_i}{\partial x_j} + \tfrac{\partial u_j}{\partial x_i}\right) \tag{2.8}$$

2.1.2 Stress tensors

Deformation energy Ψ is the energy required to deform a material and represents the area under the stress-strain diagram. In the equilibrium state the variation of deformation energy is zero. This variation may be expressed as

$$\delta\Psi = \int_\Omega \frac{\partial\bar{w}}{\partial\gamma} : \delta\gamma = \int_\Omega \frac{\partial\bar{w}}{\partial \mathrm{C}}\frac{\partial \mathrm{C}}{\partial\gamma} : \delta\gamma = \int_\Omega 2\frac{\partial\bar{w}}{\partial \mathrm{C}} : \delta\gamma \tag{2.9}$$

The relation between C and γ in the above equation is defined in equation(2.4). Disregarding residual stresses for isothermal reversible processes, $\frac{\partial\bar{w}}{\partial\gamma}$ in the above equation has a physical meaning and is referred to as the second Piola-Kirchhoff stress tensor $P - K^2$ or S.

$$\mathrm{S} = \frac{\partial\bar{w}}{\partial\gamma} = \frac{2\partial\bar{w}}{\partial \mathrm{C}} = 2\frac{\partial\bar{w}}{\partial I_1}\mathrm{I} + 4\mathrm{C}\frac{\partial\bar{w}}{\partial I_2} + 2I_3\mathrm{C}^{-1}\frac{\partial\bar{w}}{\partial I_3} \tag{2.10}$$

Applying this stress tensor to an area element with unit normal vector $\boldsymbol{N}$ and on area of A in the original undeformed coordinate results in a non-physical force $\mathrm{F}^{-1}f$ in the reference coordinate system, where f is the physical force on the area

$$\mathrm{S}\,\boldsymbol{N}\,dA = \mathrm{F}^{-1}\boldsymbol{f} \tag{2.11}$$

In the above equation, f pertains to the physical force on the deformed area, hence to obtain a stress tensor in the undeformed configuration that results in the physical force in the deformed configuration, the first Piola-Kirchhoff stress tensor $P - K^1$ or P is defined as P = F S

$$\mathrm{S} = \mathrm{F}^{-1}\mathrm{P} \rightarrow \mathrm{P}\,\boldsymbol{N}\,dA = \boldsymbol{f} \tag{2.12}$$

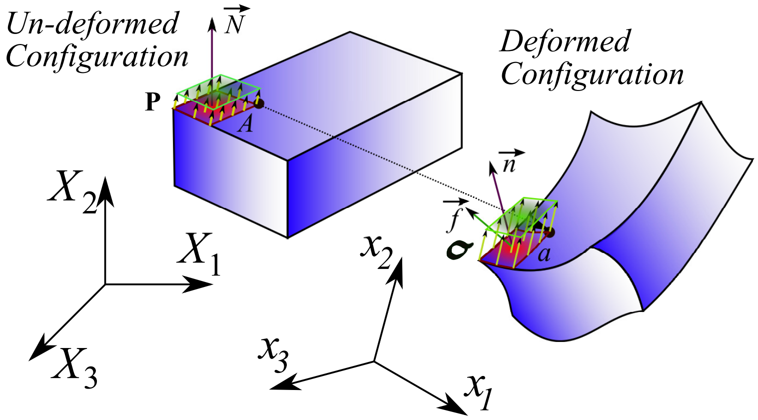

Figure 2.3 Relation between the Cauchy stress tensor and first P-K stress tensor

Finally, as shown on figure(2.3), the Cauchy stress tensor σ is specified on the deformed configuration that relates the actual force vector $\boldsymbol{f}$ on the deformed area a with unit normal $\boldsymbol{n}$ to the stress tensor

$$\sigma\,\boldsymbol{n}\,da = \boldsymbol{f} \tag{2.13}$$

2.2 Constitutive equations

Constitutive equations relate the material response to the applied loading, for example in structural mechanics the relationship between stresses or forces with strains or deformations is defined with these equations [1]. As discussed in section(2.1.2) the second Piola-Kirchhoff stress tensor is the derivative of strain energy density $\bar{w}$ with respect to Lagrangian/Green strain tensor γ. In general for isothermal processes the second Piola-Kirchhoff stress tensor in terms of the Green strain tensor can be simplified to

$$\mathrm{S} = \mathrm{K} : \gamma \quad or \quad \mathrm{S}_{ij} = \sum_{kl} \mathrm{K}_{ijkl}\, \gamma_{kl} \tag{2.14}$$

where K is a fourth order stiffness tensor. Equation(2.14) is known as Hooke's law, and the strain energy density function for these materials will be reduced to

$$\bar{w} = \int_{\Omega} \gamma : \mathrm{K} : \gamma \tag{2.15}$$

The definition of deformation energy density will depend on the material of interest.

2.2.1 Linear elastic materials

Materials for which the constitutive behavior is only a function of the current state of deformation are generally known as elastic [1]. As shown in equation(2.8), for small deformations, the infinitesimal strain tensors may be used and the relation between stress and strain can be written as

$$\sigma = \mathrm{K} : \varepsilon \tag{2.16}$$

where K is the fourth order stiffness tensor and defined as

$$\mathrm{K}_{\mathrm{ijkl}} = \lambda \delta_{\mathrm{ij}} \delta_{\mathrm{kl}} + \mu \left(\delta_{\mathrm{ik}} \delta_{\mathrm{jl}} + \delta_{\mathrm{il}} \delta_{\mathrm{jk}} \right) \tag{2.17}$$

where λ and μ are the first and second Lamé's constants that depend on the mechanical properties of the material. These parameters can be represented in terms of the Young's modulus **E** and Poisson's ratio ν for and isotropic material as

$$\begin{aligned} \lambda &= \tfrac{\nu \mathbf{E}}{(1+\nu)(1-2\nu)} \\ \mu &= \tfrac{\mathbf{E}}{2(1+\nu)} \end{aligned} \tag{2.18}$$

Substituting the stiffness tensor in equation(2.17), into equation(2.15) and assuming the material undergoes small strains, gives the strain energy function of linear elasticity as

$$\bar{w} = \int_{\Omega} \varepsilon : \mathrm{K} : \varepsilon \tag{2.19}$$

Since these materials assume small strains, the elasticity equations are the same in the current and the reference configurations.

2.2.2 Neo-Hookean hyper elastic materials

When the work done by the stresses during a deformation process is dependent only on the initial state and the final configuration, the behavior of the material is said to be path-independent (that is, reversible) and the material is termed hyper elastic [1]. A general type of hyper elastic materials is called neo-hookean or rubber like materials [2]. The strain energy function of these materials is defined as

$$\bar{w} = \frac{1}{2}\mu(I_1 - 3) - \mu \ln(J) + \frac{1}{2}\lambda(J-1)^2 \tag{2.20}$$

The second Piola-Kirchhoff and Lagrangian elasticity tensors are defined as the first and second derivatives of the equation(2.20) and are shown in equations(2.21) and (2.22) respectively.

$$\mathrm{S} = \mu(\mathrm{I} - \mathrm{C}^{-1}) + \lambda J(J-1)\mathrm{C}^{-1} \tag{2.21}$$

$$\begin{aligned} \mathrm{K} &= \lambda J(2J-1)\mathrm{C}^{-1} \otimes \mathrm{C}^{-1} + 2\left[\mu - \lambda J(J-1)\right] \diamond \\ \diamond_{ijkl} &= \left(\mathrm{C}^{-1}\right)_{ik}\left(\mathrm{C}^{-1}\right)_{jl} \end{aligned} \tag{2.22}$$

The stress and stiffness tensors can be defined in the current or Eulerian configuration as well [3]. As discussed before, stress in the current configuration is known as the Cauchy stress tensor or σ and can be written in terms of the second Piola-Kirchhoff tensor as

$$\mathrm{S} = J\,\mathrm{F}^{-1}\,\sigma\,\mathrm{F}^{-T}; \sigma = J^{-1}\mathrm{F}\,\mathrm{S}\,\mathrm{F}^{T} \tag{2.23}$$

Hence, the stress and stiffness tensors in the Eulerian configuration are

$$\begin{aligned}
&\sigma = \tfrac{\mu}{J}(\mathrm{B} - \mathrm{I}) + \lambda(\mathrm{J} - 1)\mathrm{I} \\
&\mathrm{K}_{\mathrm{Eulerian}} = \lambda\,(2J - 1)\mathrm{I} \otimes \mathrm{I} + \tfrac{2}{J}\left[\mu - \lambda J(J - 1)\right] \wp \qquad (2.24) \\
&\wp_{ijkl} = \delta_{ik}\delta_{jl}
\end{aligned}$$

Based on additional assumptions, the equations for neo-Hookean hyper elasticity may take different forms. In the current work, transversely isotropic neo-Hookean materials are implemented and will subsequently be discussed. Interested readers are directed to [1] for more details concerning the various forms of these equations. If the deformation energy density is defined as

$$\bar{w} = \frac{\mu}{2}(I_1 - 3) - \mu \ln(J) + \frac{\lambda}{2}(\ln J)^2 \qquad (2.25)$$

The Cauchy stress and stiffness tensors for this model are

$$\begin{aligned}
&\sigma = \tfrac{\mu}{J}(\mathrm{B} - \mathrm{I}) + \tfrac{\lambda}{J}(\ln J)\mathrm{I} \\
&\mathrm{K}_{\mathrm{Eulerian}} = \tfrac{\lambda}{J}\,\mathrm{I} \otimes \mathrm{I} + \tfrac{2}{J}\left[\mu - \lambda \ln J\right] \wp \qquad (2.26) \\
&\wp_{ijkl} = \delta_{ik}\delta_{jl}
\end{aligned}$$

2.2.3 Saint Venant-Kirchhoff materials

The simplest model for hyper-elastic materials is the Saint Venant-Kirchhoff model which is used for isotropic and isothermal materials. Strain energy density for these materials is defined as

$$\bar{w}(\gamma) = \frac{1}{2}\lambda \left(\mathrm{tr}(\gamma)\right)^2 + \mu\gamma : \gamma \tag{2.27}$$

The second Piola-Kirchhoff stress tensor becomes

$$\mathrm{S} = \frac{\partial \bar{w}(\gamma)}{\partial \gamma} = \left(\lambda \delta_{ij}\delta_{kl} + \mu \left(\delta_{ik}\delta_{jl} + \delta_{il}\delta_{jk}\right)\right)\gamma_{kl} = \lambda \mathrm{tr}(\gamma)\mathrm{I} + 2\mu\gamma \tag{2.28}$$

The stiffness tensor in these types of materials is constant and shall be defined the same as linear elastic materials. The difference between this class of materials and linear elastic materials is that the strain is not linear. Therefore, Hooke's law for these materials in the reference and current configurations can be defined as

$$\begin{aligned} \mathrm{S} &= \mathrm{K} : \gamma \\ \sigma &= \mathrm{K} : \eta \end{aligned} \tag{2.29}$$

The constitutive equations presented in section(2.2.2) are valid in the fully nonlinear range and they are used as the isotropic component of the transversely isotropic model derived in section(5). Constitutive equations here in section(2.2.3) for the Saint Venant-Kirchhoff materials have linear stress-strain relations, therefore these equations are more applicable in small to moderate strain ranges.

2.3 Discretization of linear elasticity

Strain and stress tensors in both Lagrangian and Eulerian coordinates have been discussed. The relationship between these two tensors is defined through the constitutive equations that was generally illustrated in the previous section. The strong form of the elasticity equations, as previously noted, represent the conservation of momentum in the Lagrangian coordinate for mechanics of materials. A general methodology for the solution of structural problems is the finite element method. Two commonly used discretization techniques for linear materials will be presented in chapter(3).

2.4 Linearization and Newton-Raphson solution

The neo-hookean and Saint Venant-Kirchhoff model of materials are nonlinear and, therefore must be solved iteratively. An iterative solution procedure, such as Newton-Raphson method, requires linearization of the system of equations. There are different approaches to numerically obtain the linearization of the system. Two such techniques are traditional finite difference or the complex Taylor series expansion (CTSE) method [4]. Using the CTSE method the exact tangent matrix for the simulation process will be obtained to second order accuracy and without subtractive cancellation errors. In this section a linearized tangent matrix based on the virtual work scheme will be provided. Virtual work of these nonlinear materials for a system undergoing a virtual velocity is a function of the current configuration $\Im(x)$ or displacement $\Im(u)$. Recall the displacement vector

$$u = x - X \rightarrow R = \delta W(x) = \Im(x) \; or \; R = \delta W(u) = \Im(u) \tag{2.30}$$

where R is the residual. In the virtual work the summation of internal and external works should be zero, hence

$$R = \delta W(u) = \int \mathrm{S} : \dot{\gamma}\, d\bar{V} - \int b.\delta \mathrm{v}\, d\bar{V} - \int t.\delta \mathrm{v}\, dA = 0 \tag{2.31}$$

where v is the velocity vector, b is the body force, t is traction forces on the surface and $\bar{V}$ is the volume in the original configuration. $\dot{\gamma}$ is the material strain rate tensor and is defined as

$$\dot{\gamma} = \frac{1}{2}\dot{\mathrm{C}} = \frac{1}{2}\left(\dot{\mathrm{F}}^T\mathrm{F} + \mathrm{F}^T\dot{\mathrm{F}}\right) \tag{2.32}$$

$\dot{\mathrm{F}}$ is the time derivative of the deformation gradient tensor F. The displacement vector u and the velocity vector v can be written in terms of the basis functions N_i and nodal displacement values u_i as $\mathrm{u} = \sum N_i u_i = N.u$ and $\mathrm{v} = N.v$. The velocity gradient tensor l is defined as the derivative of velocity with respect to the current coordinates. With this definition the time derivative of the deformation gradient tensor becomes

$$l = \frac{\partial \mathrm{v}(x,t)}{\partial x} = \nabla_x \mathrm{v} = \nabla_x N.v \rightarrow \dot{\mathrm{F}} = \frac{\partial \mathrm{v}(x,t)}{\partial X} = l\,\mathrm{F} = (\nabla_x N.v)\,\mathrm{F} \tag{2.33}$$

Using the Newton-Raphson algorithm and assuming that the residual approaches zero, the first order expansion is written as

$$R^{n+1} = R^n + \frac{\partial R}{\partial u} du \rightarrow \frac{\partial R}{\partial u} du = -R^n \tag{2.34}$$

Substituting the residual due to internal work from equation(2.31) into the above relation, the linearized internal work can be written as

$$\begin{aligned}
&\frac{\partial\left(\int_{\bar{V}} \mathrm{S}:\dot{\gamma}\right) d\bar{V}}{\partial u} = \int_{\bar{V}} \left(\frac{\partial \mathrm{S}}{\partial \mathrm{u}} : \dot{\gamma}\right) d\bar{V} + \int_{\bar{V}} \left(\mathrm{S} : \frac{\partial \dot{\gamma}}{\partial \mathrm{u}}\right) d\bar{V} \\
&= \int_{\bar{V}} \left(\frac{\partial \mathrm{S}}{\partial \gamma}\frac{\partial \gamma}{\partial \mathrm{u}} : \dot{\gamma}\right) d\bar{V} + \int_{\bar{V}} \left(\mathrm{S} : \frac{\partial \dot{\gamma}}{\partial \mathrm{u}}\right) d\bar{V} \\
&= \int_{\bar{V}} \left(\frac{\partial \gamma}{\partial \mathrm{u}} : \mathrm{K} : \dot{\gamma}\right) d\bar{V} + \int_{\bar{V}} \left(\mathrm{S} : \frac{\partial \dot{\gamma}}{\partial \mathrm{u}}\right) d\bar{V}
\end{aligned} \tag{2.35}$$

Equation(2.35) assumes that the external work is not a function of displacement vector. To evaluate the above equation, the terms $\frac{\partial \gamma}{\partial \mathrm{u}}$, $\dot{\gamma}$ and $\frac{\partial \dot{\gamma}}{\partial \mathrm{u}}$ should be defined. Furthermore, the derivative of deformation gradient tensor with respect to displacement may be expressed as

$$\frac{\partial \mathrm{F}}{\partial \mathrm{u}} = \frac{\partial}{\partial \mathrm{u}}\left(\frac{\partial(X + \sum N_i u_i)}{\partial X}\right) = \nabla_X N = \nabla_x N.\,\mathrm{F} \tag{2.36}$$

With this equation $\frac{\partial \gamma}{\partial \mathrm{u}}$ is given by

$$\frac{\partial \gamma}{\partial \mathrm{u}} = \frac{\partial \gamma}{\partial \mathrm{F}}\frac{\partial \mathrm{F}}{\partial \mathrm{u}} = \frac{1}{2}\mathrm{F}^T(\nabla_x N + (\nabla_x N)^T)\mathrm{F} = \mathrm{F}^T(\nabla_x N)\mathrm{F} \tag{2.37}$$

Following equations(2.32) and (2.33) the material strain rate tensor yields

$$\dot{\gamma} = \left(\frac{1}{2}\mathrm{F}^T(\nabla_x N + (\nabla_x N)^T).v\,\mathrm{F}\right) = \mathrm{F}^T(\nabla_x N).v\,\mathrm{F} \tag{2.38}$$

Also $\frac{\partial \dot{\gamma}}{\partial \mathrm{u}}$ is the time derivative of equation(2.37) and is defined as

$$\frac{\partial \dot{\gamma}}{\partial \mathrm{u}} = \frac{\partial}{\partial t}\frac{\partial \gamma}{\partial \mathrm{u}} = \frac{\partial}{\partial t}\left(\mathrm{F}^T(\nabla_x N)\mathrm{F}\right) = \dot{\mathrm{F}}^T(\nabla_x N)\mathrm{F} + \mathrm{F}^T(\nabla_x N)\dot{\mathrm{F}} = \mathrm{F}^T(\nabla_x N\nabla_x N).v\,\mathrm{F} \tag{2.39}$$

The relation between the elasticity tensor, stress tensor and volume between Eulerian and Lagrangian coordinates can be written as

$$\begin{aligned} &\sigma = J^{-1}\mathrm{F}\mathrm{S}\mathrm{F}^{T} \\ &(\mathrm{K}_{\mathrm{Eulerian}})_{ijkl} = J^{-1} \sum_{I,J,K,L=1}^{3} \mathrm{F}_{iI}\mathrm{F}_{jJ}\mathrm{F}_{kK}\mathrm{F}_{lL}\mathrm{K}_{IJKL} \\ &\bar{v} = J\bar{V} \end{aligned} \tag{2.40}$$

Substituting these relations, along with equations(2.37), (2.38) and (2.39), into equation(2.35), the linearized internal work in the current or Eulerian coordinates can be written as

$$\frac{\partial R}{\partial u} = \int_{\bar{v}} (\nabla_x N : \mathrm{K}_{\mathrm{Eulerian}} : \nabla_x N)\ d\bar{v} + \int_{\bar{v}} \sigma : (\nabla_x N \nabla_x N)\, d\bar{v} \tag{2.41}$$

The linearized format is further analyzed and validated with central finite difference formulations. As it is obvious in equation(2.41), the first part of the linearized internal work is the stiffness matrix for linear materials. The second part is the added term in the tangent matrix for the nonlinear materials. In these equations the stress and elasticity tensors should be calculated with the relations provided based on the material of interest. Furthermore, at each iteration, the linear system is solved using GMRES [5].

External work can also be a function of current configuration because of change in volume and surface area of material after deformation and these terms can contribute in the calculation of the LHS. Three procedures are suggested for this issue:

- First is to assume that the body and boundary forces are constant with deformation; for example, constant weight means that the density of the elements changes with the transformation of the elements to maintain the constant body force.
- Second is to take into account this nonlinear part in the tangent matrix.
- And third is to ignore this fraction of nonlinearity because it is not necessary to have an exact tangent matrix, but these parameters should be exactly calculated in the right hand side.

CHAPTER 3

DISCONTINUOUS GALERKIN FOR ELLIPTIC EQUATIONS

3.1 Introduction

Discontinuous Galerkin (DG) finite elements methods intrinsically have some attractive properties and, therefore have received considerable attention within the scientific community. However, one drawback of these schemes has been their computational implementation for second order equations. Following [6], in this section, DG schemes for solving Poisson and linear elasticity equations are formulated in a unified primal equation. From these methods, classes of interior penalty methods are rewritten by adding stability and symmetry terms. By introducing new fluxes for the interior and boundary faces, the primal equation that applies for all branches of interior penalty schemes can be formulated. Herein, detailed implementation of those equations is described and discussed, and a few examples with exact solutions are illustrated and verified via error analysis.

3.2 A short note about history

In recent years, Discontinuous Galerkin (DG) finite element methods (FEM) that allows discontinuity between the elements have been used in a wide range of applications. This stems from the characteristics of DG formulations. DG methods can be locally high-order accurate enabling them to model complex geometries and sensitive boundary conditions. Although discontinuity between the elements increases the number of degrees-of-freedom of the problem, the mass matrix is block diagonal. Furthermore, the stiffness matrix will only be dependent upon the local element and the immediate neighbors of the elements. These attributes render these schemes ideal for parallelization and adaptation techniques. Moreover, stability of the DG techniques can be guaranteed in the formulation. Being locally conservative for physical quantities such as mass, momentum and energy, DG methods have received considerable attention in Computational Fluid Dynamics (CFD) [7].

Reed and Hill [8] first introduced DG methods for hyperbolic equations. During the same decade some variants of Galerkin FEM admitting discontinuities between elements were introduced for elliptic and parabolic equations [9, 10]. This family of FEM is called interior penalty (IP) methods and share a common concept with the DG methods.

In the last decade, implementation of DG methodologies have grown in solid mechanics due to the amenability of the methods for parallel programming and to complex geometries. Some examples of exploiting the DG method for beams, plates and shells can be found in [11, 12]. Lew et al. [13] have implemented DG for linear elasticity, Hansbo and Larson [14] also developed a DG FEM for incompressible and nearly incompressible elasticity. Eyck and Lew [15] expanded the implementation in [13] to non-linear elasticity.

Discontinuity in the displacement jumps between the elements and compatibility of the mesh adaptation in crack propagation problems are pressing issues within fracture mechanics and may be addressed using DG approaches. Examples of implementation of DG methods in fracture mechanics can be found in [16–18].

The Interior Penalty (IP) method was first introduced to impose Dirichlet boundary conditions weakly. Nitsche [19] introduced a consistency, symmetric and a penalty term in the bi-linear matrix of the Poisson equation. In a similar work by Babuška [20], a penalty term for penalizing the jump was utilized. Further discussion concerning the IP scheme can be found in the works by Arnold [10], Douglas and Dupont [9], Baker [21] and Babuška and M. Zlámal [22]. For other implementations of the IP scheme, and an excellent review of the development of IP methods, the reader is directed to [23]. Meanwhile, starting with the work of Bassi and Rebay in 1997 [24], but independently from improvements in the IP, DG schemes for elliptic equations were implemented in the Navier-Stokes equations. Later Cockburn and Shu [25] generalized the work of Bassi and Rebay and introduced the Local Discontinuous Galerkin (LDG) method. Other variants were proposed by Brezzi et al. [26, 27], Baumann and Oden [28], Bassi et al. [29] and Riviére et al. [30]. As noted in the work of Arnold et al. [6], these variants can be written in a unified fashion and the difference between them is the definition of numerical fluxes. A complete review concerning the development of DG methods can be found in [31].

The next section is devoted to explaining the discussed DG formulations of the Poisson equation in a unified format. IP schemes will be subsequently presented for the Poisson equation and linear elasticity. In this work, implementation of the DG scheme is thoroughly discussed, and examples with error analysis are provided for verification.

3.3 Discontinuous Galerkin formulation of the Poisson equation in a unified primal format

A d-dimensional convex polygon computational domain of Ω in $\mathbb{R}^d$, $d = 1, 2$ or 3, confined in boundary $\partial\Omega$ partitioned with Dirichlet and Neumann boundary condition of $\partial\Omega_D$ and $\partial\Omega_N$ is defined; where $\partial\Omega_D \cup \partial\Omega_N = \partial\Omega$, $\partial\Omega_D \cap \partial\Omega_N = \emptyset$ and $\partial\Omega_D \neq \emptyset$. Consider the model boundary value problem of

$$\begin{aligned} &-\nabla.(\kappa\nabla u) = f \;\; in \; \Omega \\ &u = u_D \;\; on \; \partial\Omega_D \\ &\kappa\tfrac{\partial u}{\partial \mathbf{n}} = u_N \; on \; \partial\Omega_N \end{aligned} \tag{3.1}$$

where f, u_D and u_N are given functions in $L^2(\Omega)$, κ is a positive value in $L^\infty(\Omega)$ and $\mathbf{n}$ is the outward unit normal vector on the boundaries. Introducing an auxiliary variable $\bar{\sigma} = \kappa\nabla u$, equation(3.1) can be written as a system of two ordinary differential equations

$$\begin{aligned} &\bar{\sigma} = \kappa\nabla u \;\; in \; \Omega \\ &-\nabla.\bar{\sigma} = f \;\; in \; \Omega \\ &u = u_D \;\; on \; \partial\Omega_D \\ &\bar{\sigma}.\mathbf{n} = u_N \; on \; \partial\Omega_N \end{aligned} \tag{3.2}$$

Assume subdivision $\mathcal{T}_h = \{E\}$ of the domain Ω, where E is an interval, triangle or tetrahedron if d =1,2, or 3, respectively. Broken spaces $V(\mathcal{T}_h)$ and $\bar{\Sigma}(\mathcal{T}_h)$ are introduced as

$$\begin{aligned} &V_h := \left\{v \in L^2(\Omega) : v|_E \in P(E) \;\; \forall E \in \mathcal{T}_h\right\} \\ &\sum\nolimits_h := \left\{\tau \in \left[L^2(\Omega)\right]^d : \tau|_E \in \sum(E) \;\; \forall E \in \mathcal{T}_h\right\} \end{aligned} \tag{3.3}$$

where $P(E) = \mathbf{P_p(E)}$ is the polynomial space with the degree of $1 \leq p$ and $\sum(E) = \left[\mathbf{P_p(E)}\right]^d$ is a polynomial vector field of degree p or $p-1$. Now $u_h \in V_h$ and $\bar{\sigma}_h \in \sum_h$ should be found such that for all elements $E \in \mathcal{T}_h$ the following relations holds

$$\begin{aligned} &\int_E \bar{\sigma}_h.\tau \, dx = \int_E (\kappa \nabla u_h).\tau \, dx \\ &\int_E (-\nabla.\bar{\sigma}_h) \, v \, dx = \int_E f \, v \, dx \end{aligned} \tag{3.4}$$

Application of integration by parts gives

$$\int_E \bar{\sigma}_h.\tau \, dx = -\int_E u_h \, \nabla.(\kappa\tau) \, dx + \int_{\partial E} \hat{u} \, \kappa \, (\tau.\mathbf{n}) \, ds \tag{3.5}$$

$$\int_E \bar{\sigma}_h.\nabla v \, dx = \int_E f \, v \, dx + \int_{\partial E} v(\hat{\sigma}.\mathbf{n}) \, ds \tag{3.6}$$

In the above equations, ∂E refers to boundaries of all elements $E \in \mathcal{T}_h$ and $\hat{u}$ and $\hat{\sigma}$ are the $numerical fluxes$ that approximate the traces of u and $\bar{\sigma} = \kappa\nabla u$ on ∂E. ∂E can be divided to boundary faces $\partial\Omega$ and the union of all interior faces $\partial\Omega_i$. Furthermore, $\partial\Omega$ consists of Neumann boundary condition $\partial\Omega_N$ and Dirichlet boundary conditions $\partial\Omega_D$. By setting $\tau = \nabla v$, equation(3.5) can be rewritten as

$$\int_E \bar{\sigma}_h.\nabla v \, dx = -\int_E u_h \, \nabla.(\kappa\nabla v) \, dx + \int_{\partial E} \hat{u} \, \kappa \, (\nabla v.\mathbf{n}) \, ds \tag{3.7}$$

Performing integration by parts on the first term in the right hand side of equation(3.7) yields

$$\int_E \bar{\sigma}_h.\nabla v \, dx = \int_E \nabla u_h \, (\kappa \nabla v) \, dx + \int_{\partial E} (\hat{u} - u_h) \, (\kappa \nabla v).\mathbf{n} \, ds \tag{3.8}$$

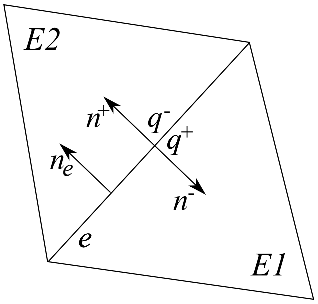

Figure 3.1 Face e shared with two elements $E1$ and $E2$ with the unit normal of n_e from $E1$ to $E2$ with double valued variable q on either side

To prevent double surface integration over ∂E_i, two operators of jump [.] and average {.} are defined. As shown in figure(3.1), considering an interior face e between two elements $E1$ and $E2$ with an associated unit normal of $\mathbf{n_e}$, these operators are defined as

$$\forall e = \partial E1 \cap \partial E2, \quad [w] = (w|_{E1}) - (w|_{E2}), \quad \{w\} = \frac{1}{2}(w|_{E1}) + \frac{1}{2}(w|_{E2}) \tag{3.9}$$

The definition of these two operators on the boundary faces are

$$\forall e = \partial E1 \cap \partial \Omega, \quad [w] = (w|_{E1}), \quad \{w\} = (w|_{E1}) \tag{3.10}$$

It can be shown that the result of the integration of variable q multiplied by a test function w on the element boundaries ∂E each with unit normal of $\mathbf{n_e}$ can be written as the summation of jump and average operators on the union of interior faces $\partial\Omega_i$ with unit normal vector of $\mathbf{n}$ and the boundary of domain $\partial\Omega$

$$\sum_{E\in\mathcal{T}_h}\int_{\partial E} q\, w\, \mathbf{n_e}\mathbf{ds} = \int_{\partial\Omega_i} [q]\,\{w\}\,\mathbf{nds} + \int_{\partial\Omega_i} \{q\}\,[w]\,\mathbf{nds} + \int_{\partial\Omega} q\, w\,\mathbf{nds} \tag{3.11}$$

Comparing equations(3.6) and (3.8), the equivalency of the Left Hand Side (LHS) of these two equations can be observed, thus the combination of these two equations gives the the so called *primal formulation*

$$\int_E \nabla u_h\,.(\kappa\nabla v)\,dx + \int_{\partial E} (\hat{u} - u_h)\,(\kappa\nabla v).\mathbf{n}\,ds = \int_E f\,v\,dx + \int_{\partial E} v(\hat{\sigma}.\mathbf{n})\,ds \tag{3.12}$$

Furthermore applying relation(3.11) in equation(3.12) gives

$$\begin{aligned}&\textstyle\int_E \nabla u_h\,.(\kappa\nabla v)\,dx + \int_{\partial\Omega_i} ([\hat{u} - u_h]\,\{\kappa\nabla v\} + \{\hat{u} - u_h\}\,[\kappa\nabla v])\,.\mathbf{n}\,ds\\ &\textstyle- \int_{\partial\Omega_i} ([\hat{\sigma}]\,\{v\} + \{\hat{\sigma}\}\,[v])\,.\mathbf{n}\,ds + \int_{\partial\Omega} (\hat{u}_b - u_h)\,(\kappa\nabla v).\mathbf{n}\,ds - \int_{\partial\Omega} v(\hat{\sigma}_b.\mathbf{n})\,ds\\ &\textstyle= \int_E f\,v\,dx\end{aligned} \tag{3.13}$$

in which $\hat{u}_b$ and $\hat{\sigma}_b$ refer to the fluxes on the boundaries.

Equation(3.13) is the basis to compare different variants of DG schemes for the elliptic equations. The diversity of the methods originates from the definition of fluxes on the interior and boundary faces. These effect the behavior of the solution, such as the stability and accuracy, as well as sparsity of the matrices or symmetry of the stiffness matrix. Other properties such as *locality*, *consistency* and *conservation* can be investigated for each method as well. These properties are defined as:

1. A method is called local if the fluxes defined on the face e shared between elements $E1$ and $E2$ are only function of u_{E1}, ∇u_{E1}, $\bar{\sigma}_{E1}$, u_{E2}, ∇u_{E2} and $\bar{\sigma}_{E2}$.

$$\begin{aligned} \hat{u}|_e &= f\left(u_{E1}, \nabla u_{E1}, \bar{\sigma}_{E1}, u_{E2}, \nabla u_{E2}, \bar{\sigma}_{E2}\right) \\ \hat{\sigma}|_e &= f\left(u_{E1}, \nabla u_{E1}, \bar{\sigma}_{E1}, u_{E2}, \nabla u_{E2}, \bar{\sigma}_{E2}\right) \end{aligned} \tag{3.14}$$

2. Consistency refers to schemes that satisfy

$$\begin{aligned} \hat{u}|_e &= f\left(u_{E1}, \nabla u_{E1}, u_{E2}, \nabla u_{E2}\right) = u|_e \\ \hat{\sigma}|_e &= f\left(u_{E1}, \nabla u_{E1}, u_{E2}, \nabla u_{E2}\right) = \kappa \nabla\, u|_e \end{aligned} \tag{3.15}$$

   Where $u|_e$ satisfy the Dirichlet boundary conditions on $\partial\Omega_D$.

3. And finally a scheme is conservative if the numerical fluxes $\hat{u}$ and $\hat{\sigma}$s on a face shared between elements $E1$ and $E2$ are the same

$$\begin{aligned} \hat{u}_{E1}|_e &= \hat{u}_{E2}|_e \\ \hat{\sigma}_{E1}|_e &= \hat{\sigma}_{E2}|_e \end{aligned} \tag{3.16}$$

In fact, if the test function v in equation(3.6) is taken as identity, the conservative fluxes satisfy

$$\int_E f\, dx = -\int_{\partial E} (\hat{\sigma}.\mathbf{n})\, ds \tag{3.17}$$

Further discussion and comprehensive reviews concerning these properties can be found in the works of Arnold et al. [23] and Castillo [32].

3.3.1 Interior penalty methods

DG schemes for the elliptic problems can be categorized as Symmetric Interior Penalty discontinuous Galerkin (SIPG), Non-Symmetric Interior Penalty discontinuous Galerkin (NIPG) and Incomplete Interior Penalty discontinuous Galerkin (IIPG). The differnece between these methods is the sign of the added symmetry term to the weak form of the elliptic equation. To begin considering the concept of IP methods, one can write the weak form of Poisson equation as

$$\int_E \nabla u_h\, (\kappa \nabla v)\, dx - \int_{\partial E} (\kappa \nabla u_h)\, .\mathbf{n}\, v\, ds = \int_E f\, v\, dx \tag{3.18}$$

or with the average and jump notations as

$$\begin{aligned} &\textstyle\int_E \nabla u_h\, (\kappa \nabla v)\, dx - \int_{\partial \Omega_i} (\{\kappa \nabla u_h\}\, [v])\, .\mathbf{n}\; ds - \int_{\partial \Omega_i} ([\kappa \nabla u_h]\, \{v\})\, .\mathbf{n}\; ds - \int_{\partial \Omega} (\kappa \nabla u_h)\, .\mathbf{n}\, v\, ds \\ &= \textstyle\int_E f\, v\, dx \end{aligned} \tag{3.19}$$

In the exact solution, the term $-\int_{\partial\Omega_i} ([\kappa\nabla u_h]\,\{v\})\,.\mathbf{n}\ ds$ vanishes and makes integration unstable, hence this term is omitted and two other terms are added to equation(3.19) to insure the coercivity of the scheme. The general formulation can be written as

$$A(u_h, v) = L(v) \tag{3.20}$$

where $A(u_h, v)$ is the bi-linear form and $L(v)$ the linear form and are defined as

$$\begin{aligned} A(u_h, v) &:= \int_E \nabla u_h\,(\kappa\nabla v)\,dx - \int_{\partial\Omega_i} (\{\kappa\nabla u_h\}\,[v])\,.\mathbf{n}\ ds - \int_{\partial\Omega} (\kappa\nabla u_h)\,.\mathbf{n}\,v\ ds \\ &\overbrace{-\,\alpha\int_{\partial\Omega_i+\partial\Omega} (\{\kappa\,\nabla v\}\,[u_h])\,.\mathbf{n}\ ds}^{symmetry} + \overbrace{\int_{\partial\Omega_i+\partial\Omega} {}^{\eta_e}/_{l_e}([u_h]\,[v])\ ds}^{stability} \\ L(v) &:= \int_E f\,v\,dx \end{aligned} \tag{3.21}$$

The first and second added terms are known as symmetry and stabilization terms, and ${}^{\eta_e}/_{l_e}$ is the penalty parameter. Here, l_e is the diameter of element and η_e is a positive coefficient that must be large enough to insure the stability of the method [10]. Epshteyn and Riviére [33] expressed the minimum value of η_e as a function of the local polynomial degree and the smallest degree in the triangulation of the mesh for SIPG and IIPG. As described by Wheeler [34], η_e should only be a positive number and does not have any minimum limit in NIPG method. Other limits for the stability coefficient can be found in the work by Shahbazi [35]. Furthermore, the coefficient α defines the variant of IP method:

1. $\alpha = 1$: SIPG, Douglas and Dupont [9], Wheeler [34]

2. $\alpha = -1$: NIPG, Baumann and Oden [36], Riviére, Wheeler and Girault [30]

3. $\alpha = 0$: IIPG, Sun and Wheeler [37]

The bi-linear form $A(u_h, v)$ is positive definite for a sufficiently large penalty parameter; it is also symmetric for SIPG and non-symmetric for NIPG and IIPG.

A set of local, consistent and conservative fluxes are defined here for SIPG methods as

$$\begin{aligned} &Interior\ Faces \begin{cases} \hat{u} = \{u_h\} \\ \hat{\sigma}.\mathbf{n} = \kappa \nabla u_h.\mathbf{n} - \left({}^{\eta_e}\!/_{l_e} \right) [u_h] \end{cases} \\ &Dirichlet\ Boundaries \begin{cases} \hat{u}_b = u_D \\ \hat{\sigma}_b.\mathbf{n} = \kappa\ \nabla u_h.\mathbf{n} - {}^{\eta_e}\!/_{l_e} (u_h - u_D) \end{cases} \\ &Neumann\ Boundaries \begin{cases} \hat{u}_b = u_h \\ \hat{\sigma}_b.\mathbf{n} = u_N \end{cases} \end{aligned} \tag{3.22}$$

Incorporating these fluxes into equation(3.13), and using the following identities

$$[\{.\}] = 0, \quad [[.]] = 0, \quad \{[.]\} = [.], \quad \{\{.\}\} = \{.\} \tag{3.23}$$

The primal equation(3.13) for SIPG can be expressed as

$$\begin{aligned} &A\,(u_h, v) = \int_E \nabla u_h\,.(\kappa \nabla v)\, dx + \int_{\partial\Omega_i \cup \partial\Omega_D} {}^{\eta_e}\!/_{l_e} \left([v]\,[u_h] \right)\, ds \\ &- \int_{\partial\Omega_i \cup \partial\Omega_D} \left(\{\kappa \nabla u_h\}\,[v] \right) .\mathbf{n}\ ds - \int_{\partial\Omega_i \cup \partial\Omega_D} \left(\{\kappa\ \nabla v\ \}\,[u_h] \right) .\mathbf{n}\ ds \\ &L(v) := \int_E f\ v\ dx - \int_{\partial\Omega_D} (\kappa \nabla v)\,.\mathbf{n}\, u_D\, ds + \int_{\partial\Omega_D} {}^{\eta_e}\!/_{l_e} v\ u_D\, ds + \int_{\partial\Omega_N} v\ u_N\, ds \end{aligned} \tag{3.24}$$

NIPG and IIPG are different in that the bi-linear form is not symmetric. Following equation(3.13) all of the IP variants can be written as

$$\begin{aligned} A\left(u_h, v\right) &= \int_E \nabla u_h \left(\kappa \nabla v\right) dx + \int_{\partial\Omega_i \cup \partial\Omega_D} {}^{\eta_e}\!/_{l_e} \left([v]\,[u_h]\right)\, ds \\ &- \int_{\partial\Omega_i \cup \partial\Omega_D} \left(\{\kappa \nabla u_h\}\,[v]\right) .\mathbf{n}\ ds - \alpha \int_{\partial\Omega_i \cup \partial\Omega_D} \left(\{\kappa\, \nabla v\ \}\,[u_h]\right) .\mathbf{n}\ ds \\ L(v) &:= \int_E f\ v\ dx - \alpha \int_{\partial\Omega_D} \left(\kappa \nabla v\right) .\mathbf{n}\, u_D\ ds + \int_{\partial\Omega_D} {}^{\eta_e}\!/_{l_e} v\ u_D\ ds + \int_{\partial\Omega_N} v\ u_N\ ds \end{aligned} \tag{3.25}$$

3.3.2 Investigation of the consistency of the proposed fluxes

To check the consistency of the unified interior penalty in relation(3.25), another set of fluxes are investigated and the results are compared with the proposed formulation.

3.3.2.1 Babuška and M. Zlámal scheme

One straightforward choice of fluxes has been defined by Babuška and M. Zlámal (B-Z) [22] as

$$\begin{aligned} \hat{u} &= \hat{u}_b = u_h \\ \hat{\sigma}.\mathbf{n} &= \hat{\sigma}_b.\mathbf{n} = -{}^{\eta_e}\!/_{l_e}\,[u_h] \end{aligned} \tag{3.26}$$

Thus the weak form of the B-Z scheme is

$$\int_E \nabla u_h\, .(\kappa \nabla v)\, dx + \int_{\partial\Omega_i} {}^{\eta_e}\!/_{l_e} \left(\,[u]\,[v]\right)\ ds + \int_{\partial\Omega} {}^{\eta_e}\!/_{l_e} \left(\,[u]\, v\ \right)\ ds = \int_E f\ v\ dx \tag{3.27}$$

3.3.2.2 *An example about the consistency of the methods*

The B-Z method lacks the consistency and symmetry. For example consider the equation $-\Delta u = 2 \;\; 0 \leq \hat{x} \leq 1, \;\; 0 \leq \hat{y} \leq 1$, with Dirichlet boundary conditions, one exact solution to this equation is $u = -\hat{x}^2$. Choosing the test function as $v = 1$, the first term in equation(3.27) is equal to zero because $\nabla v = 0$, also second term is zero because $[v]$ is zero, and utilizing the exact solution in the remaining integrals gives

$$-{}^{\eta_e}\!/\!{}_{l_e}\left(\int_0^1 \hat{x}^2\Big|_{\hat{y}=1} d\hat{x} + \int_0^1 \hat{x}^2\Big|_{\hat{y}=0} d\hat{x} + \int_0^1 \hat{x}^2\Big|_{\hat{x}=1} d\hat{y}\right) \neq \int_E f\,dx = 2 \tag{3.28}$$

In the same fashion, equation(3.25) for the above example can be simplified to

$$\int_{\partial\Omega_D} {}^{\eta_e}\!/\!{}_{l_e}\,(u_h)\;ds - \int_{\partial\Omega_D} (\kappa\nabla u_h)\,.\mathbf{n}\;ds = \int_E f\,dx + \int_{\partial\Omega_D} {}^{\eta_e}\!/\!{}_{l_e}\,(u_D)\;ds \tag{3.29}$$

Substituting the exact solution $u = -\hat{x}^2$ in the remaining integrations gives us a similar relationship to the definition of conservative scheme in equation(3.17)

$$-\int_{\partial\Omega_D} (\kappa\nabla u_h)\,.\mathbf{n}\;ds = \int_E f\,dx \tag{3.30}$$

This is in fact the divergence theorem that results in

$$\int_{\partial\Omega_D} (2\hat{x})\,.\mathbf{n}\;ds = \int_0^1 (2\hat{x})\,|_{\hat{y}=1}\,d\hat{x} - \int_0^1 (2\hat{x})\,|_{\hat{y}=0}\,d\hat{x} + \int_0^1 (2\hat{x})\,|_{\hat{x}=1}\,d\hat{y} = \int_E f\,dx = 2 \tag{3.31}$$

Thus all of the IP variants for this example are consistent.

3.4 Interior penalty methods for linear elasticity equation

Similar to steps described in section(3.3), the so called primal equation for linear elasticity problems can be written as

$$\begin{aligned}
&A\left(\mathbf{u}_h, \mathbf{v}\right) = \int_E \nabla \mathbf{u}_h \;: \mathrm{K} : \nabla \mathbf{v}\, dx + \int_{\partial\Omega_i \cup \partial\Omega_D} {}^{\eta_e}\!/_{l_e} \left([\mathbf{v}] : [\mathbf{u}_h]\right)\, ds \\
&- \int_{\partial\Omega_i \cup \partial\Omega_D} \left(\{\mathrm{K} : \nabla \mathbf{u}_h\} : [\mathbf{v}]\right) \otimes \mathbf{n}\; ds - \alpha \int_{\partial\Omega_i \cup \partial\Omega_D} \left(\{\mathrm{K} : \nabla \mathbf{v}\} : [\mathbf{u}_h]\right) \otimes \mathbf{n}\; ds \qquad (3.32) \\
&L(\mathbf{v}) := \int_E \mathbf{f} \;: \mathbf{v}\, dx - \alpha \int_{\partial\Omega_D} \left((\mathrm{K} : \nabla \mathbf{v}) \;: \mathbf{u}_D\right) \otimes \mathbf{n}\, ds + \int_{\partial\Omega_D} {}^{\eta_e}\!/_{l_e} \mathbf{v} \;: \mathbf{u}_D\, ds + \int_{\partial\Omega_N} \mathbf{v} \;: \mathbf{u}_N\, ds
\end{aligned}$$

Vector variables $\mathbf{u}$, $\mathbf{v}$ and $\mathbf{f}$ are presented in this equation as opposed to scalar variables u, v and f used for Poisson equation. Additionally, K is the elasticity matrix, and the colon ":" and outer product $\otimes$ operators are defined as

$$\begin{aligned}
&\mathbf{x} : \mathbf{y} = \sum_{i\,j} \mathbf{x}_{ij}\, \mathbf{y}_{ij} \\
&\mathbf{x} : \mathbf{M} = \sum_{i\,j} \mathbf{x}_{ij}\, \mathbf{M}_{ijkl} \\
&\mathbf{M} : \mathbf{y} = \sum_{k\,l} \mathbf{M}_{ijkl}\, \mathbf{y}_{kl} \\
&\mathbf{x} \otimes \mathbf{y} = \mathbf{x}\, \mathbf{y}^T
\end{aligned} \qquad (3.33)$$

where $\mathbf{x}$, $\mathbf{y}$ are vectors and $\mathbf{M}$ is a matrix. Detailed definition and implementation procedure of each term in equations(3.32) and (3.25) is presented in the next section.

3.5 Discretization and numerical implementation

For implementing the DG primal equations for the Poisson and linear elasticity the displacement vector **u** is discretized over each element with standard finite element procedure. This discretization is illustrated in figure(3.2).

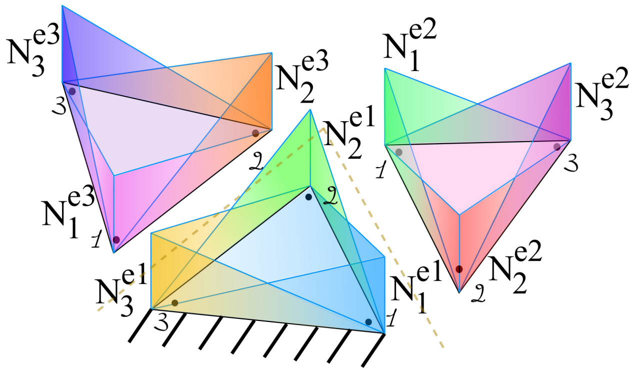

Figure 3.2 Illustration of discontinuity between the shape functions and element nodes in adjacent elements in two dimensional discontinuous Galerkin formulation

In three dimensional space $\mathbf{u} \in \Omega \subset \mathbb{R}^3$, and can be discretized as $\mathbf{u} \approx \sum N_i \mathbf{u}_i$. The following matrices are given to express the primal equations of linear elasticity in standard matrix form. Defining

$$\bar{\mathrm{N}} = \left[\begin{array}{ccc|ccc|c} N_1 & 0 & 0 & N_2 & 0 & 0 & \\ 0 & N_1 & 0 & 0 & N_2 & 0 & \cdots \\ 0 & 0 & N_1 & 0 & 0 & N_2 & \end{array}\right], \quad \mathbf{n} = \begin{bmatrix} n_x & 0 & 0 & 0 & n_z & n_y \\ 0 & n_y & 0 & n_z & 0 & n_x \\ 0 & 0 & n_z & n_y & n_x & 0 \end{bmatrix}^T$$

$$\bar{\mathrm{B}} = \left[\begin{array}{ccc|ccc|c} N_{1,x} & 0 & 0 & N_{2,x} & 0 & 0 & \\ 0 & N_{1,y} & 0 & 0 & N_{2,y} & 0 & \\ 0 & 0 & N_{1,z} & 0 & 0 & N_{2,z} & \cdots \\ 0 & N_{1,z} & N_{1,y} & 0 & N_{2,z} & N_{2,y} & \\ N_{1,z} & 0 & N_{1,x} & N_{2,z} & 0 & N_{2,x} & \\ N_{1,y} & N_{1,x} & 0 & N_{2,y} & N_{2,x} & 0 & \end{array}\right] \tag{3.34}$$

where $*_{,x}$ indicates the derivative of $*$ with respect to variable x and n_x, n_y and n_z are the components of the normal vector in the Cartesian coordinates. $\bar{B}$ is referred to as the strain-displacement matrix. Implementing these relations, the following terms may be expressed as

$$\mathbf{u} = \bar{\mathrm{N}}.\mathrm{U}, \quad \nabla\mathbf{u} = \bar{\mathrm{B}}.\mathrm{U} \tag{3.35}$$

The following sections are devoted to describe the implementation procedure of the primal equations of linear elasticity and Poisson equation. Expanded version of these relations are provided for two dimensional implementations. For the two dimensional problems the elasticity or constitutive matrix K will be defined in general as

$$\mathrm{K} = \begin{bmatrix} d_{11} & d_{12} & d_{13} \\ d_{21} & d_{22} & d_{23} \\ d_{31} & d_{32} & d_{33} \end{bmatrix} \tag{3.36}$$

3.5.1 LHS loops

Calculation of the LHS, or the bi-linear term, requires three loops. These consist of one over the elements, one over the interior boundaries of element, and one over the Dirichlet boundaries.

3.5.1.1 Domain loop

The domain loop is similar to the Continuous Galerkin (CG) formulation and the description of this implementation is provided in standard CG books.

$$\int_E \nabla \mathbf{u}_h : \mathrm{K} : \nabla \mathbf{v}\, dx = \int_E \bar{\mathrm{B}}^T\ \mathrm{K}\, \bar{\mathrm{B}}.\mathrm{U}\, \mathrm{dx} \tag{3.37}$$

3.5.1.2 Interior faces loop

Unlike the CG formulation, there is an internal boundary loop in DG. The implementation is illustrated in algorithm(1) where W_e and J_e are the weight and Jacobian associated with each Gauss point on the boundary segment. Table(3.1) defines the parameters of algorithm(1) for each corresponding integral for linear elasticity. In this integration, the nodes that corresponds to an interior face from adjacent elements are involved. Expansion of the involved terms in the interior loop are provided in equations(3.38), (3.39) and (3.40). Careful attention should be taken for the sign of variable β during the calculations. This variable can be +1 or −1 according to the multiplication sign of the jumps in $(u_2 - u_1) \times (v_2 - v_1)$. Although the integration is performed over the faces, other elemental shape functions contribute to this integral. Assuming that the Lagrange shape functions are used for the interpolations, non-adjacent shape functions to the face are zero in the integration, but may have non-zero derivatives along this face and should be accounted for during the integration.

Table(3.2) defines the parameters of algorithm(1) for each corresponding integral for Poisson equation and expansion of the involved terms in the interior loop are provided in equation(3.41).

Algorithm 1 Interior face integration

```
Loop (e) over every interior face
Loop over line Gauss points
Loop (i) over both sides of the face param1
Loop (j) over both sides of the face param2
$A\left[\bar{c}\left(\mathbf{u}_h, \mathbf{v}\right)\right] += W_e \times J_e \times \left(\bar{k}_1 + \bar{k}_2 + \bar{k}_3\right)$
```

Table 3.1 Description of parameters in algorithm(1) for defining the stiffness matrix in linear elasticity

$Term$	$equation$	$param1$	$param2$
$\bar{k}_1$	$\int_{\partial\Omega_i} {}^{\eta_e}/_{l_e} \left([\mathbf{v}] : [\mathbf{u}_h]\right) \, ds$	face shape functions	face shape functions
$\bar{k}_2$	$-\int_{\partial\Omega_i} \left(\{\mathrm{K} : \nabla\mathbf{u}_h\} : [\mathbf{v}]\right) \otimes \mathbf{n} \, ds$	face shape functions	elemental shape functions
$\bar{k}_3$	$-\alpha \int_{\partial\Omega_i} \left(\{\mathrm{K} : \nabla\mathbf{v}\} : [\mathbf{u}_h]\right) \otimes \mathbf{n} \, ds$	face shape functions	elemental shape functions

$$
\begin{aligned}
&\bar{k}_1[1,1] = {}^{\eta_e}\!/_{l_e} \times \beta \times N_i \times N_j, \quad \bar{k}_1[1,2] = 0 \\
&\bar{k}_1[2,1] = 0, \quad \bar{k}_1[2,2] = {}^{\eta_e}\!/_{l_e} \times \beta \times N_i \times N_j
\end{aligned}
\tag{3.38}
$$

$$
\begin{aligned}
\bar{k}_2[1,1] &= -\beta \times \left\{N_{j,x}\left(\tfrac{d_{11}N_i \times n_x + d_{31}N_i \times n_y}{2}\right) + N_{j,y}\left(\tfrac{d_{13}N_i \times n_x + d_{33}N_i \times n_y}{2}\right)\right\} \\
\bar{k}_2[1,2] &= -\beta \times \left\{N_{j,y}\left(\tfrac{d_{12}N_i \times n_x + d_{32}N_i \times n_y}{2}\right) + N_{j,x}\left(\tfrac{d_{13}N_i \times n_x + d_{33}N_i \times n_y}{2}\right)\right\} \\
\bar{k}_2[2,1] &= -\beta \times \left\{N_{j,x}\left(\tfrac{d_{31}N_i \times n_x + d_{21}N_i \times n_y}{2}\right) + N_{j,y}\left(\tfrac{d_{33}N_i \times n_x + d_{23}N_i \times n_y}{2}\right)\right\} \\
\bar{k}_2[2,2] &= -\beta \times \left\{N_{j,y}\left(\tfrac{d_{32}N_i \times n_x + d_{22}N_i \times n_y}{2}\right) + N_{j,x}\left(\tfrac{d_{33}N_i \times n_x + d_{23}N_i \times n_y}{2}\right)\right\}
\end{aligned}
\tag{3.39}
$$

$$
\begin{aligned}
\bar{k}_3[1,1] &= -\alpha \times \beta \times N_i \left\{\left(\tfrac{d_{11}N_{j,x} + d_{31}N_{j,y}}{2}\right) n_x + \left(\tfrac{d_{13}N_{j,x} + d_{33}N_{j,y}}{2}\right) n_y\right\} \\
\bar{k}_3[1,2] &= -\alpha \times \beta \times N_i \left\{\left(\tfrac{d_{13}N_{j,x} + d_{33}N_{j,y}}{2}\right) n_x + \left(\tfrac{d_{12}N_{j,x} + d_{32}N_{j,y}}{2}\right) n_y\right\} \\
\bar{k}_3[2,1] &= -\alpha \times \beta \times N_i \left\{\left(\tfrac{d_{31}N_{j,x} + d_{21}N_{j,y}}{2}\right) n_x + \left(\tfrac{d_{33}N_{j,x} + d_{23}N_{j,y}}{2}\right) n_y\right\} \\
\bar{k}_3[2,2] &= -\alpha \times \beta \times N_i \left\{\left(\tfrac{d_{33}N_{j,x} + d_{23}N_{j,y}}{2}\right) n_x + \left(\tfrac{d_{32}N_{j,x} + d_{22}N_{j,y}}{2}\right) n_y\right\}
\end{aligned}
\tag{3.40}
$$

Table 3.2 Description of parameters in algorithm(1) for defining the stiffness matrix in Poisson equation

$Term$	$equation$	$param1$	$param2$
$\bar{k}_1$	$\int_{\partial\Omega_i} {}^{\eta_e}\!/_{l_e} \left([v]\,[u_h]\right)\, ds$	face shape functions	face shape functions
$\bar{k}_2$	$-\int_{\partial\Omega_i} \left(\{\kappa\nabla u_h\}\,[v]\right) .\mathbf{n}\; ds$	face shape functions	elemental shape functions
$\bar{k}_3$	$-\alpha\int_{\partial\Omega_i} \left(\{\kappa\,\nabla v\,\}\,[u_h]\right) .\mathbf{n}\; ds$	face shape functions	elemental shape functions

$$
\begin{aligned}
\bar{k}_1 &= {}^{\eta_e}\!/_{l_e} \times \beta \times N_i \times N_j \\
\bar{k}_2 &= -\beta \times N_j \times \kappa/2 \left\{ N_{i,x} n_x + N_{i,y} n_y \right\} \\
\bar{k}_3 &= -\alpha \times \beta \times N_i \times \kappa/2 \left\{ N_{j,x} n_x + N_{j,y} n_y \right\}
\end{aligned}
\tag{3.41}
$$

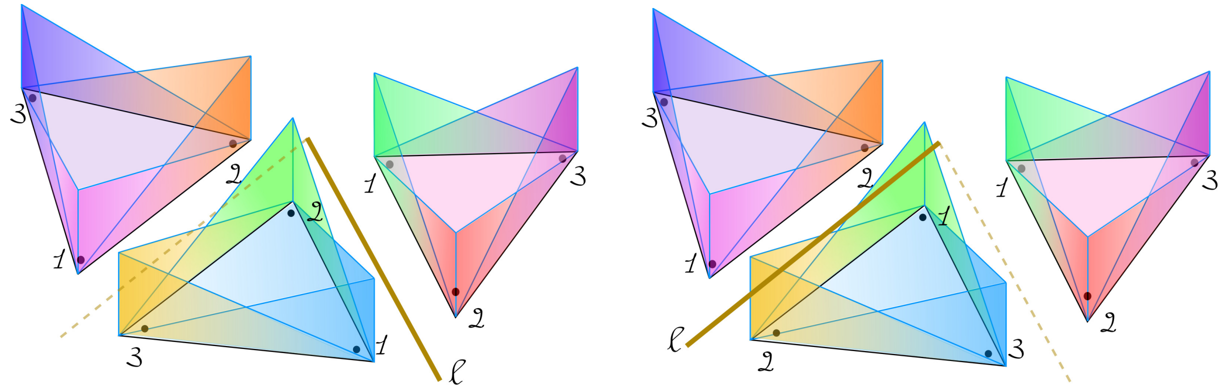

(a) Integral face is highlighted

(b) Integral face is highlighted

Figure 3.3 Reordering the elemental shape functions according to corresponding face integration

Care is needed in performing the face integration in a consistent way; that is, to utilize the appropriate element shape functions. This is accomplished by reordering the elemental shape functions in neighbor elements according to the face being integrated. This procedure is illustrated in figure(3.3).

3.5.1.3 Dirichlet boundary loop

To calculate the stiffness matrix in the DG primal form, another loop over the Dirichlet boundary faces should be performed. This procedure is described in algorithm(2). Tables(3.3) and (3.4) explain the parameters of this loop for the linear elastic and the Poisson equations, respectively. The expanded equations of these terms are defined in equations(3.42), (3.43) and (3.44) for the linear elasticity and in equation(3.45) for the Poisson equation. Logical parameter $\vee$ or $'or'$ indicates the possibility of existence mixed boundary conditions in the boundary segments, meaning that the segments can have Dirichlet boundary on one primary variable and Neumann on other directions. The terms in algorithm(2) should only be implemented in the Dirichlet or constrained directions of the boundary faces.

Algorithm 2 Integration over Dirichlet Boundary faces.

```
Loop (e) over every Dirichlet boundary faces
Loop over line Gauss points
Loop (i) over param1
Loop (j) over param2
$A\left[\bar{c}\left(\mathbf{u}_h, \mathbf{v}\right)\right] += W_e \times J_e \times \left(\hat{k}_1 + \hat{k}_2 + \hat{k}_3\right)$
```

Table 3.3 Description of parameters in algorithm(2) for defining the stiffness matrix for linear elasticity

$Term$	$equation$	$param1$	$param2$
$\hat{k}_1$	$\int_{\partial\Omega_D} {}^{\eta_e}/_{l_e} \left([\mathbf{v}] : [\mathbf{u}_h]\right)\, ds$	face shape functions	face shape functions
$\hat{k}_2$	$-\int_{\partial\Omega_D} \left(\{\mathrm{K} : \nabla\mathbf{u}_h\} : [\mathbf{v}]\right) \otimes \mathbf{n}\, ds$	face shape functions	elemental shape functions
$\hat{k}_3$	$-\alpha \int_{\partial\Omega_D} \left(\{\mathrm{K} : \nabla\mathbf{v}\} : [\mathbf{u}_h]\right) \otimes \mathbf{n}\, ds$	face shape functions	elemental shape functions

$$\begin{gathered}\hat{k}_1[1,1] = {}^{\eta_e}\!/_{l_e} \times N_i \times N_j \ \vee\ 0, \quad \hat{k}_1[1,2] = 0 \\ \hat{k}_1[2,1] = 0, \quad \hat{k}_1[2,2] = {}^{\eta_e}\!/_{l_e} \times N_i \times N_j \ \vee\ 0\end{gathered} \tag{3.42}$$

$$\begin{aligned}\hat{k}_2[1,1] &= -1 \times \left\{N_{j,x}\left(d_{11}N_i \times n_x + d_{31}N_i \times n_y\right) + N_{j,y}\left(d_{13}N_i \times n_x + d_{33}N_i \times n_y\right)\right\} \ \vee\ 0 \\ \hat{k}_2[1,2] &= -1 \times \left\{N_{j,y}\left(d_{12}N_i \times n_x + d_{32}N_i \times n_y\right) + N_{j,x}\left(d_{13}N_i \times n_x + d_{33}N_i \times n_y\right)\right\} \ \vee\ 0 \\ \hat{k}_2[2,1] &= -1 \times \left\{N_{j,x}\left(d_{31}N_i \times n_x + d_{21}N_i \times n_y\right) + N_{j,y}\left(d_{33}N_i \times n_x + d_{23}N_i \times n_y\right)\right\} \ \vee\ 0 \\ \hat{k}_2[2,2] &= -1 \times \left\{N_{j,y}\left(d_{32}N_i \times n_x + d_{22}N_i \times n_y\right) + N_{j,x}\left(d_{33}N_i \times n_x + d_{23}N_i \times n_y\right)\right\} \ \vee\ 0\end{aligned} \tag{3.43}$$

$$\begin{aligned}\hat{k}_3[1,1] &= -\alpha \times N_i \left\{\left(d_{11}N_{j,x} + d_{31}N_{j,y}\right)n_x + \left(d_{13}N_{j,x} + d_{33}N_{j,y}\right)n_y\right\} \ \vee\ 0 \\ \hat{k}_3[1,2] &= -\alpha \times N_i \left\{\left(d_{13}N_{j,x} + d_{33}N_{j,y}\right)n_x + \left(d_{12}N_{j,x} + d_{32}N_{j,y}\right)n_y\right\} \ \vee\ 0 \\ \hat{k}_3[2,1] &= -\alpha \times N_i \left\{\left(d_{31}N_{j,x} + d_{21}N_{j,y}\right)n_x + \left(d_{33}N_{j,x} + d_{23}N_{j,y}\right)n_y\right\} \ \vee\ 0 \\ \hat{k}_3[2,2] &= -\alpha \times N_i \left\{\left(d_{33}N_{j,x} + d_{23}N_{j,y}\right)n_x + \left(d_{32}N_{j,x} + d_{22}N_{j,y}\right)n_y\right\} \ \vee\ 0\end{aligned} \tag{3.44}$$

Table 3.4 Description of parameters in relation(2) for defining the stiffness matrix in Poisson equation

$Term$	$equation$	$param1$	$param2$
$\hat{k}_1$	$\int_{\partial\Omega_D} {}^{\eta_e}\!/_{l_e} \left([v]\,[u_h]\right)\, ds$	face shape functions	face shape functions
$\hat{k}_2$	$-\int_{\partial\Omega_D} \left(\{\kappa\nabla u_h\}\,[v]\right).\mathbf{n}\ ds$	face shape functions	elemental shape functions
$\hat{k}_3$	$-\alpha\int_{\partial\Omega_D} \left(\{\kappa\,\nabla v\,\}\,[u_h]\right).\mathbf{n}\ ds$	face shape functions	elemental shape functions

$$\begin{aligned}
\hat{k}_1 &= {}^{\eta_e}\!/_{l_e} \times N_i \times N_j \\
\hat{k}_2 &= -1 \times N_j \times \kappa/2 \left\{ N_{i,x} n_x + N_{i,y} n_y \right\} \\
\hat{k}_3 &= -\alpha \times N_i \times \kappa/2 \left\{ N_{j,x} n_x + N_{j,y} n_y \right\}
\end{aligned} \tag{3.45}$$

3.5.2 RHS loops

There are four loops to calculate in the linear form or RHS of the primal equation.

3.5.2.1 Domain loop and Neumann boundary loop

RHS loops corresponding to the body forces and Neumann boundary conditions are given by

$$L\left[\bar{c}\left(\mathbf{v}\right)\right] + = \int_E \mathbf{f} \; : \mathbf{v} \, dx \tag{3.46}$$

$$L\left[\bar{c}\left(\mathbf{v}\right)\right] + = \int_{\partial\Omega_N} \mathbf{v} \; : \mathbf{u}_N \, ds \tag{3.47}$$

Since these integrals are performed in a similar manner as their CG counter parts they will not be discussed.

3.5.2.2 Dirichlet boundary loop

In DG the Dirichlet boundary conditions are imposed weakly. Implementation is shown in algorithm(3). This loop can be carried out along with the Dirichlet boundary loop in the calculation of the LHS for the stiffness matrix. Tables(3.5) and (3.6) explain the parameters of this loop for the linear elastic and the Poisson equations, respectively. The expanded version of these terms are defined in equations(3.48) and (3.49) for the linear elasticity and in equation(3.50) for the Poisson equation.

Algorithm 3

```
1: Loop (e) over every Dirichlet boundary faces
2: Loop over line Gauss points
3: Loop (i) over param1
4: $|L\left[\bar{c}\left(\mathbf{v}\right)\right] += W_e \times J_e \times (\hat{r}_1 + \hat{r}_2)$
```

Table 3.5 Description of parameters in relation(3) for defining the RHS vector in linear elasticity

$Term$	$equation$	$param1$
$\hat{r}_1$	$\int_{\partial\Omega_D} {}^{\eta_e}\!/_{l_e}\mathbf{v} : \mathbf{u}_D \, ds$	face shape functions
$\hat{r}_2$	$-\alpha \int_{\partial\Omega_D} ((\mathrm{K} : \nabla\mathbf{v}) : \mathbf{u}_D) \otimes \mathbf{n} \, ds$	elemental shape functions

$$\begin{aligned} \hat{r}_1[1] &= {}^{\eta_e}\!/_{l_e} \times N_i \times u_{Dx} \\ \hat{r}_1[2] &= {}^{\eta_e}\!/_{l_e} \times N_i \times u_{Dy} \end{aligned} \tag{3.48}$$

$$
\hat{r}_2[1] = -\alpha \times \left(\begin{array}{l} u_{Dx} \left\{ \left(d_{11} N_{i,x} + d_{31} N_{i,y} \right) n_x + \left(d_{13} N_{i,x} + d_{33} N_{i,y} \right) n_y \right\} \\ +u_{Dy} \left\{ \left(d_{13} N_{i,x} + d_{33} N_{i,y} \right) n_x + \left(d_{12} N_{i,x} + d_{32} N_{i,y} \right) n_y \right\} \end{array} \right)
$$
$$
\hat{r}_2[2] = -\alpha \times \left(\begin{array}{l} u_{Dx} \left\{ \left(d_{31} N_{i,x} + d_{21} N_{i,y} \right) n_x + \left(d_{33} N_{i,x} + d_{23} N_{i,y} \right) n_y \right\} \\ +u_{Dy} \left\{ \left(d_{33} N_{i,x} + d_{23} N_{i,y} \right) n_x + \left(d_{32} N_{i,x} + d_{22} N_{i,y} \right) n_y \right\} \end{array} \right) \tag{3.49}
$$

Table 3.6 Description of parameters in relation(3) for defining the RHS vector in Poisson equation

$Term$	$equation$	$param1$
$\hat{r}_1$	$\int_{\partial\Omega_D} {}^{\eta_e}\!/_{l_e} v\, u_D\, ds$	face shape functions
$\hat{r}_2$	$-\alpha \int_{\partial\Omega_D} (\kappa \nabla v)\, .\mathbf{n}\, u_D\, ds$	elemental shape functions

$$
\begin{aligned}
\hat{r}_1 &= {}^{\eta_e}\!/_{l_e} \times N_i \times u_D \\
\hat{r}_2 &= -\alpha \times u_D \times \kappa \left\{ N_{i,x} n_x + N_{i,y} n_y \right\}
\end{aligned} \tag{3.50}
$$

3.6 Numerical results

In this section, examples for both Poisson and the linear elastic equations are given. The examples are carefully selected to cover a wide range of boundary conditions and body forces. For some examples, exact solutions are available for verification and error analysis of the current implementation.

3.6.1 Results of Poisson equation

Three examples with different boundary conditions and body forces are shown for the Poisson equation. In the first example, only Dirichlet boundary conditions are defined. In the second example, body force is added to the equation as a source term and in the third example combination of Dirichlet and Neumann boundary conditions with body force is examined. Figures(3.5), (3.7) and (3.9) show the error of these examples which is computed as the difference between the exact and the numerical results of the simulation. Good agreement of results between the numerical and exact solutions is illustrated in figures(3.4), (3.6) and (3.8) for these threes examples in the presented order. Second order reduction logarithm of integral of the L^2 norm of error over the domain for these examples versus the logarithm of elemental length for linear triangle elements is displayed in figure(3.10) that shows the consistency of the numerical method.

3.6.1.1 Problem with known Dirichlet boundary condition for symmetric interior penalty

Boundary conditions and the problem definition is described in relation(3.51). Symmetric interior penalty is chosen for this problem.

$$\begin{aligned}
&\nabla^2 u = 0 \;\; in \; \Omega := (0 < x < a) \cap (0 < y < b) \\
&u(0, y) = u(\pi, y) = u(x, 0) = 0, \;\; u(x, 0) = w_0 \times Sin(\tfrac{\pi x}{a}) \\
&Exact\ Solution = \frac{w_0}{Sinh(\frac{\pi b}{a})} \times Sin(\tfrac{\pi x}{a}) \times Sinh(\tfrac{\pi y}{a}) \\
&Defining \;\; w_0 = 2, \;\; a = b = \pi
\end{aligned} \tag{3.51}$$

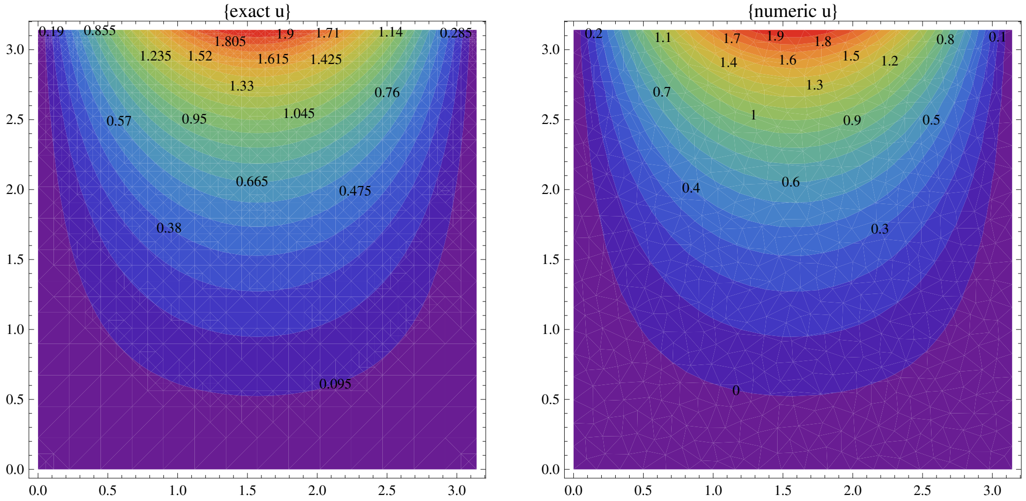

(a) Deformation in Exact solution

(b) Deformation in numerical solution

Figure 3.4 Comparison of exact and numerical solution of Poisson equation for Dirichlet boundary condition

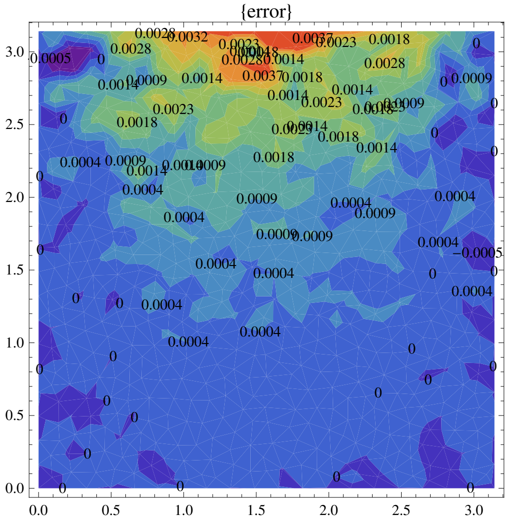

Figure 3.5 Error of numerical solution of Poisson equation for Dirichlet boundary condition

3.6.1.2 Problem with known Dirichlet boundary condition and body force for non-symmetric interior penalty

Boundary conditions and the problem definition is described in equation(3.52). Non-symmetric interior penalty is selected for the solution of this problem.

$$
\begin{aligned}
&\nabla^2 u = x \times y \ \ in\ \Omega := (0 < x < a) \cap (0 < y < b)\\
&Defining\ a = b = \pi\\
&u(0, y) = u(x, 0) = 0,\ \ u(a, y) = \tfrac{\pi}{6} \times y^3,\ \ u(x, b) = \tfrac{x}{6} \times \pi^3 + Sin(x) \times Sinh(\pi)\\
&Exact\ Solution = \tfrac{x}{6} \times y^3 + Sin(x) \times (\sum_{i=1}^{n} \tfrac{y^{(2\times i-1)}}{(2\times i-1)!})
\end{aligned}
\tag{3.52}
$$

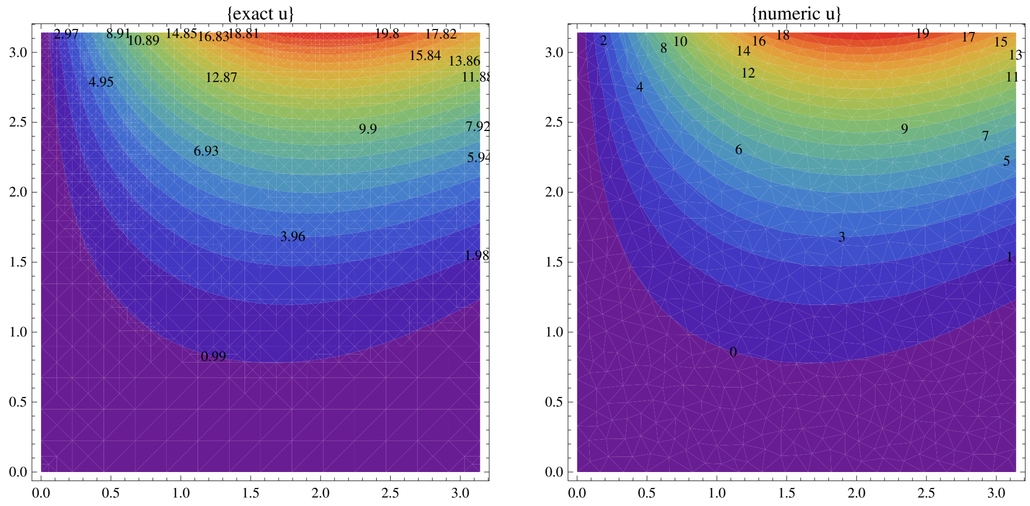

(a) Deformation in Exact solution

(b) Deformation in numerical solution

Figure 3.6 Comparison of exact and numerical solution of Poisson equation for Dirichlet boundary condition and body force

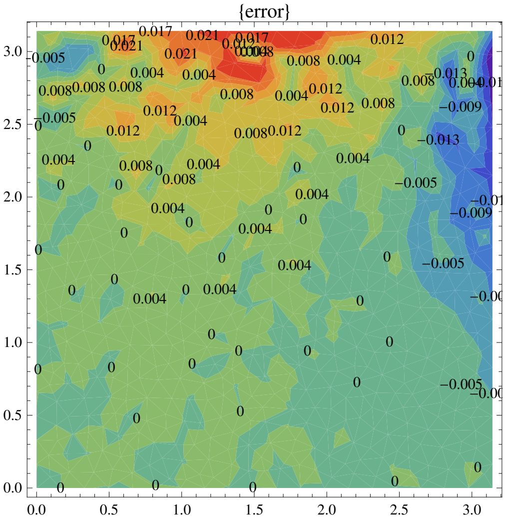

Figure 3.7 Error of numerical solution of the Poisson equation for Dirichlet boundary condition and body force

3.6.1.3 Problem with known Dirichlet and Neumann boundary condition and body force for incomplete interior penalty

Boundary conditions and the problem definition is described in equation(3.53). For the numerical solution, incomplete interior penalty method is selected.

$$
\begin{aligned}
&\nabla^2 u = x \times y \;\; in\; \Omega := (0 < x < a) \cap (0 < y < b)\\
&Defining\;\; a = b = \pi\\
&\tfrac{\partial u}{\partial x}.\mathbf{n}(0, y) = -\tfrac{y^3}{6},\; \tfrac{\partial u}{\partial x}.\mathbf{n}(a, y) = \tfrac{y^3}{6},\;\; u(x, 0) = Cos(x), \qquad (3.53)\\
&\tfrac{\partial u}{\partial y}.\mathbf{n}(x, b) = \tfrac{x}{2} \times \pi^2 + Cos(x) \times (Cosh(\pi) + Sinh(\pi))\\
&Exact\; Solution = \tfrac{x}{6} \times y^3 + Cos(x) \times (1 + \sum_{i=1}^{n} \tfrac{y^i}{i!})
\end{aligned}
$$

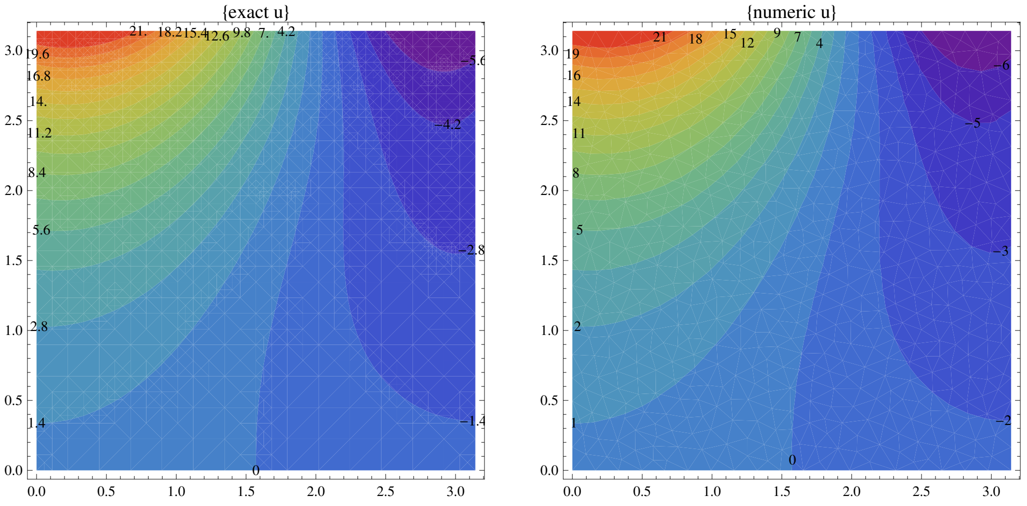

(a) Deformation in Exact solution

(b) Deformation in numerical solution

Figure 3.8 Comparison of exact and numerical solution of Poisson equation for Dirichlet and Neumann boundary condition and body force

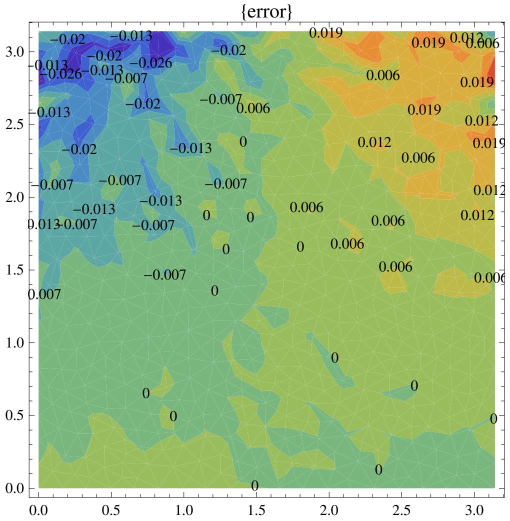

Figure 3.9 Error of numerical solution of Poisson equation for Dirichlet and Neumann boundary condition and body force

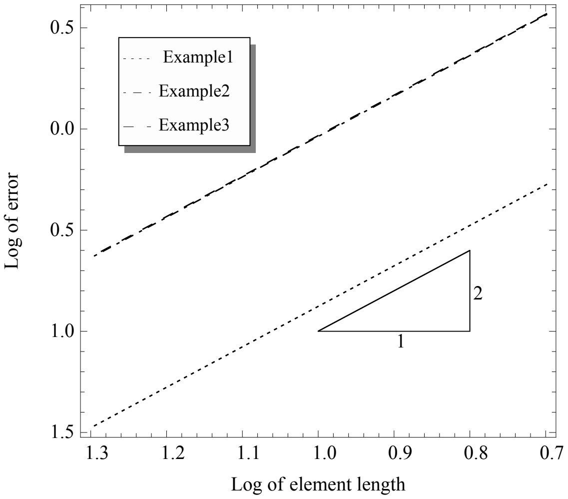

Figure 3.10 Error reduction analysis for the Poisson equation examples in finer elements

3.6.2 Results of linear elasticity

Three examples are selected for the analysis of the DG method for linear elastic problems. The examples are carefully selected to cover different boundary conditions and geometries.

3.6.2.1 Linear elastic example 1

A square plate fixed at the boundaries and under body force of $\mathbf{f}$ is investigated for this example. The symmetric interior penalty scheme is used for the simulation. The problem is defined as

$$
\begin{aligned}
&-\bar{B}^T(\mathbf{K}\bar{B}\mathbf{u}) = \mathbf{f} \;\; in \quad -1 \le x \le 1, \; -1 \le y \le 1, \\
&\mathbf{u} = 0 \;\; on \; \partial\Omega_D, \;\; \lambda = 0.3, \;\; \mu = 0.35 \\
&\mathbf{K} = \begin{bmatrix} \lambda & 2\mu+\lambda & 0 \\ 2\mu+\lambda & \lambda & 0 \\ 0 & 0 & \mu \end{bmatrix}, \;\; \mathbf{f} = \begin{bmatrix} -2\mu(3 - x^2 - 2y^2 - 2xy) - \lambda(2 - 2y^2 - 4xy) \\ -2\mu(3 - 2x^2 - y^2 - 2xy) - \lambda(2 - 2x^2 - 4xy) \end{bmatrix}
\end{aligned}
\tag{3.54}
$$

And the exact solution for this problem is

$$
\mathbf{u} = \begin{bmatrix} (1-x^2)(1-y^2) \\ (1-x^2)(1-y^2) \end{bmatrix} \tag{3.55}
$$

The numerical displacements or ($u = \mathbf{u_1}, v = \mathbf{u_2}$) are shown in figure(3.11). Second order reduction of logarithm of L^2 norm of error with decreasing element size is expected for linear triangle elements and is shown in figure(3.12).

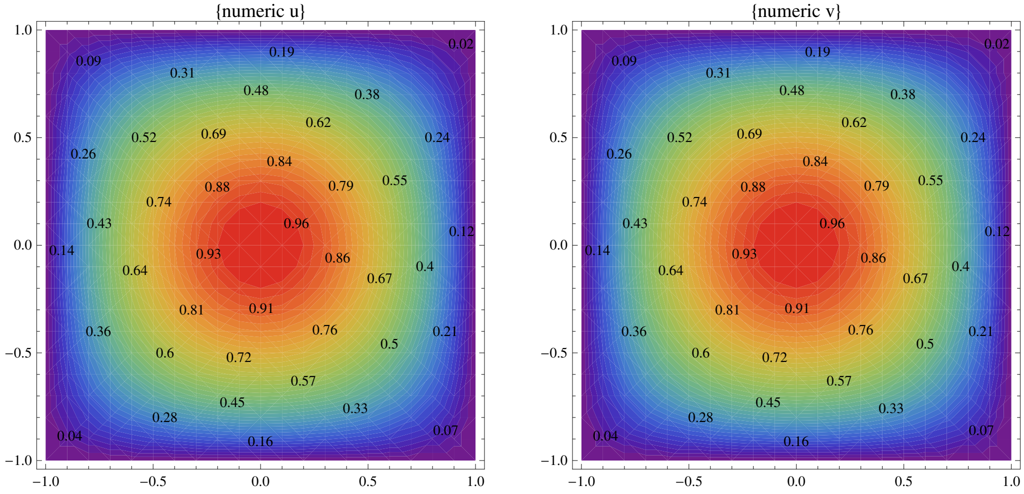

(a) u or $\mathbf{u_1}$

(b) v or $\mathbf{u_2}$

Figure 3.11 Numerical deformation of plate in x and y directions for the first example

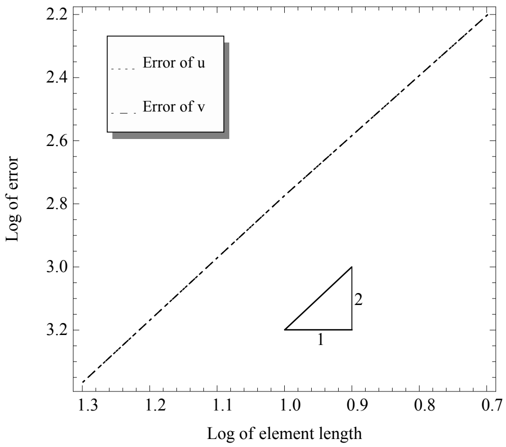

Figure 3.12 Reduction of error with reduction of element size

3.6.2.2 Linear elastic example 2

For the second problem illustrated in figure(3.13), a plate is hinged at $x = -1$, $y = -1$ and under constant tension at $x = 1$. The constitutive matrix for this problem is

$$\mathbf{K} = \begin{bmatrix} 1.2 & 0.4 & 0 \\ 0.4 & 1.2 & 0 \\ 0 & 0 & 0.4 \end{bmatrix} \tag{3.56}$$

The computed deflections of the plate is shown in figure(3.14). Furthermore, this problem can be solved analytically and the numerical error, i.e. the difference between the numerical and exact solution, is depicted in figure(3.15).

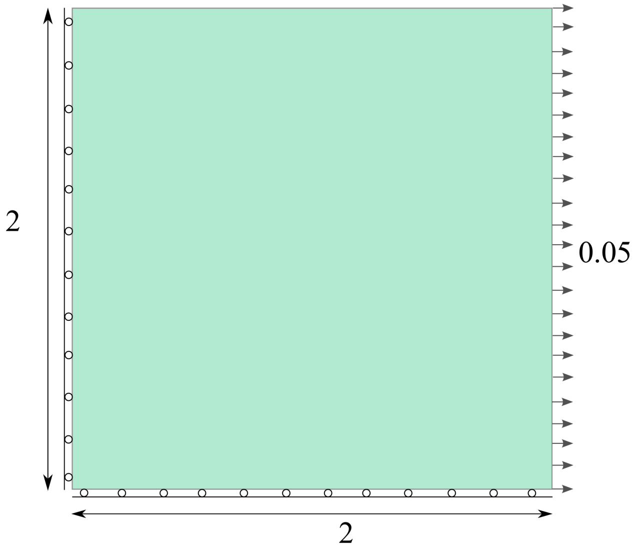

Figure 3.13 Problem configuration of the second example

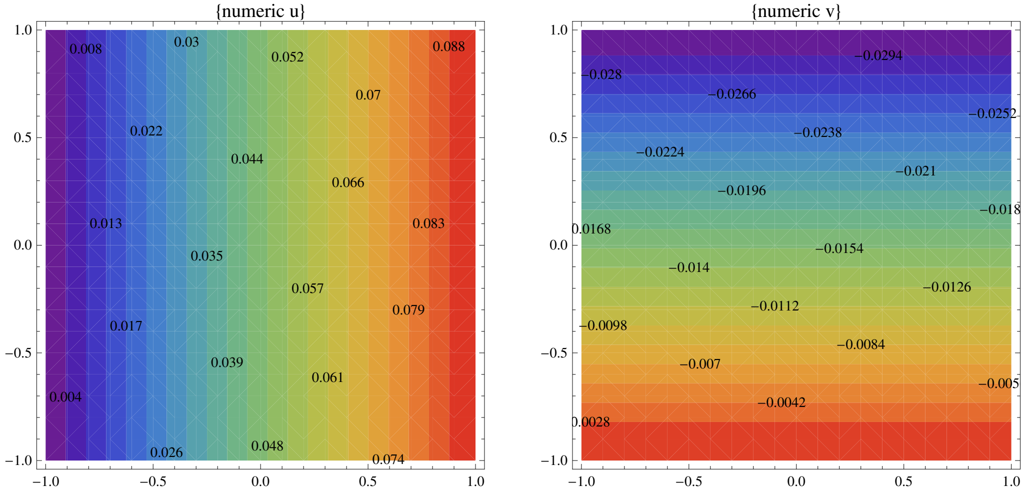

(a) u or $\mathbf{u_1}$

(b) v or $\mathbf{u_2}$

Figure 3.14 Numerical deformation of plate in x and y directions for the second example

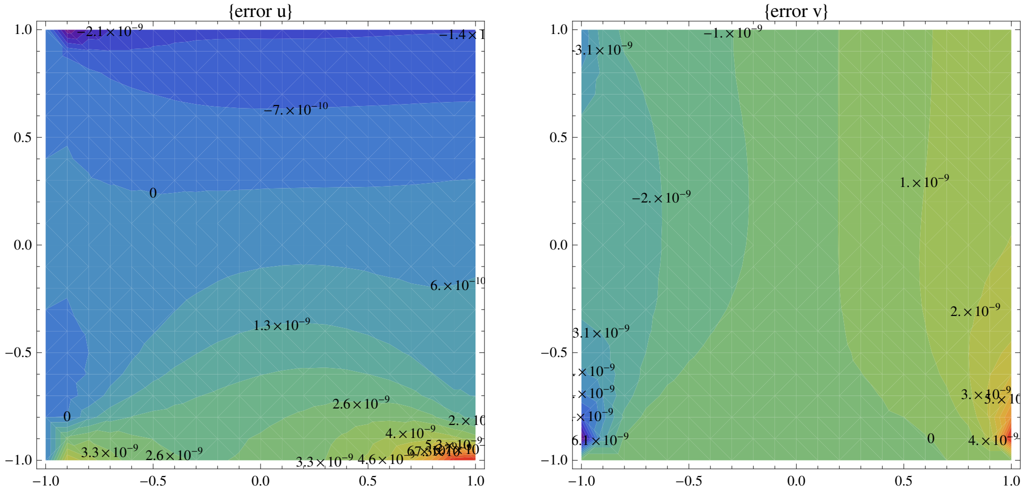

(a) Numerical error of v or $\mathbf{u_2}$

(b) Numerical error of v or $\mathbf{u_2}$

Figure 3.15 Numerical error in x and y directions for the second example

3.6.2.3 Plate with hole

For the last problem, a rectangular plate with a hole as described in figure(3.16) is solved under the plane stress assumption and with the developed symmetric interior penalty DG algorithm. The dimenesions in this figure are inch for the length and pound for the boundary force. The plate has the material properties of Aluminum, and are given as

$$E = 10600ksi, \;\; \nu = 0.33 \tag{3.57}$$

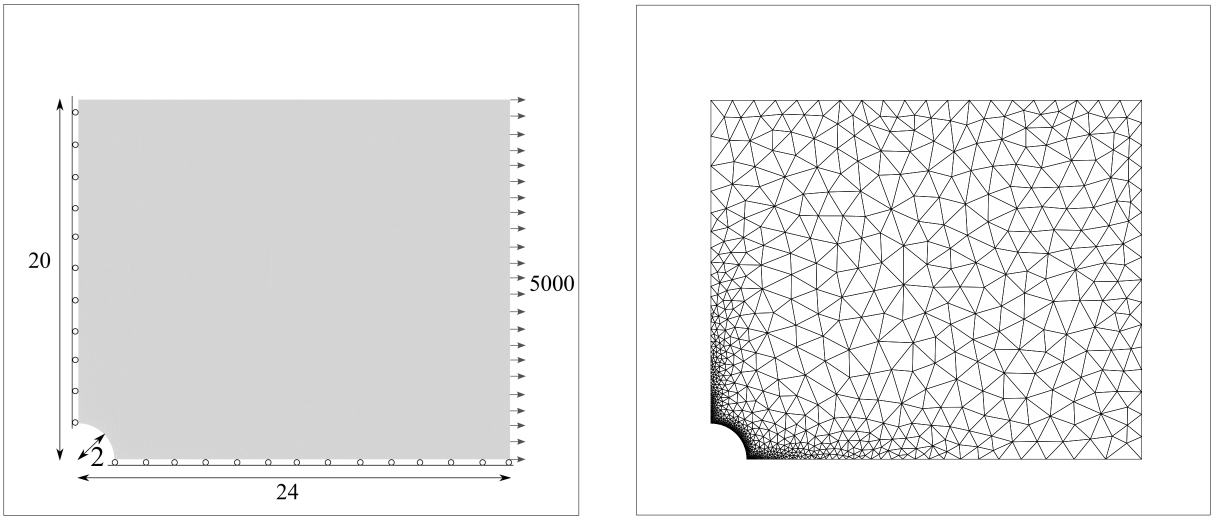

(a) (b)

Figure 3.16 Configuration and meshing of the problem

Deformation and stress contours of the plate are depicted in figures(3.17), (3.18) and (3.19).

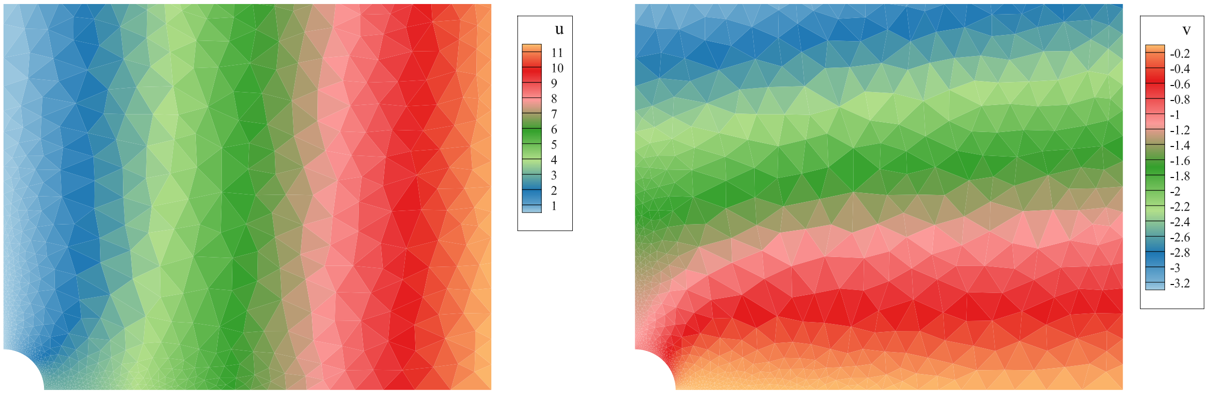

(a) Deformation in $\mathbf{u_1}$ direction

(b) Deformation in $\mathbf{u_2}$ direction

Figure 3.17 Deformation of the third linear elasticity example

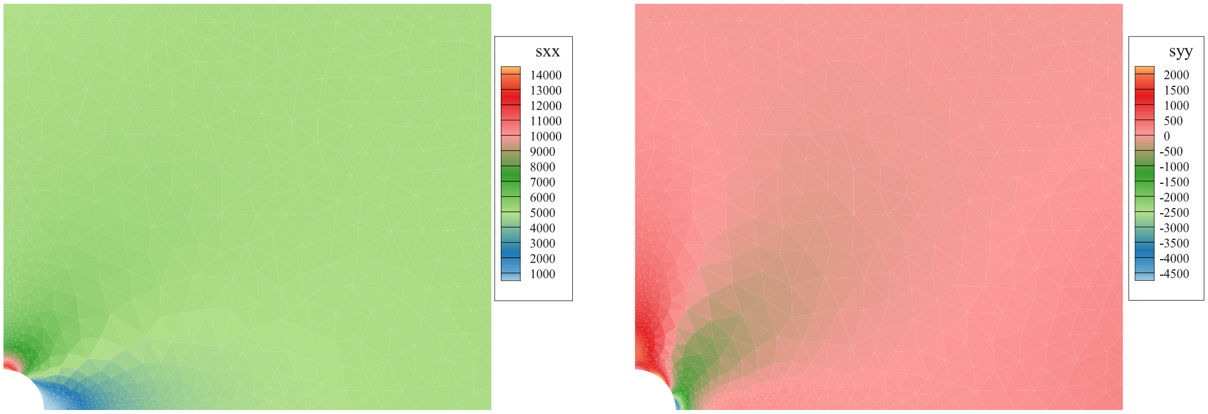

(a) Normal stress of the plate

(b) Transverse normal stress of the plate

Figure 3.18 Stress contours of the third linear elasticity example

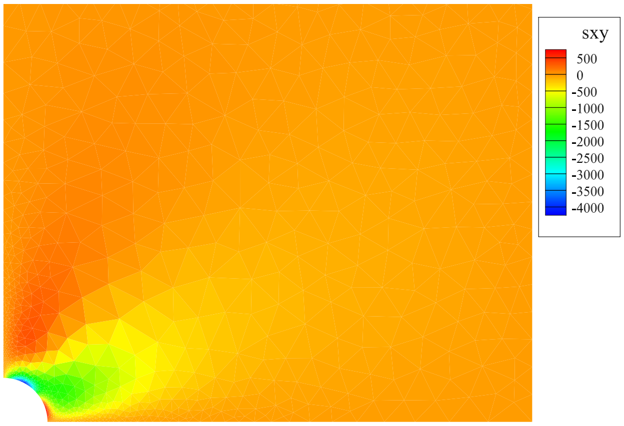

Figure 3.19 Shear stress contours of the third linear elasticity example

Stresses along three edges of the plate are depicted in figures(3.20) and (3.21). Note that in the case of a circular hole the Stress Concentration Factor (SCF) does not depend on the size of the hole and as is shown in figure(3.20-a), this factor is approximately three. Figure(3.20-b) reflects the normal stress where the force is applied to the plate. The numerical procedure captures this boundary condition with less than 0.1% error.

Figure(3.21) shows the normal stresses along x = 0. From the figure it is obvious that there is a singularity near the hole. This singularity comes from the fact that normal and shear stress inside the hole is zero, while there is a normal stress in the adjacent edge of element that makes the singularity. At a distance far enough from the hole the normal stress yields zero that satisfies the zero stress on this edge.

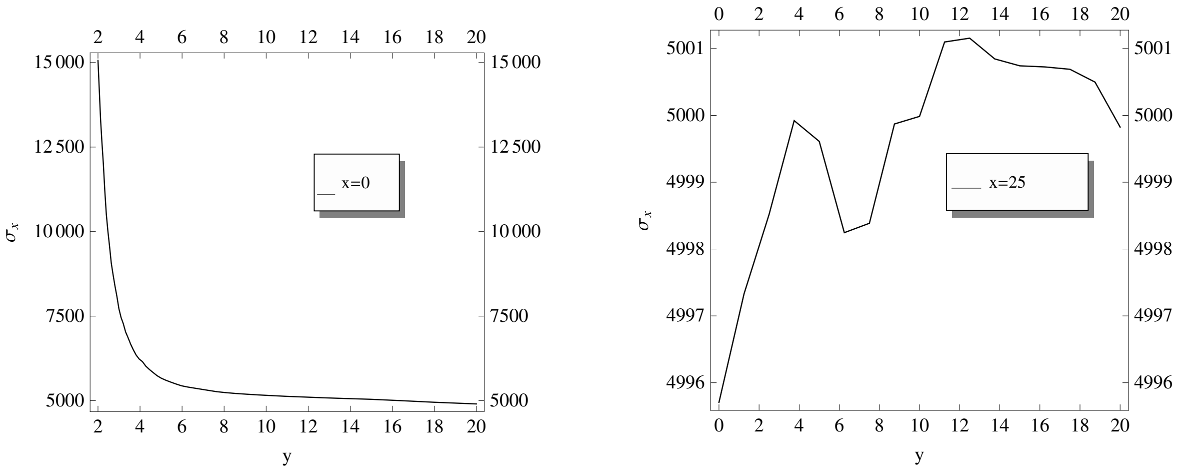

(a) Normal stress at the Dirichlet boundary condition
(b) Normal stress at the Neumann boundary condition

Figure 3.20 Normal stresses along the y direction

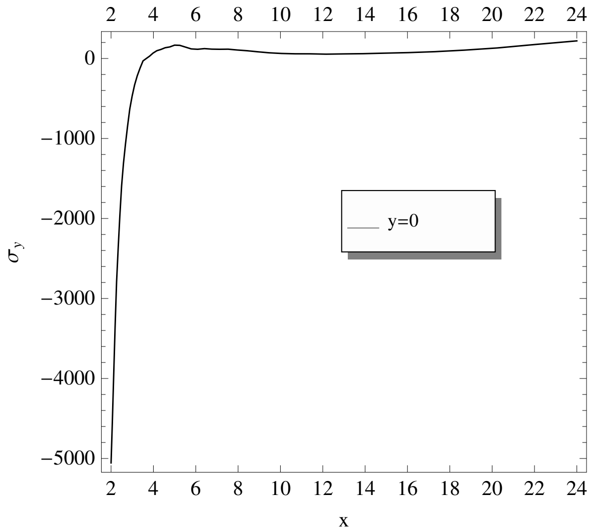

Figure 3.21 Transverse normal stress along the x direction

3.7 Conclusion

In this section the numerical implementation of discontinuous Galerkin interior penalty approaches for solution of Poisson and linear elasticity is presented. The equations are first written in a primal form and new fluxes on the interior and boundary edges are defined such that they can be incorporated into any class of interior penalty methods. Implementation details are discussed and examples are introduced to verify the results of the developed methodology.

CHAPTER 4

COMPARISON OF LINEAR AND NONLINEAR ELASTICITY FOR MESH DEFORMATION

4.1 Introduction

In arbitrary Lagrangian-Eulerian formulations [38, 39], a procedure to adapt the mesh after each solid body movement is required. Many approaches have been suggested for this task, such as tension spring analogy [40] or treating the mesh as a linear elastic material [41]. Other techniques based on adjoint methods [42] and equations of elasticity with selective treatment for mesh deformation [43] have also been proposed for improved treatment of large deformations in the mesh. With increasing popularity of higher-order finite element methods, finding a procedure to adjust the mesh to curvilinear boundaries has become an important issue. Thus, non-linear solid mechanics concepts in curved mesh generation and mesh refinement have been implemented in [44]. Similarly, to address the same issue, thermo-elastic concepts are used in [45] for boundary curvature. Over the last few years, several works have investigated curvilinear mesh generation techniques, but these methods have not been implemented for large deformation mesh movement.

The aforementioned schemes are computationally expensive and research that compare these schemes computationally are rarely found. In this section a procedure to cast the mesh deformation as a non-linear material response is developed in a continuous Galerkin finite element framework. The back-ground terminology and two classes of hyper elastic materials (Saint-Venant and Neo-Hookean) have been introduced in Chapter(2). Mesh deformation with these two material models are compared with linear elasticity, and the computational cost of each scheme is discussed.

4.2 Constitutive equations

Constitutive equations for the linear and non-linear isotropic materials have been discussed in Chapter(2), and here the implementation procedure and the numerical results are presented.

4.3 Mesh deformation implementation procedure

For mesh deformation using the elasticity analogy, the boundary deformation is imposed incrementally. The stress tensor of each element is calculated due to strain created by this boundary deformation. In linear elastic and Saint Venant-Kirchhoff materials, the elasticity tensor is independent of deformation, but in neo-hookean materials this tensor should be calculated accordingly. Internal mesh points adjust to new positions to eliminate the residual generated because of this internal energy. After reducing the residual order to a pre-specified level, another deformation increment will be applied and this procedure continues until the mesh adapts to its new configuration.

For large displacement and strains, two numerical formulations may be utilized based on the selected coordinates to be used for evaluation of the quantities. In the updated Lagrange formulation the reference coordinate is updated in each increment but in the total Lagrange the original un-deformed coordinate is used for the calculations [46]. The effect of this selection is investigated in section(4.5) of this chapter.

4.4 Numerical results

In this section the procedure of mesh movement with linear and non-linear elasticity is illustrated by four examples. A single layer thick beam is investigated initially to validate the non-linear algorithms for large strain range problems. Subsequently, combined mesh movement and adaption is studied for a square plate. In large deformations, mesh quality can not be conserves, thus, this combination increases the mesh quality after the mesh movement procedure. For the next example, 360° rotation of a circle is performed to demonstrate that the scheme is capable of large mesh deformation. Finally, comparison of linear and non-linear elasticity is investigated for 90° rotation of an airfoil. For all of these examples, an updated Lagrange formulation is implemented in a CG finite element platform.

4.4.1 Clamped-Free single layer laminate under body force

A cantilever steel plate, fixed at $x = 0$ and free at $x = L$ with different aspect ratios of ($L/H = 1$, 4, 10 and 20) described in [47] is investigated. The problem is solved under plane stress assumptions with Saint Venant and neo-Hookean material models. The material properties and body force (weight per volume of the material) assumed for this example are defined as

$$E = 29000\,psi,\;\; \nu = 0.3,\;\; \mathbf{b} = \left\{0, -2.836\times10^{-4}, 0\right\}\frac{kipf}{in^3} \tag{4.1}$$

Both of the material models show similar results so only results of the neo-Hookean model is provided here. End deflection of the plate for four aspect ratios of 1, 4, 10 and 20 is tabulated and compared with the deflection obtained from the classical solution of plates [48] and from reference [47] in table(4.1). Shamsaei and Boroomand [47] have used exponential basis functions in their simulations which is and their scheme can capture large strains in thick multi-layered anisotropic materials, but that method can only be applied for rectangle laminates. In contrast, the hyper-elastic formulation presented here is applicable to any geometries. As expected the difference between the results become less as the aspect ratio grows. However, for a square plate the deflection obtained from the present study is twice as much as that evaluated from classical laminate theory. The maximum of normal stress and transverse shear stresses at $0.1 \times L$ from the clamped support for four ratios of length to thickness are compared between the present analysis and reference [47] and shown in table(4.2).

Table 4.1 Comparison of maximum deflection of cantilever between classical laminate theory, reference [47] and the present study in different aspect ratios

L/H	1	4	10	20
Reference [47]	-4.159×10^{-6}	-0.0005725	-0.0212954	-0.33848
Present analysis	-4.249×10^{-6}	-0.0005721	-0.0212732	-0.337065
CLT	-2.112×10^{-6}	-0.0005408	-0.0211233	-0.33797

Results of table(4.2) show good agreements between the present analysis and reference [47]. The distribution of the shear and transverse normal stresses in the thickness of the described square plate ($L = H = 12$) is shown in figure(4.1) and normal and transverse deflections are depicted in figure(4.2).

Table 4.2 Comparison of maximum stresses at a distance $0.1 \times L$ from the clamped support between reference [47] and the present study in different aspect ratios

L	H	$\lvert\sigma_x\rvert$		$\lvert\tau_{xy}\rvert$	
		Reference [47]	Present analysis	Reference [47]	Present analysis
12	12	0.009423	0.009468	0.00352536	0.00350497
48	12	0.130371	0.1290987	0.0182922	0.0183648
120	12	0.826261	0.814429	0.0460553	0.044663149
240	12	3.30727	3.275483	0.091887	0.0935204

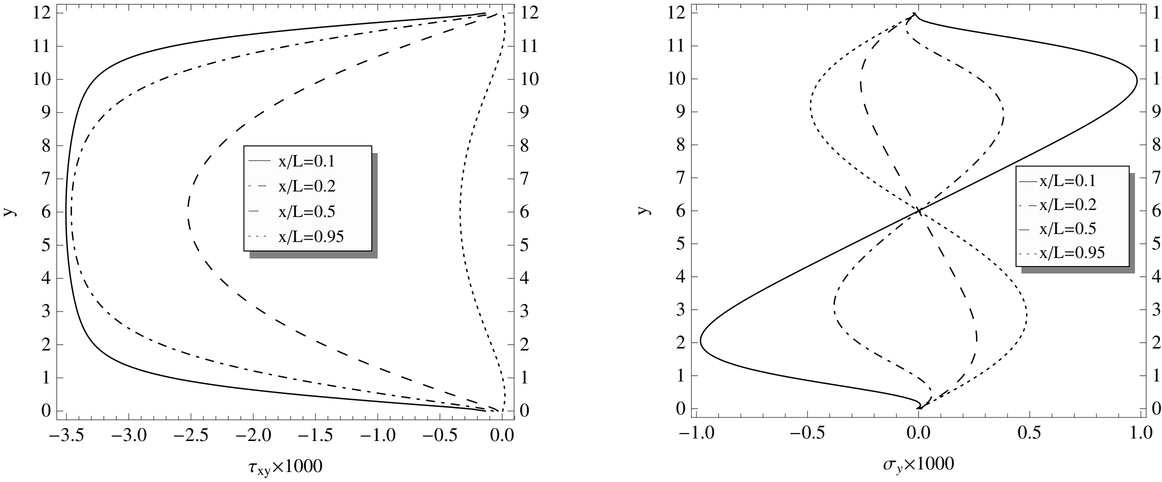

(a) Distribution of shear stress (τ_{xy}) in the height of the plate

(b) Distribution of transverse normal stress (σ_y) in the height of the plate

Figure 4.1 The distribution of axial and transverse normal stress in different sections of a square plate carrying body weight

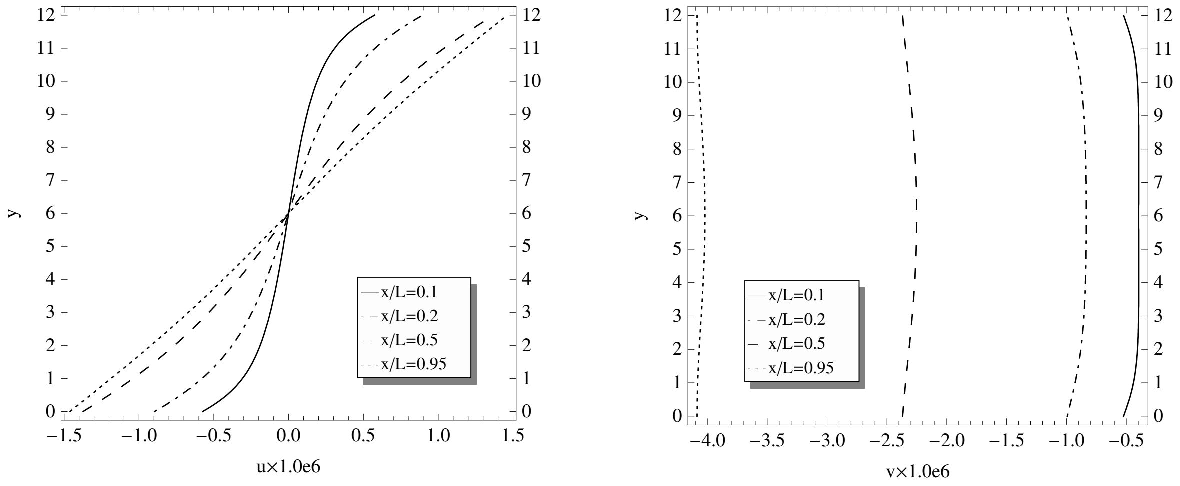

(a) Distribution of axial displacement

(b) Distribution of transverse displacement

Figure 4.2 The displacements in different sections of a square plate carrying body weight

4.4.2 Mesh deformation with adaptation

In this example a 10×10 square plate with a combined boundary movement and mesh adaptation is depicted in different stages of the mesh movement. The mesh is refined with a h-adaptation algorithm in three steps and is subjected to adapt the new boundary condition of $0.15 \times x \times (x-10)$. In large deformations, mesh quality changes that affect the final simulation results. One remedy for this effect is to refine the mesh in skewed elements. In this example this combination is shown that increases the mesh quality after the mesh movement procedure. Figure(4.3) shows the different stages of the mesh movement.

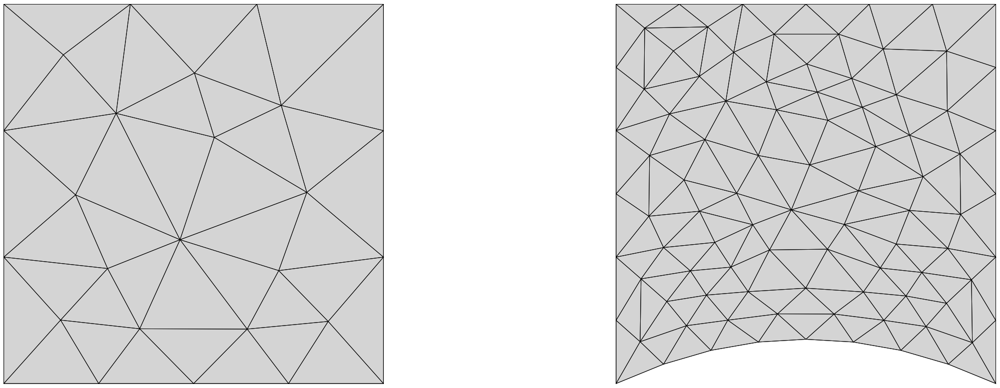

(a) Initial configuration

(b) 1/3 of final boundary position

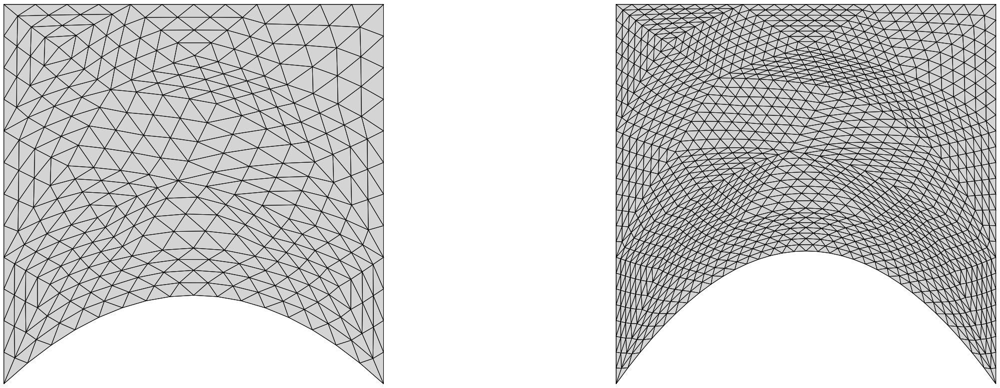

(c) 2/3 of final boundary position

(d) Final stage

Figure 4.3 Adaptation of the square plate

4.4.3 Cylinder rotation

For this example a cylinder with a triangular appendage is rotated 360°. A Saint Venant Kirchhoff hyper-elastic material is used for this procedure. Modulus of elasticity is linearly reduced with the distance from the interior cylinder. 200 incremental steps are regarded for this rotation. This example is provided to show the capability of the non-linear formulation for large mesh deformation and comparison of the linear and non-linear elasticity for this procedure is provided in the next example. As can be seen in figure(4.4), the current scheme is capable of deforming and producing a mesh of acceptable quality when subjected to large deformation.

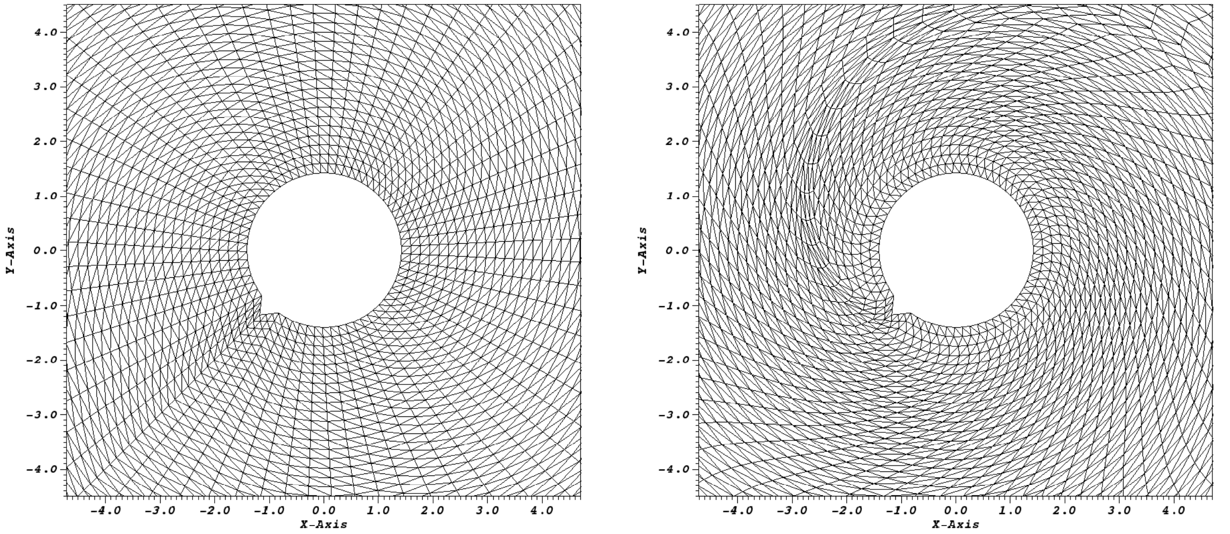

(a) Initial condition of cylinder

(b) Cylinder after 360 degrees rotation of inner boundary

Figure 4.4 Cylindrical mesh under large deformation

4.4.4 Rotation of a NACA-6412 airfoil

For the final example, three different material models are deployed for the mesh deformation of NACA-6412 airfoil. A stiffer layer around the airfoil is embedded to preserve the viscous layer. The modulus of elasticity in this layer $E1$ is considered as 100 times more than $E2$ which is the stiffest part in the outer layer. Modulus of elasticity is linearly reduced with the distance from the airfoil in the softer or outer layer. Figure(4.5) is provided to show the selection of modulus of elasticity for this example.

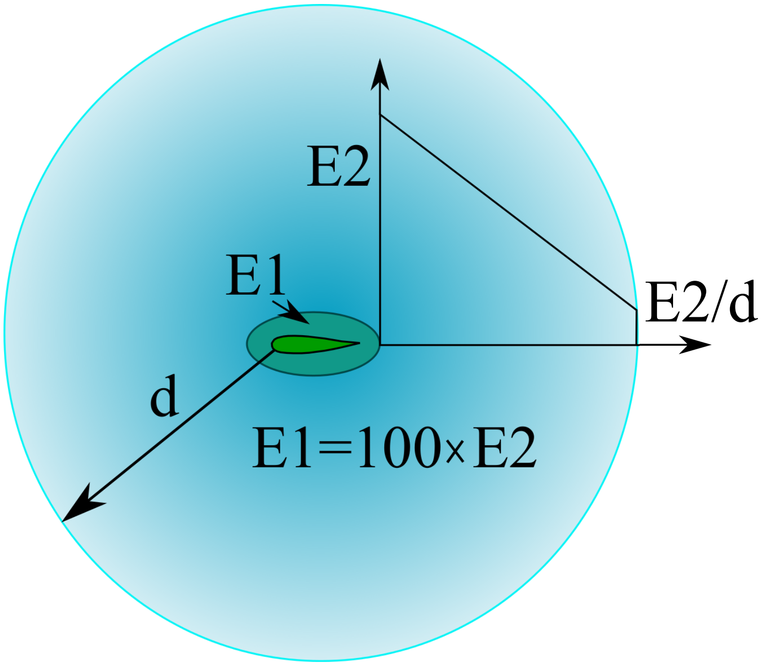

Figure 4.5 Illustration of modulus of elasticity for the mesh movement

Mesh deformation is investigated using linear elastic, Saint Venant-Kirchhoff and neo-hookean material models. The neo-Hookean results are provided for the non-linear models in the following figures because of the similarity between the final results of the Saint-Venant and neo-Hookean schemes. Figure(4.6) shows the difference between using non-linear hyper-elastic and linear elastic material models for 200 increments of rotation. Elemental weighted condition number, skewness and aspect ratio are calculated for each triangle as mesh metrics. Distribution of elemental weighted condition number and skewness of initial mesh is depicted in figure(4.7). Comparison of elemental aspect ratio, skewness and weighted condition number between linear elastic and hyper-elastic mesh movement with 200 increments of rotation are depicted in figures(4.8), (4.9) and (4.10), respectively. The difference between the scaling in these figures should be noted for better understanding of the differences. Comparison of change in the elemental metrics from the initial configuration such as aspect ratio, skewness and weighted condition number between linear elastic and hyper-elastic mesh movement with 200 increments of rotation are also provided in figures(4.11), (4.12) and (4.13), respectively.

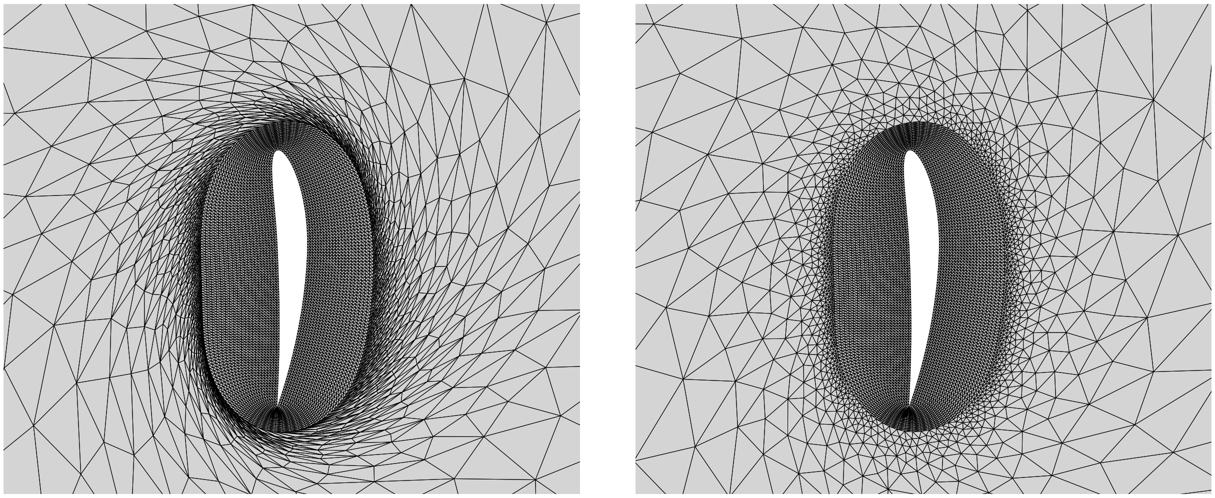
(a) Linear elastic material

(b) neo-Hookean material

Figure 4.6 NACA-6412 after 90° rotation

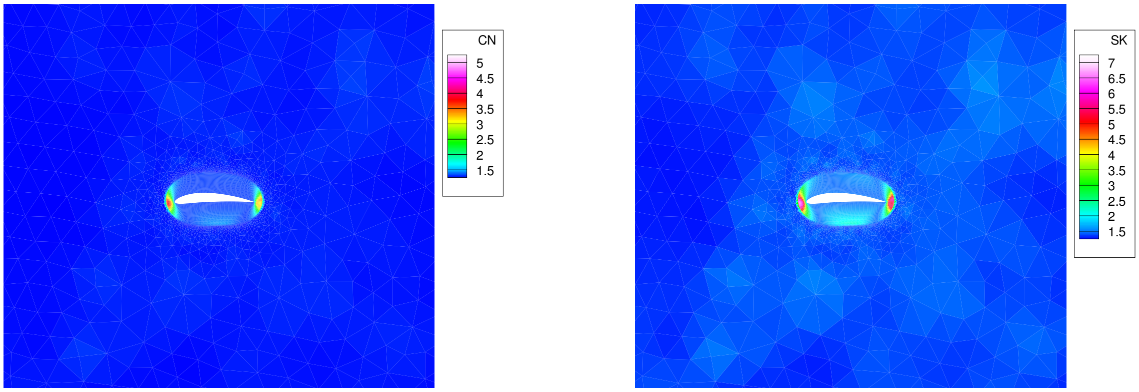

(a) Distribution of condition number of mesh elements in the initial mesh

(b) Distribution of skewness of mesh elements in the initial mesh

Figure 4.7 Initial NACA-6412 mesh metrics

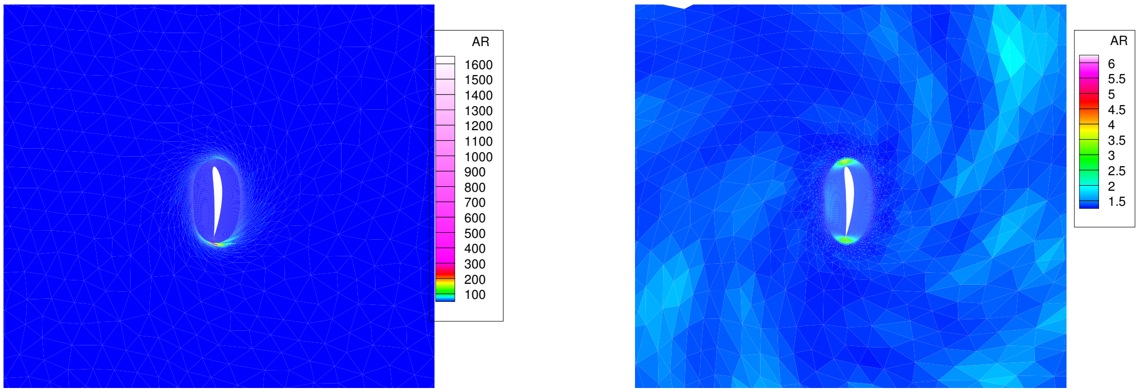

(a) Linear elasticity model

(b) Non-linear neo-Hookean model

Figure 4.8 Distribution of aspect ratio of mesh elements in NACA-6412 after 90° rotation with 200 incremental rotation

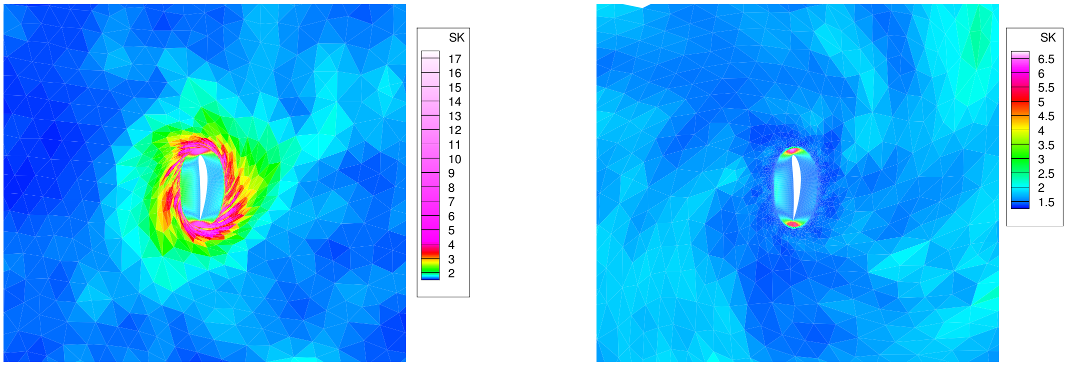

(a) Linear elasticity model

(b) Non-linear neo-Hookean model

Figure 4.9 Distribution of skewness of mesh elements in NACA-6412 after 90° rotation with 200 incremental rotation

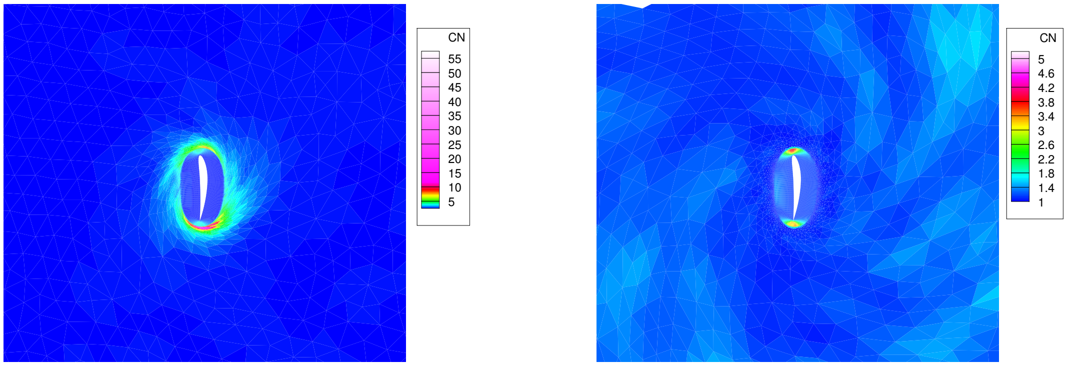

(a) Distribution of weighted condition number of mesh elements in linear elasticity model

(b) Distribution of weighted condition number of mesh elements in non-linear neo-Hookean model

Figure 4.10 Distribution of weighted condition number of mesh elements in NACA-6412 after 90° rotation with 200 incremental rotation

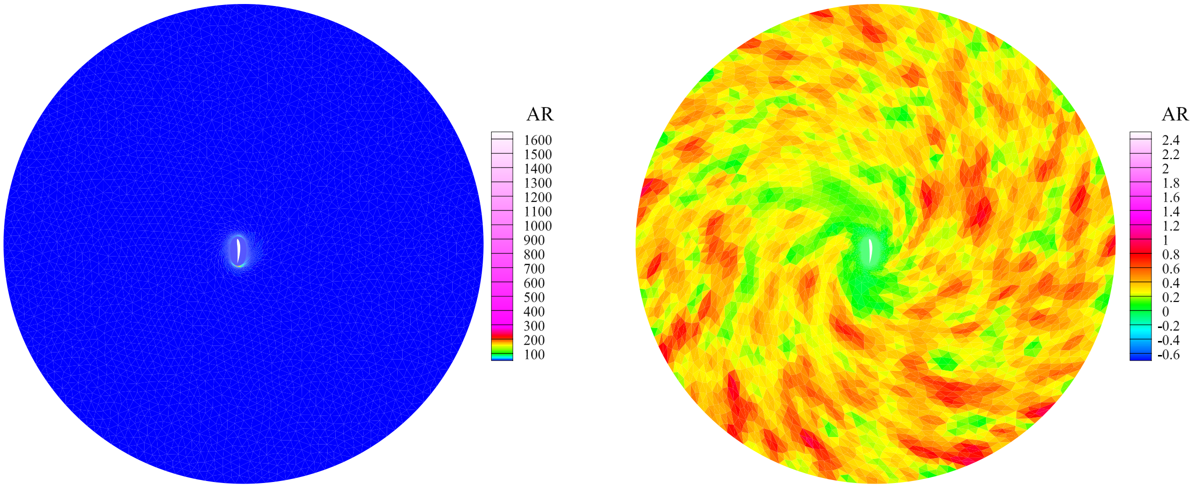

(a) Linear elasticity model (b) Non-linear neo-Hookean model

Figure 4.11 Distribution of change of aspect ratio of mesh elements in NACA-6412 after 90° rotation with 200 incremental rotation

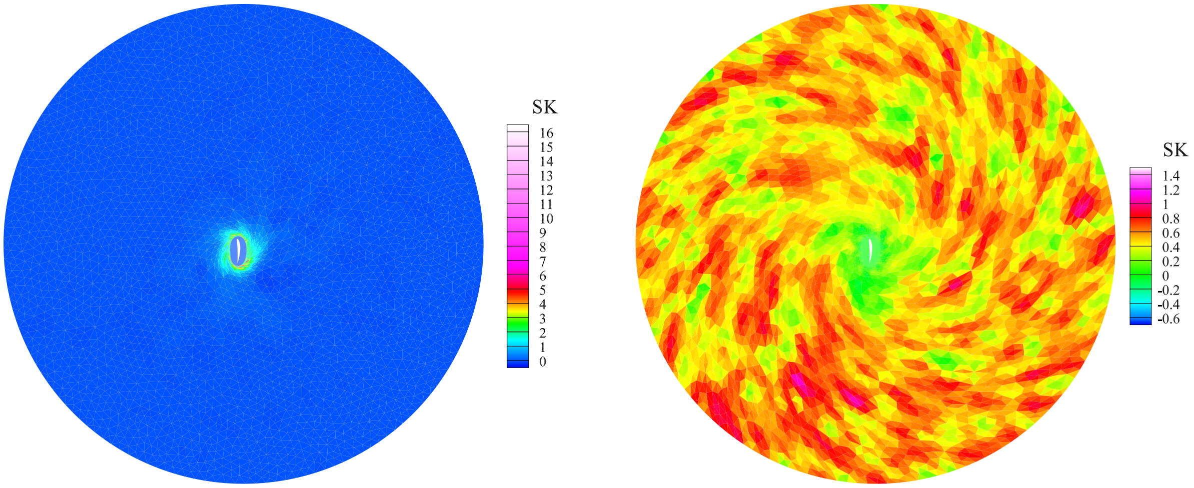

(a) Linear elasticity model (b) Non-linear neo-Hookean model

Figure 4.12 Distribution of change of skewness of mesh elements in NACA-6412 after 90° rotation with 200 incremental rotation

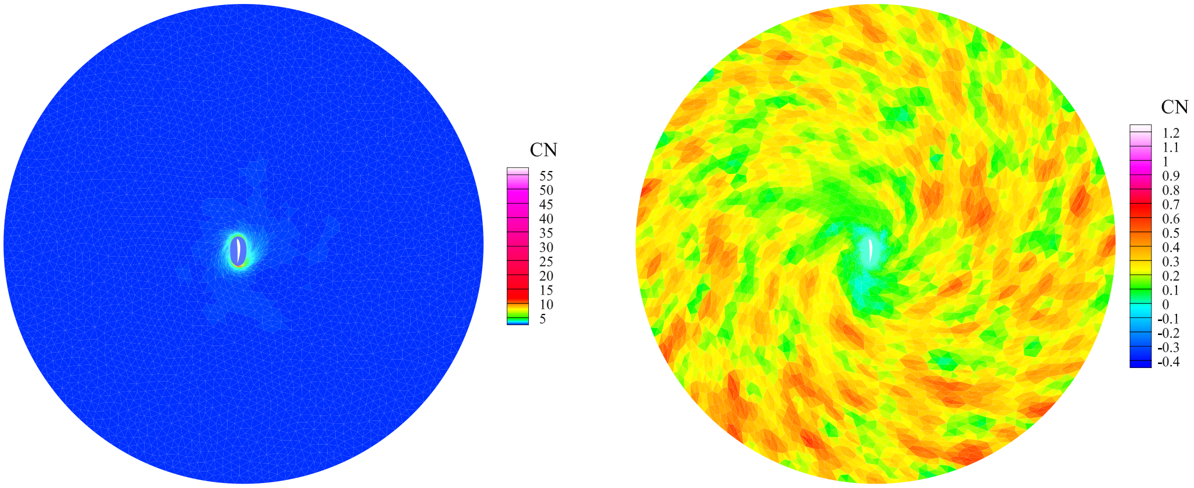

(a) Linear elasticity model

(b) Non-linear neo-Hookean model

Figure 4.13 Distribution of change of weighted condition number of mesh elements in NACA-6412 after 90° rotation with 200 incremental rotation

Table(4.3) provides more detail for comparing the linear and non-linear models. This table compares the mesh metrics and computational cost of each algorithm. Table(4.4) represents the changes in the mesh metrics in the described methods. From these two tables, the superiority of using linear elasticity with more incremental steps over the non-linear elasticity models is evident.

Table 4.3 Comparison of mesh metrics and CPU time between different mesh movement algorithms

Deformation method	Aspect Ratio		Skewness		Weight. Cond. Num.		CPU Time(s)
	Max	*Min*	*Max*	*Min*	*Max*	*Min*	
Initial mesh	6.59	1.00	7.09	1.00	5.17	1.00	
Linear Elastic 200 Iteration	1717.76	1.00	18.10	1.00	59.97	1.00	3178
Neo-Hookean 200 Iteration	6.59	1.00	7.09	1.00	5.17	1.00	13289
Saint Venant 200 Iteration	6.59	1.00	7.09	1.00	5.17	1.00	15467
Linear Elastic 500 Iteration	6.59	1.00	7.09	1.00	5.17	1.00	8011

Table 4.4 Comparison of maximum and minimum mesh metric change between different mesh movement algorithms

Deformation method	Aspect Ratio		Skewness		Weight. Cond. Num.	
	Max	*Min*	*Max*	*Min*	*Max*	*Min*
Linear Elastic 200 Iteration	1716.76	-1.24	16.52	-0.67	58.97	-0.65
Neo-Hookean 200 Iteration	2.55	-0.77	1.63	-0.80	1.23	-0.42
Saint Venant 200 Iteration	2.55	-0.77	1.63	-0.80	1.23	-0.42
Linear Elastic 500 Iteration	2.93	-0.79	1.70	-0.80	1.27	-0.43

4.5 Discussion

Although, it is not the primary focus of this dissertation, the purpose of the present chapter was to investigate and compare linear and non-linear elasticity for mesh deformation. Based on this limited study, some observations can be made.

1. For small deformations, or using small increments during mesh deformation, the final result of linear and non-linear is the same. This outcome is expected because of the linear behavior of non-linear equations in small deformations.

2. The updated Lagrange formulation that updates the mesh coordinates in each incremental step was found to be more robust than the total Lagrange scheme, Although the two methods can be shown to be mathematically equivalent [46], for extremely large deformations the total Lagrange formulation would not converge in the mesh movement process.

3. Inherently, the neo-Hookean formulation is more expensive than the Saint Venant hyperelasticity, however, the Saint Venant-kirchhoff model requires more non-linear or Newton-Raphson iterations to reduce the order of residual to the same tolerance. This increase in iterations at each displacement increment, ultimately makes the Saint Venant model more computationally demanding.

4. Although not shown, numerical experiments indicated that the neo-Hookean model allows larger deformation increments to be taken within the mesh movement process. This aspect could be further investigated for computational savings.

4.6 Conclusion

In this chapter, constitutive equations for three different types of materials are preliminarily studied for mesh deformation, typically needed in fluid dynamic applications. Subsequently, the mesh is treated as a linear and non-linear material and subjected to prescribed boundary motion. The computational cost and mesh quality after large deformations are then compared. In this limited study, with increased number of deformation increments, it appears that the use of linear elasticity remains the more efficient approach for mesh movement. That is, although larger deformation increments may be taken using the non-linear materials models, the computational cost associated with the solution procedure is considerably higher.

CHAPTER 5

CONSTITUTIVE EQUATIONS FOR TRANSVERSELY ISOTROPIC LARGE STRAIN MATERIALS

In this chapter a set of constitutive equations for simulation of large strain transversely isotropic materials are described. Validation of this material model is performed using examples of composite beams undergoing large strains. Subsequently, the loading, geometry and material properties for the simulation of the femur are described and the aforementioned constitutive equations are implemented to simulate the non-linear behavior of the bone.

5.1 Introduction

Because of the existence of fibers in biological soft and hard tissues, these materials exhibit transversely isotropic behavior. This behavior is characterized by having different responses in the fiber and perpendicular to the fiber directions. Biological soft tissues like muscle and flesh undergo non-linear large deformations that yields large strains. With aging, the bone density diminishes and the solid outer layer becomes thinner. This means that hard bones turn spongy, and spongy bones turn spongier [49]. More than 220,000 proximal femoral fractures occur in the United States each year, where 90 % of these fractures occur in patients older than 50 years [50]. Furthermore, in [51] the relation of sponginess of the bone with the fracture is established. This relationship illustrates the necessity of using non-linear elasticity equations for the simulation of proximal femur failure.

Femur is the longest body bone and is a compound of two layers of cortical (or hard outer layer) and cancellous (or inner or spongy) bone. The upper or proximal extremity part of femur consists of a head, neck and the two trochanters. This bone has been found to exhibit transversely isotropic behavior in different parts [52].

In the next section, the constitutive equations of non-linear materials for transversely isotropic materials based on the proposed scheme from Bonet and Burton [3] is discussed. These equations are implemented in the simulation of large strain composite materials for verification. Material and morphological properties of the proximal femur is described and maximum strains of the bone are compared using linear and non-linear analysis.

5.2 Constitutive equations for transversely isotropic linear and non-linear materials

In this section the general orthotropic materials and a sub-class of them, i.e. transversely isotropic materials, are introduced. Furthermore, the constitutive equations of linear and non-linear behavior for transversely isotropic materials are presented.

5.2.1 General orthotropic materials

In linear materials, the relation between stress and strain follows equation(2.16). As discussed, both the stress and strain in the equation are linear and the only difference between the isotropic and transversely isotropic materials is embodied within the stiffness matrix K. This relation between the strain and stress is given as

$$\begin{Bmatrix} \varepsilon_{11} \\ \varepsilon_{22} \\ \varepsilon_{33} \\ 2\varepsilon_{12} \\ 2\varepsilon_{13} \\ 2\varepsilon_{23} \end{Bmatrix} = \begin{bmatrix} \frac{1}{E_1} & \frac{-\nu_{21}}{E_2} & \frac{-\nu_{31}}{E_3} & 0 & 0 & 0 \\ \frac{-\nu_{12}}{E_1} & \frac{1}{E_2} & \frac{-\nu_{32}}{E_3} & 0 & 0 & 0 \\ \frac{-\nu_{13}}{E_1} & \frac{-\nu_{23}}{E_2} & \frac{1}{E_3} & 0 & 0 & 0 \\ 0 & 0 & 0 & \frac{1}{G_{12}} & 0 & 0 \\ 0 & 0 & 0 & 0 & \frac{1}{G_{13}} & 0 \\ 0 & 0 & 0 & 0 & 0 & \frac{1}{G_{23}} \end{bmatrix} \begin{Bmatrix} \sigma_{11} \\ \sigma_{22} \\ \sigma_{33} \\ \sigma_{12} \\ \sigma_{13} \\ \sigma_{23} \end{Bmatrix} \tag{5.1}$$

In the above relation, E_i, ν_{ij} and G_{ij} are the Young's modulus, Poisson ratio and shear modulus in the corresponding i and j directions. The matrix relating the strains to the stresses is referred to as the compliance matrix. The matrix relating strain to stress is referred to as the compliance matrix. The constitutive or the stiffness matrix of the general orthotropic material is symmetric and can be obtained by inverting the compliance matrix.

5.2.2 Transversely isotropic linear materials

A class of orthotropic materials is called transversely isotropic, and exhibit similar properties in the two directions perpendicular to the principal direction. Assuming the materials are aligned in direction 3, the material properties of this type are

$$\begin{aligned} &E_1 = E_2 = E, \quad E_3 = E_A, \quad \nu_{12} = \nu_{23} = \nu_{13} = \nu \\ &G_{13} = G_{23} = G, \quad G_{12} = \frac{E}{2(1+\nu)} \end{aligned} \tag{5.2}$$

Implementing these relations in the stiffness or elasticity matrix for transversely isotropic materials yields

$$\begin{Bmatrix} \sigma_{11} \\ \sigma_{22} \\ \sigma_{33} \\ \sigma_{12} \\ \sigma_{13} \\ \sigma_{23} \end{Bmatrix} = \begin{bmatrix} \frac{E(1-nv^2)}{m(1+v)} & \frac{E(v+nv^2)}{m(1+v)} & \frac{E_A v}{m} & 0 & 0 & 0 \\ \frac{E(v+nv^2)}{m(1+v)} & \frac{E(1-nv^2)}{m(1+v)} & \frac{E_A v}{m} & 0 & 0 & 0 \\ \frac{E_A v}{m} & \frac{E_A v}{m} & \frac{E_A(1-v)}{m} & 0 & 0 & 0 \\ 0 & 0 & 0 & \frac{E}{2(1+v)} & 0 & 0 \\ 0 & 0 & 0 & 0 & G & 0 \\ 0 & 0 & 0 & 0 & 0 & G \end{bmatrix} \begin{Bmatrix} \varepsilon_{11} \\ \varepsilon_{22} \\ \varepsilon_{33} \\ 2\varepsilon_{12} \\ 2\varepsilon_{13} \\ 2\varepsilon_{23} \end{Bmatrix} \tag{5.3}$$

where in the above relation $n = E/E_A, \quad m = 1 - v - 2nv^2$.

5.2.3 Transversely isotropic materials under large strains

Composite materials are typically regarded as transversely isotropic and when they experience large strains, for example in short and thick beams, the linear equations tend to under estimate the deflections in the simulation. Thus, in the next section, the constitutive equations based on a proposed method in [3] are considered. Constitutive equations for the non-linear neo-Hookean and Saint Venant-Kirchhoff isotropic materials have been discussed in sections(2.2.2) and (2.2.3).

Considering A to be the material fiber direction in the un-deformed configuration, and thus a = F.A to be the new material direction after deforming in the deformed configuration. The material is isotropic in the two directions perpendicular to the principal direction A, which suggests that the deformation energy density function is a function of three invariants of tensor C and two additional invariants I_4 and I_5. Therefore with $\bar{w} = \Im(I_1, I_2, I_3, I_4, I_5)$ [53], these two invariants are

$$I_4 = A.\mathrm{C}.A, \quad I_5 = A.\mathrm{C}^2.A \tag{5.4}$$

The derivatives of these invariants with respect to tensor C are

$$\frac{\partial I_4}{\partial \mathrm{C}} = A \otimes A, \quad \frac{\partial I_5}{\partial \mathrm{C}} = \mathrm{C}A \otimes A + A \otimes \mathrm{C}A \tag{5.5}$$

Thus, similar to equation(2.10), the second Piola-Kirchhoff stress tensor may be expressed as

$$\mathrm{S} = \frac{2\partial \bar{w}}{\partial \mathrm{C}} = 2\frac{\partial \bar{w}}{\partial I_1}\mathrm{I} + 4\mathrm{C}\frac{\partial \bar{w}}{\partial I_2} + 2I_3\mathrm{C}^{-1}\frac{\partial \bar{w}}{\partial I_3} + 2(A \otimes A)\frac{\partial \bar{w}}{\partial I_4} + 2(\mathrm{C}A \otimes A + A \otimes \mathrm{C}A)\frac{\partial \bar{w}}{\partial I_5} \tag{5.6}$$

Similar to the discussed concerning isotropic materials, i.e. Saint Venant-Kirchhoff and neo-Hookean constitutive equations, that for transversely isotropic materials is presented in the following section.

5.2.3.1 Transversely isotropic Saint Venant-Kirchhoff materials

As discussed, deformation density function of transversely isotropic materials is also a function of two additional invariants, namely I_4 and I_5. In these constitutive equations, the deformation density function is a function of isotropic and transverse components expressed as

$$\bar{w} = \bar{w}_{iso} + \bar{w}_{trans} \tag{5.7}$$

As a result, both stress and the elasticity tensors have two components, i.e. isotropic and transverse, and may be written as

$$\begin{aligned} \sigma &= \sigma_{iso} + \sigma_{trans} \\ \mathrm{K}_{\text{Eulerian}} &= \mathrm{K}_{iso} + \mathrm{K}_{trans} \end{aligned} \tag{5.8}$$

In transversely isotropic Saint Venant-Kirchhoff materials the isotropic deformation density function and stress tensor are defined similar to isotropic materials in equations(2.27) and (2.28), thus the elasticity tensor shall be defined as

$$\mathrm{K}_{iso} = \lambda \mathrm{I} \otimes \mathrm{I} + 2\mu \delta_{ik} \delta_{jl} \tag{5.9}$$

Transverse counterparts are defined as

$$\begin{aligned} &\bar{w}_{trans} = \left(\alpha + \beta\left(I_1 - 3\right) + \mathcal{X}\left(I_4 - 1\right)\right)\left(I_4 - 1\right) - \tfrac{1}{2}\alpha\left(I_5 - 1\right) \\ &\mathrm{S}_{trans} = \tfrac{2\partial \bar{w}_{trans}}{\partial \mathrm{C}} = 2\beta\left(I_4 - 1\right)\mathrm{I} + 2\left(\alpha + \beta\left(I_1 - 3\right) + 2\mathcal{X}\left(I_4 - 1\right)\right) A \otimes A \\ &-\alpha\left(\mathrm{C}A \otimes A + A \otimes \mathrm{C}A\right) \\ &\mathrm{K}_{trans} = \tfrac{2\mathrm{S}_{trans}}{\partial \mathrm{C}} = 8\mathcal{X} A \otimes A \otimes A \otimes A + 4\beta\left(A \otimes A \otimes \mathrm{I} + \mathrm{I} \otimes A \otimes A\right) - 2\alpha \Upsilon \\ &\Upsilon_{ijkl} = A_i A_l \delta_{jk} + A_j A_l \delta_{ik} \\ &n = \tfrac{E}{E_A},\ m = 1 - \nu - 2n\nu^2,\ \vartheta = \tfrac{E(\nu + n\nu^2)}{m(1+\nu)} \\ &\alpha = \mu - G_A,\ \beta = \tfrac{E\nu^2(1-n)}{4m(1+\nu)},\ \mathcal{X} = \tfrac{E_A(1-\nu)}{8m} - \tfrac{\vartheta + 2\mu}{8} + \tfrac{\alpha - 2\beta}{2} \end{aligned} \tag{5.10}$$

The summation of the isotropic and transverse components of the elasticity tensor in the defined equations is nothing more than the transformation of the elasticity tensor to the direction of the material. Thus, the relation between the stress and strain is linear and the same set of equations as equation(2.29) applies here for the stress tensor, namely

$$\begin{aligned} \mathrm{S} &= \mathrm{K} : \gamma \\ \sigma &= \mathrm{K} : \eta \end{aligned} \tag{5.11}$$

5.2.3.2 *Transversely isotropic neo-Hookean materials*

Here, two sets of constitutive equations are described for transversely isotropic solids, and are based on the neo-hookean material model. Similar to isotropic materials, Saint Venant-Kirchhoff models are ideal for small to moderate strain ranges, despite the fact that linear elasticity is only applicable for small strain regimes. In large strains, the neo-hookean definitions have more validity. The equations for the isotropic components defined in equations(2.24) and (2.26) can be used here. Defining the transverse stress and elasticity tensors in the following form gives a simple neo-hookean set of equations

$$\begin{aligned} \sigma_{trans} &= J^{-1} \begin{pmatrix} 2\beta\left(I_4 - 1\right)\mathrm{B} + 2\left(\alpha + \beta\left(I_1 - 3\right) + 2\mathcal{X}\left(I_4 - 1\right)\right) a \otimes a \\ -\alpha\left(\mathrm{B}a \otimes a + a \otimes \mathrm{B}a\right) \end{pmatrix} \\ \mathrm{K}_{trans} &= J^{-1}\left(8\mathcal{X} a \otimes a \otimes a \otimes a + 4\beta\left(a \otimes a \otimes \mathrm{B} + \mathrm{B} \otimes a \otimes a\right) - 2\alpha\Upsilon\right) \\ \Upsilon_{ijkl} &= a_i a_l \mathrm{B}_{jk} + a_j a_l \mathrm{B}_{ik} \end{aligned} \tag{5.12}$$

One should notice that equation(5.12) is nothing more than reinterpretation of equation(5.10) in the deformed configuration, which is basically the linear anisotropic part. Adding this linear transverse part to the non-linear isotropic hyper-elastic formulation constitutes this model. Thus, the transverse part of the stress and elasticity tensor might not behave fully non-linear in large strain regimes. To this end, the following set of equations will be defined to better represent the non-linearity

$$
\begin{aligned}
\bar{w}_{trans} &= \left(\alpha + \beta \ln J + \mathcal{X}\left(I_4 - 1\right)\right)\left(I_4 - 1\right) - \tfrac{1}{2}\alpha\left(I_5 - 1\right) \\
\sigma_{trans} &= J^{-1}\left(\begin{array}{l} 2\beta\left(I_4 - 1\right)\mathrm{I} + 2\left(\alpha + 2\beta \ln J + 2\mathcal{X}\left(I_4 - 1\right)\right) a \otimes a \\ -\alpha\left(\mathrm{B}a \otimes a + a \otimes \mathrm{B}a\right) \end{array}\right) \\
\mathrm{K}_{trans} &= J^{-1}\left(8\mathcal{X} a \otimes a \otimes a \otimes a + 4\beta\left(a \otimes a \otimes \mathrm{I} + \mathrm{I} \otimes a \otimes a\right) - \alpha\Upsilon - 4\beta\left(I_4 - 1\right)\wp\right) \\
\Upsilon_{ijkl} &= a_i a_l \mathrm{B}_{jk} + a_j a_l \mathrm{B}_{ik} \\
\wp_{ijkl} &= \delta_{ik}\delta_{jl}
\end{aligned}
\tag{5.13}
$$

Appendix(A) illustrates how to transform the tensor notation to matrix notation for the elasticity tensor. Additionally, to provide an example for calculating the stress tensors in a tensor notation, expansion and the implementation procedure of tensors in equation(5.13) is presented in appendix(B).

5.3 Implementation of the non-linear equations for multi-layer materials

Examples for the validation of the described schemes are presented in the CG finite element platform. Different boundary conditions, material orientation, and loading are utilized to show the ability of the constitutive equations in simulating multi-layered materials. To this end, two examples are provided. One example for single layer lamina, and one two-layered laminae with various boundary conditions are provided for the verification process. In all examples, all Dirichlet boundaries are divided to 50 segments in the height of the plate. Accordingly, the number of points in the length are selected to create an equilateral triangular meshes. For these examples, a graphite-epoxy plate with the following properties is assumed

$$\begin{aligned} &E_A/E = 25,\ G/E = 0.5,\ \nu = 0.25 \\ &E_A = 172.25\,GPa\,(25 \times 10^6\,psi),\ E = 6.89\,GPa\,(10^6\,psi),\ G = 3.45\,GPa(0.5 \times 10^6\,psi) \end{aligned} \tag{5.14}$$

The material fiber is directed in the length of the plate (0 degree) for the single layer examples, as for the double-layer plate it is (0/90 degrees) for the laminae. The material orientation for these examples is shown in figur(5.1).

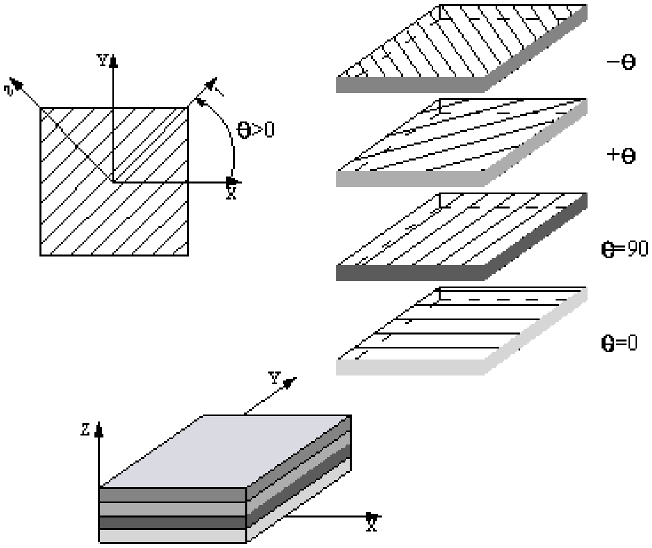

Figure 5.1 Material orientation for laminated structures

5.3.1 Clamped-Clamped single layer laminate

In this example a graphite-epoxy plate with clamped-clamped edges under a sinusoidal loading on the top surface is considered. The following traction vector is defined for the top surface

$$t_{X_1} = 0, \;\; t_{X_3} = -q_0 Sin(\frac{\pi X_1}{L}) \tag{5.15}$$

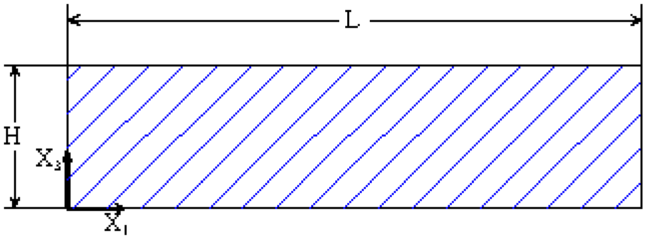

Figure 5.2 Geometry of the described laminate

The results of the current method are quantitatively compared with of [54] and classical laminate theory in tables (5.1 and 5.2), where normalized transverse deflection, normal stress, transverse shear stress, transverse normal stress and extension of normal (change of the thickness) are given at various locations in the plate. Results in [54] are obtained using an analytical solution of the cylindrical bending of a clamped-clamped, anisotropic plate of arbitrary span to thickness ratio. Here again *L* and *H* denote the length and height of the plate respectively. As it can be seen, the results are in excellent agreement with those presented in [54].

Table 5.1 Comparison between the normalized transverse deflections, normal stresses, transverse shear stresses obtained from the proposed method, classical laminated theory (CLT) and Vel and Batra [54] for four aspect ratios

L/H	$\frac{100EH^3}{q_0L^4}u_3\left(\frac{L}{2},\frac{H}{2}\right)$		$\frac{H^2}{q_0L^2}\sigma_{11}\left(\frac{L}{2},H\right)$		$\frac{H}{q_0L}\sigma_{31}\left(\frac{L}{4},\frac{H}{2}\right)$	
	[54]	*Present*	[54]	*Present*	[54]	*Present*
4	-1.4946	-1.4941	-0.4887	-0.4887	-0.2765	-0.2764
10	-0.3402	-0.3401	-0.2716	-0.2694	-0.3246	-0.3245
20	-0.1652	-0.1652	-0.2338	-0.2349	-0.3356	-0.3356
60	-0.1122	-0.1118	-0.2223	-0.2206	-0.3374	-0.3372
CLT	-0.1055		-0.2209		-0.3376	

Table 5.2 Comparison between the transverse normal stresses and extension of normal (change of the thickness) obtained from the proposed method, classical laminated theory (CLT) and Vel and Batra [54] for four aspect ratios

L/H	$\frac{1}{q_0}\sigma_{33}\left(\frac{L}{2},\frac{H}{2}\right)$		$\frac{10E}{q_0H}\left[u_3\left(\frac{L}{2},H\right)-u_3\left(\frac{L}{2},0\right)\right]$	
	[54]	*Present*	[54]	*Present*
4	-0.490	-0.499	-4.6238	-4.6246
10	-0.500	-0.499	-4.6731	-4.6730
20	-0.500	-0.500	-4.6750	-4.6750
60	-0.500	-0.500	-4.6750	-4.6750
CLT	-0.500			-

Figure(5.3) shows the distribution of normalized axial and shear stresses at different sections of the thick transversely isotropic plate. Excellent agreement of the results with those provided in [54] shows the applicability of the described equations for simulation of thick plates.

Since the loading is applied on the top surface of the plate, the plate exhibits asymmetry in the shear stress along the thickness. The absolute value of the shear stress reaches its maximum in the upper half of the plate. The shear stress at the boundaries increases sharply from zero at the edges. Theoretically, the upper and lower surfaces are free of shear stress.

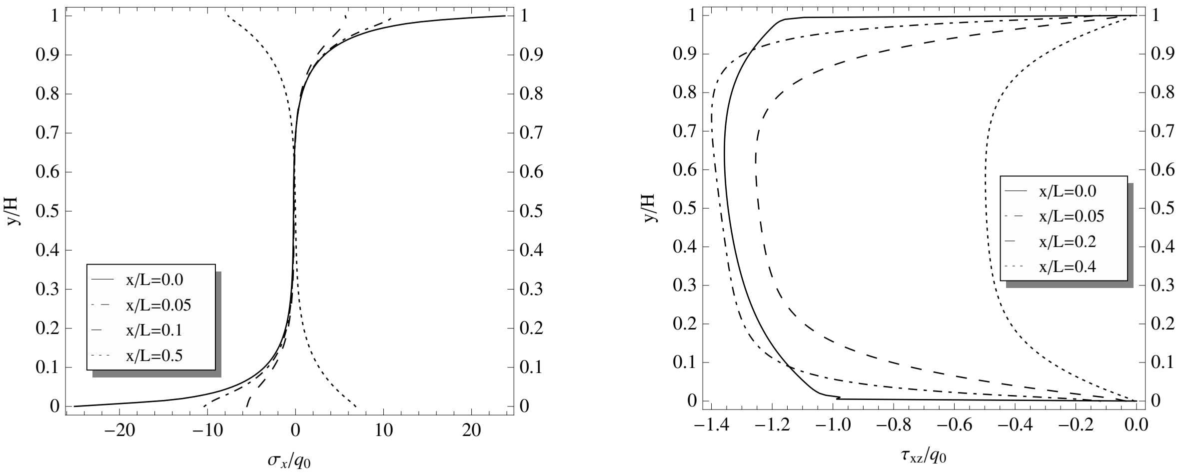

(a) Normalized axial stress

(b) Normalized shear stress

Figure 5.3 Distribution of normalized axial and shear stresses at different sections of the thick ($L/H = 4$) transversely isotropic plate

Figure(5.4) shows the distribution of normalized axial and shear stresses in a section $L/4$ far from either of the clamped edges for a range of aspect ratios. Although not shown, these results are similar to those presented in [54]. Furthermore, the effect of transverse shear in thick plates, which causes comparatively larger slopes at the clamped supports, can be clearly seen. With increasing aspect ratio the slopes at both supports vanish. This justifies the application of classical theory of plates for high aspect ratios.

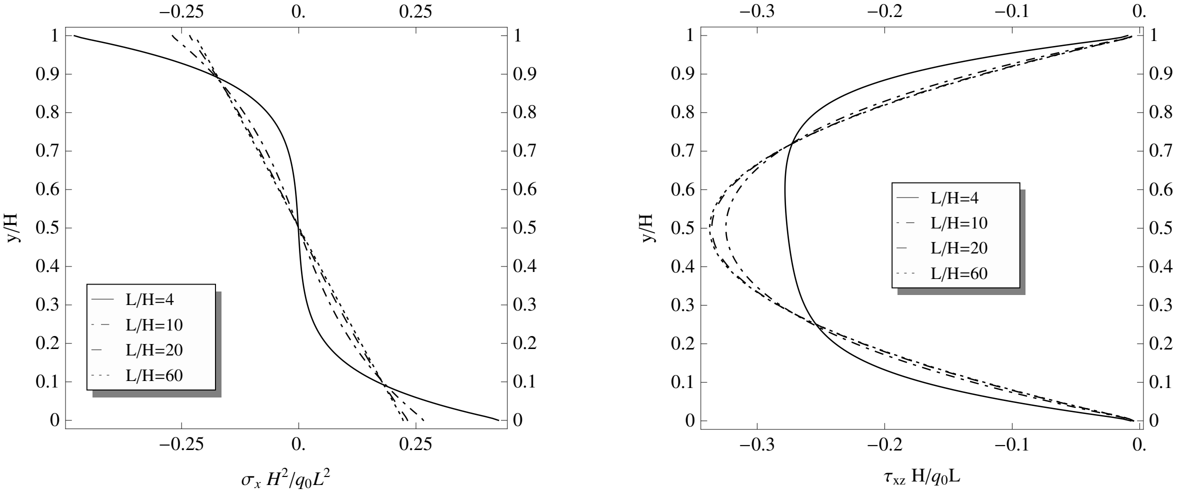

(a) Normalized axial stress at $L/2$

(b) Normalized shear stress at $L/4$

Figure 5.4 The distribution of normalized axial and shear stresses of the plate with four different aspect ratios

Figure (5.5) shows the distribution of normalized displacements in the mid surface of length and height of the plate. The longitudinal displacement is nearly linear above an aspect ratio of 20 as seen in figure(5.5a). This is due to the vanishing Saint Venant effect at $L/4$.

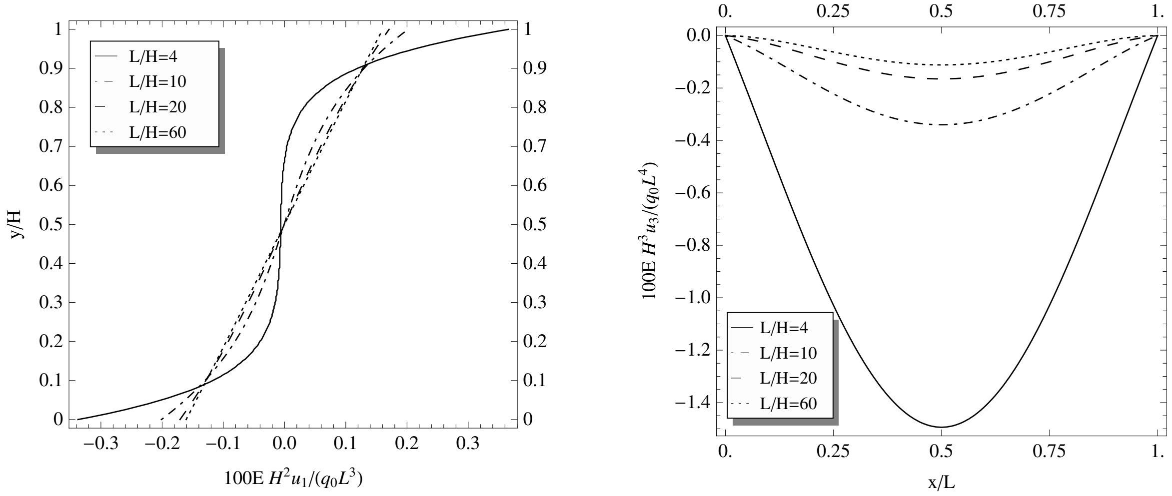

(a) Normalized displacement u_1 at $L/4$

(b) Normalized displacement u_3 at midplane surface

Figure 5.5 The distribution of normalized displacements of the plate with four different aspect ratios

5.3.2 Clamped-Clamped two layer plate

Bending of a two layer clamped-clamped plate, studied in [47], is investigated in this example. The material is again graphite-epoxy and fibers are arranged in the (0/90) degree orientation for the layers. The plate is under sinusoidal load, the layers are assumed to have equal thicknesses, and the loading is applied at the bottom of plate as

$$t^t_{X_1} = 0,\ t^t_{X_3} = 0,\ t^b_{X_1} = 0,\ t^b_{X_3} = -q_0 Sin(\frac{\pi X_1}{L}) \tag{5.16}$$

Normalized transverse normal, normal and shear stresses are shown and compared for two (L/H) aspect ratios of 4 and 10 in figures(5.6), (5.7) and (5.8), respectively. Additionally, tables(5.3 and 5.4) reflect the values of normalized deflection, normal, transverse shear and transverse normal stress and extension of normal (change of the thickness) for these aspect ratios. In this table, these values are quantitatively compared with those provided in [47]. Except for the value of $\frac{E}{q_0 H}\left[u_3\left(\frac{3L}{4}, H\right) - u_3\left(\frac{3L}{4}, \frac{H}{2}\right)\right]$ for an aspect ratio of 4, all results are in good agreements with [47]. Reference [47] have used exponential basis functions for the simulations which is capable of capturing large strains in thick multi-layered an-isotropic materials, but that method can only be applied for rectangle laminates.

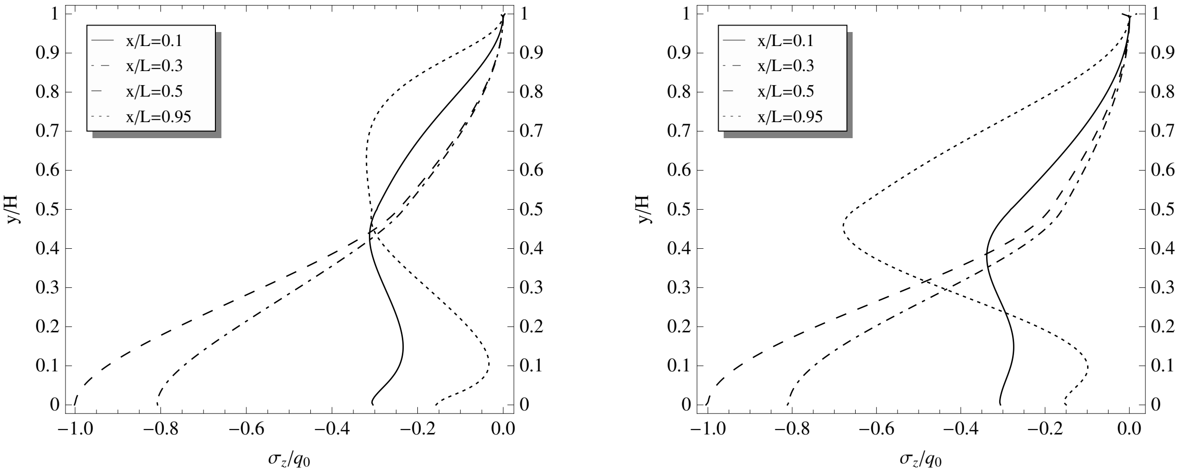

(a) Distribution of transverse normal stress in (L/H = 4) (b) Distribution of transverse normal stress in (L/H = 10)

Figure 5.6 The distribution of normalized transverse normal stress in example(5.3.2)

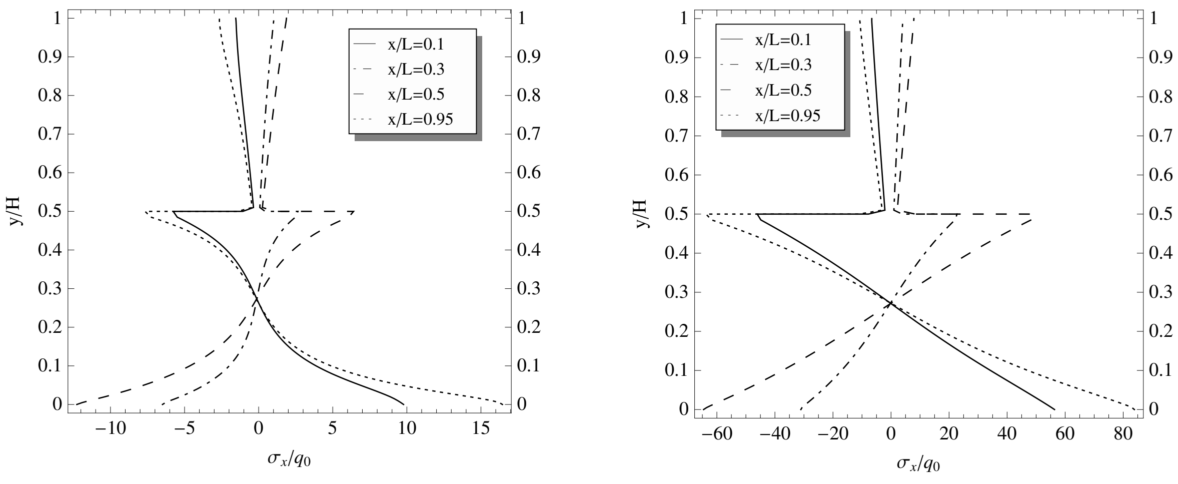

(a) Distribution of normal stress in (L/H = 4)

(b) Distribution of normal stress in (L/H = 10)

Figure 5.7 The distribution of normalized normal stress in example(5.3.2)

The inter-laminar continuity of transverse normal stress σ_{33} is evident in figure(5.6). The shear stress σ_{31} in figure(5.8) illustrates a discontinuity in slope between the two layers. Discontinuity of normal or in-plane stress σ_{11} between the layers is obvious in figure(5.7), where the impact of $\frac{L}{H}$ can be clearly seen. This phenomenon reflects the concept of C_z^0 requirements for simulation of laminar plates. Following [55], relations asserting the C_z^0 requirements are

$$
\begin{aligned}
u_i^{k,t} &= u_i^{k+1,b}, \quad \sigma_{i3}^{k,t} = \sigma_{i3}^{k+1,b} \\
\partial_z u_i^{k,t} &\neq \partial_z u_i^{k+1,b}, \quad \partial_z \sigma_{i3}^{k,t} \neq \partial_z \sigma_{i3}^{k+1,b}
\end{aligned}
\tag{5.17}
$$

Equation(5.17) assume that the layers are arranged in the z direction as depicted in figure(5.1). b and t reflect the bottom and top surfaces of the $k+1^{th}$ and k^{th} layer in the plate and assume that these layers are perfectly bonded together.

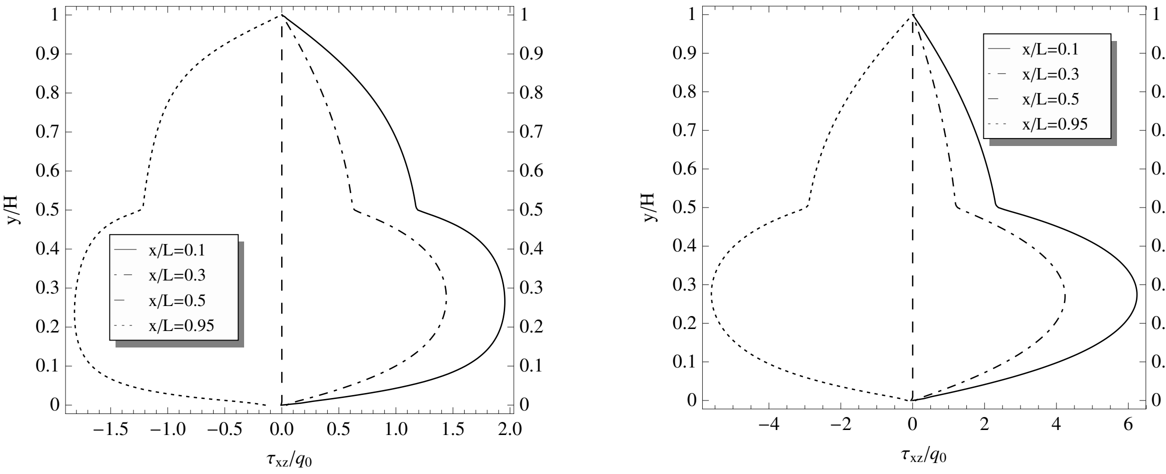

(a) Distribution of shear stress in (L/H = 4)

(b) Distribution of shear stress in (L/H = 10)

Figure 5.8 The distribution of normalized shear stress in example(5.3.2)

Table 5.3 Comparison between the normalized deflection, normal stress and transverse shear in two layers for aspect ratios of 4 and 10 between the present study and Shamsaei-Boroomand [47]

L/H	$\frac{100EH^3}{q_0L^4}u_3\left(\frac{L}{2},\frac{H}{2}\right)$		$\frac{10H^2}{q_0L^2}\sigma_{11}\left(\frac{L}{2},H\right)$		$\frac{10H}{q_0L}\sigma_{31}\left(0.3L,\frac{3H}{4}\right)$	
	[47]	*Present*	[47]	*Present*	[47]	*Present*
4	2.5624	2.3227	1.0454	1.1731	0.9208	1.0490
10	0.8827	0.8715	0.7853	0.7879	0.7822	0.7671
L/H	$\frac{100EH^3}{q_0L^4}u_3\left(\frac{L}{2},\frac{H}{2}\right)$		$\frac{10H^2}{q_0L^2}\sigma_{11}\left(\frac{L}{2},0\right)$		$\frac{10H}{q_0L}\sigma_{31}\left(0.3L,\frac{H}{4}\right)$	
	[47]	*Present*	[47]	*Present*	[47]	*Present*
4	2.5624	2.3227	-8.3595	-7.6705	3.8098	3.5874
10	0.8827	0.8715	-6.5255	-6.4574	4.1948	4.2163

Table 5.4 Comparison between the transverse normal stress and extension of normal (change of the thickness) in two layers for aspect ratios of 4 and 10 between the present study and Shamsaei-Boroomand [47]

L/H	$\frac{10}{q_0}\sigma_{33}\left(\frac{L}{2},\frac{3H}{4}\right)$		$\frac{E}{q_0 H}\left[u_3\left(\frac{3L}{4},H\right)-u_3\left(\frac{3L}{4},\frac{H}{2}\right)\right]$	
	[47]	*Present*	[47]	*Present*
4	-0.6595	-0.7269	-0.0215	-0.0685
10	-0.5556	-0.5444	-0.1540	-0.1684
L/H	$\frac{10}{q_0}\sigma_{33}\left(\frac{L}{2},\frac{H}{4}\right)$		$\frac{E}{q_0 H}\left[u_3\left(\frac{3L}{4},\frac{H}{2}\right)-u_3\left(\frac{3L}{4},0\right)\right]$	
	[47]	*Present*	[47]	*Present*
4	-6.4566	-6.6192	-0.2108	-0.2256
10	-6.3535	-6.3322	-0.2013	-0.2022

5.4 Morphological study of proximal femur

The femur is composed of a hard or outer layer and a soft, spongy or inner layer. These layers are known as cortical and cancellous layers, respectively. The upper or proximal extremity of the femur consists of a head, neck and the two trochanters. This region is the subject of the current study. Transversely isotropic behavior has been observed in both of these two layers [52], thus according to equation(5.2), material properties of each layer can be defined with four parameters of E, E_A, ν and G. In some studies these properties are asserted as a function of density of the bone. Section(5.7) provides more detail about this functional dependence. This section is intended to compare appropriateness of using linear and non-linear elasticity for simulating the proximal femur. For this reason, two dimensional mediolateral view of proximal femur is investigated in this section and morphological parameters for generating the finite element simulation is briefly discussed.

There are several morphological studies for the femur e.g. [56] and [57]. These measurements are usually made using computer aided design techniques on computed tomography (CT) scanned images of femurs and the provided data is typically used for designing standard femoral stems for cementless insertion. The geometrical parameters are the femoral head offset(A), femoral head diameter(B), femoral head relative position(C), neck diameter(N), mediolateral canal width 20 mm above the lesser trochanter(D), mediolateral canal width at the lesser trochanter(E), mediolateral canal width 20 mm below the lesser trochanter(F), mediolateral canal width at the isthmus(G), periosteal width at the isthmus(H) and the neck-shaft angle(J). Figure(5.9) is provided to reflect the mean of the above parameters in the Indian population [56].

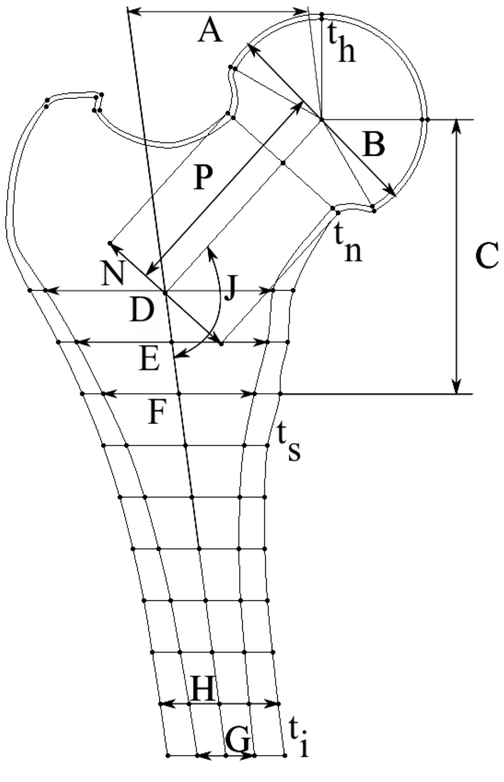

Figure 5.9 Morphological parameters for simulation of mediolateral section of proximal femur

Readers are directed to the tables provided in [56] for the mean and standard deviation of the parameters A, B, C, D, E, F, G, H and P in figure(5.9). Extension of canal diameter in anteroposterior, lateral, internal oblique, and external oblique diameters of the medullary canal in Indian population is also characterized in [58] for 10 different sections. In figure(5.9), t_h, t_n, t_s and t_i refer to cortical thickness in head, neck, shaft and isthmus sections, respectively. These values are provided in [59], and are used to generate the finite element geometry for simulation of the proximal femur. Additionally, the mean value of the neck diameter is specified in [57]. The finite element mesh generated using the aforementioned data is shown in figure(5.10).

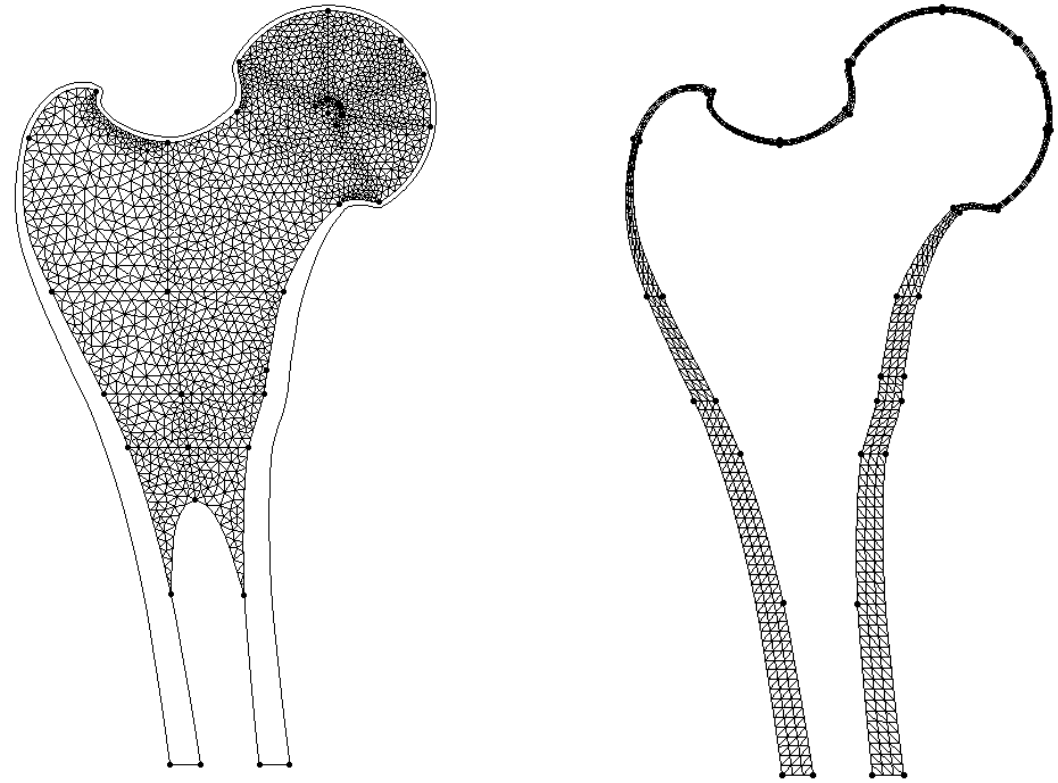

(a) Cancellous section of proximal femur

(b) Cortical section of proximal femur

Figure 5.10 Mediolateral finite element meshing for simulation of proximal femur

5.5 Proximal femur loading during the gait cycle

Analysis of the influence of the muscle groups on the internal loads of the femur can be found in [60]. Description of the loading during 10%(heel strike), 30%(mid stance), 45%(push off) and 70%(mid-swing) of the gait cycle is presented in appendix(C).

5.6 Density distribution in proximal femur

Bone adaptation is a process in which bone mass is modified by both mechanical and metabolic stimuli. The relationship between mechanical movement of the body and bone adaptation was suggested more than 100 years ago. There are several mathematical theories for bone adaptation that can be used to simulate bone changes during development, growth, adaptation and aging, e.g. [61] and [62]. A generalized theory for bone remodeling simulation can be found in [63]. In this research, a density distribution based on maximum Von-Mises strain in the bone during the gait cycle is chosen for the cortical and cancellous bones. Figure(5.11) illustrates the notional density distribution in the proximal femur.

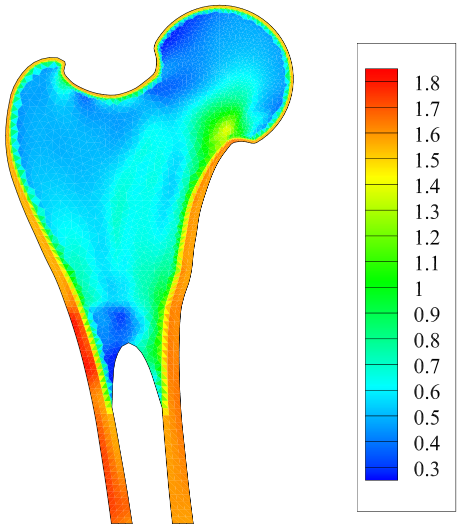

Figure 5.11 Notional density distribution in the proximal femur

5.7 Material properties of proximal femur

As discussed, many studies have clearly demonstrated the anisotropic behaviour of bone [64, 65]. In the literature, finite element simulations have used isotropic properties [], and orthotropic or transversely isotropic properties in the linear regime []. In the current work, non-linear transversely isotropic material models are used for the simulation of proximal femur. The study by Rudy et al. shows that anatomic variation in the elastic inhomogeneity and anisotropy of human femoral cortical bone tissue is consistent across multiple donors [66], for this reason, the data provided by Wirtz et al. [67] is chosen to obtain the material properties for the finite element simulation of the proximal femur. This requires specification of Young's modulus, shear modulus and Poisson ratio for cortical and cancellous layers of the bone. Compression, tensile and torsional strength of these layers are quantified subsequently.

5.7.1 Young's modulus

Young's modulus in the axial and transverse directions to the material orientation is a function of apparent density in both cortical and cancellous layers. The functional relations are approximated in the axial load direction and the transverse load directions [67] as

$$\begin{aligned} E_{A,cortical} &= 2065\rho^{3.09} \\ E_{cortical} &= 2314\rho^{1.57} \\ E_{A,cancellous} &= 1904\rho^{1.64} \\ E_{cancellous} &= 1157\rho^{1.78} \end{aligned} \tag{5.18}$$

The Young's modulus in equation(5.18) are in MPa or N/mm^2 and the apparent density is defined in g/cm^3.

5.7.2 Poisson's ratio

The cited values for Poisson's ratio span over a large range, thus the average values are regarded in this work. These values are between 0.2 and 0.5 with the average of 0.3 for cortical section and between 0.01 and 0.35 with the average of 0.12 for the cancellous bone.

5.7.3 Shear modulus

The shear modulus of cortical femoral bone is assumed to be between 2840 and 4040 MPa with the average of 3280 MPa [64]. For the cancellous bone the study in [68] shows that the shear modulus is between 8 and 40 MPa with the average of 24 for apparent densities between 0.1 and 0.8 g/cm^3.

5.7.4 Compressive strength, tensile strength and torsional strength

The compressive strength of the cortical and cancellous bones are a function of apparent density. Defining these strengths in MPa or N/mm^2, and the apparent density in g/cm^3, the following is utilized

$$\begin{aligned}
\sigma_{A,cortical} &= 72.4\rho^{1.88} \\
\sigma_{cortical} &= 37\rho^{1.51} \\
\sigma_{A,cancellous} &= 40.8\rho^{1.89} \\
\sigma_{cancellous} &= 21.4\rho^{1.37}
\end{aligned} \tag{5.19}$$

In equation(5.19), subscript A refers to the material direction and lack of this index indicates the direction perpendicular. Studies show that the tensile strength in the cortical section is not a function of density and defined as 150 MPa. However, in the cancellous section this value varies linearly between 3 and 15 MPa for apparent densities between 0.2 and 0.5 g/cm^3.

Torsional strength for the cortical section is between 49 to 68 MPa with an average of 58.5 MPa. Shear strength of the cancellous bone is not addressed in [67] and the data used in this work is gathered from [69]. Torsional strength in the direction of the material and perpendicular to this direction are possibly different in nature, however due to lack of data these two properties are considered the same in this research.

5.8 Orientation of orthotropic material properties in a femur

Wolff's law Postulates that trabecular structure pattern of the cancellous bone coincides with the directions of the principal stresses. Because of the bone remodeling, effective material properties such as stiffness and strength are higher in these directions, which are the direction of the maximum stress. A procedure to orient orthotropic properties in a proximal femur finite element model using the directions of the principal stresses produced by a physiological load scheme is developed in [52]. Reference [70] has also suggested that trabecular pattern is defined by extreme loading directions. Following the same concept and procedure in [52], multiple sets of loading during the gait cycle is used to adjust the maximum principal direction of each element to orient the transversely isotropic direction in the bone. Figure(5.12) shows the excellent agreement with the actual bone the results provided in [52]. This figure highlights trabeculae groups: (1) principal compressive, (2) principal tensile, (3) secondary compressive, (4) secondary tensile and (5) greater trochanteric.

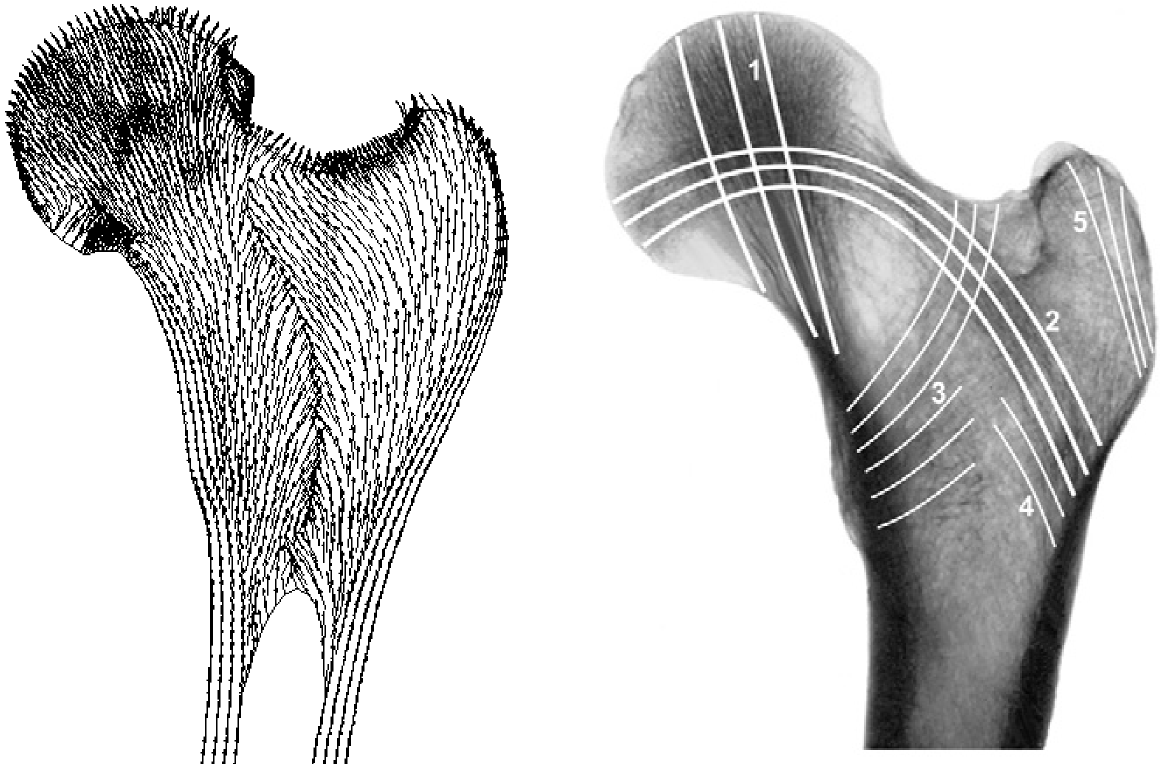

(a) Present study

(b) Radiographic scan of the proximal femur with highlighted trabeculae groups [52]

Figure 5.12 Material orientation of bone using maximum principal direction

5.9 Analysis of proximal femur during the gait cycle

Loading of proximal femur during the gait cycle is tabulated in appendix(C). Figures(5.13), (5.14), (5.15) and (5.16) depict the Von-Mises strain distribution in the proximal femur during the gait cycle. These figures illustrate the difference in results between linear elasticity and non-linear hyper-elastic simulation.

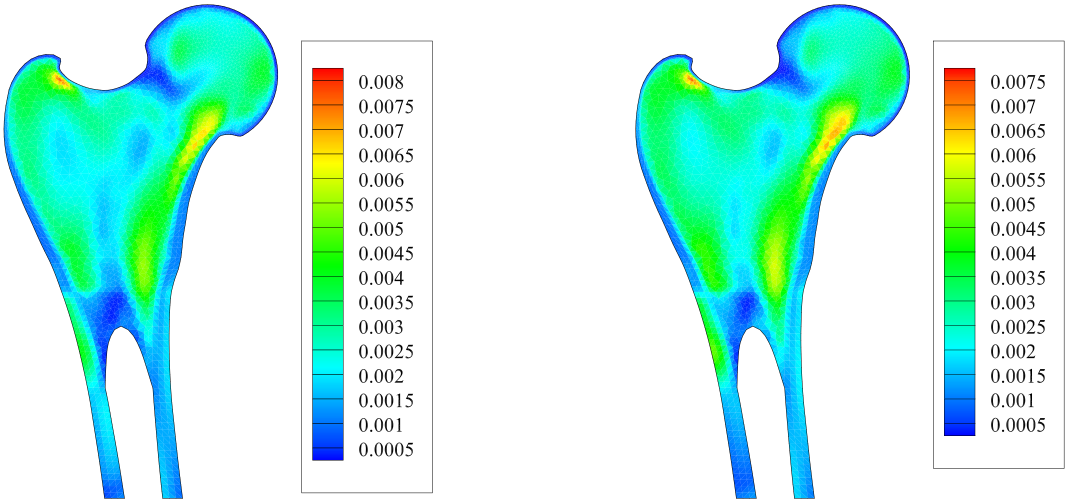

(a) Linear elastic solution of Von-Mises strain (b) Non-linear hyper elastic solution of Von-Mises strain

Figure 5.13 Comparison of linear and non-linear elasticity in Von-Mises strain in 10% of gait cycle

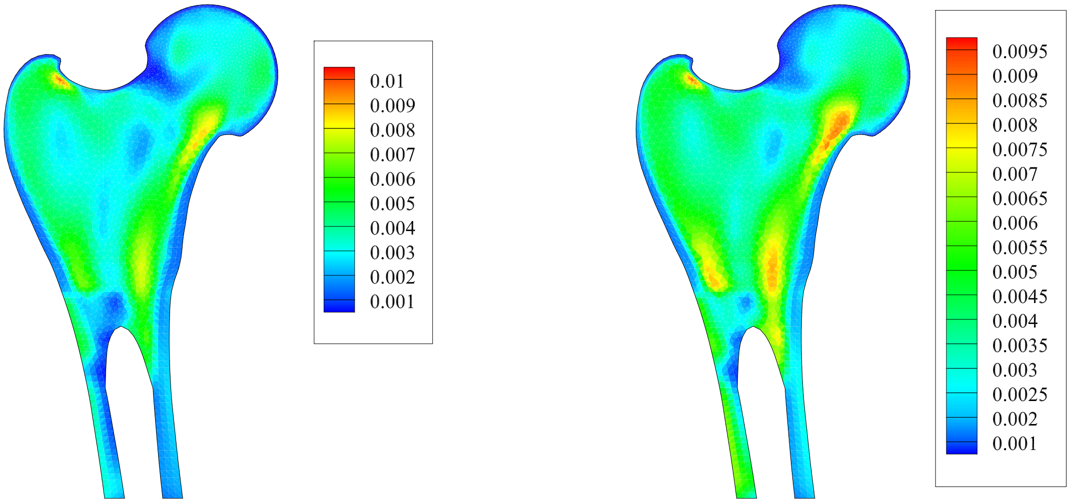

(a) Linear elastic solution of Von-Mises strain (b) Non-linear hyper elastic solution of Von-Mises strain

Figure 5.14 Comparison of linear and non-linear elasticity in Von-Mises strain in 30% of gait cycle

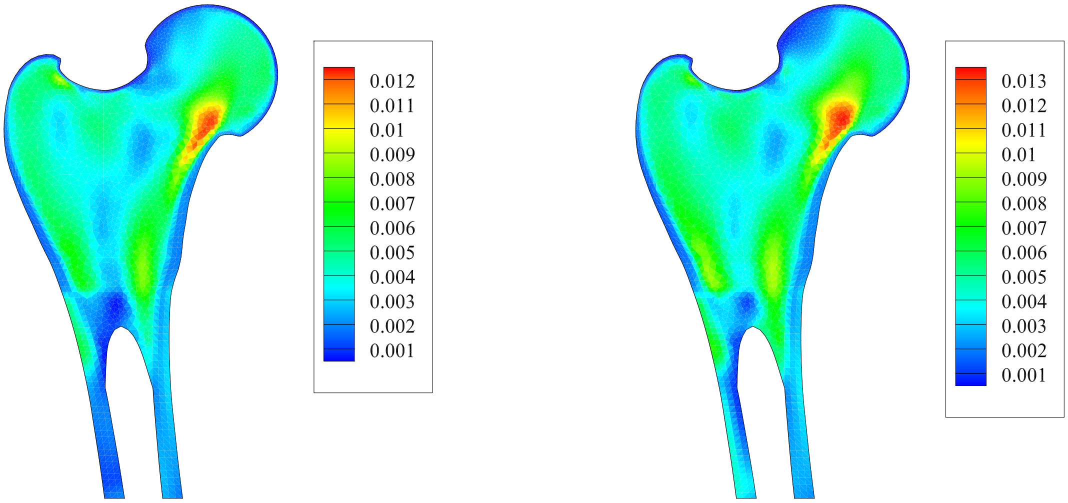

(a) Linear elastic solution of Von-Mises strain (b) Non-linear hyper elastic solution of Von-Mises strain

Figure 5.15 Comparison of linear and non-linear elasticity in Von-Mises strain in 45% of gait cycle

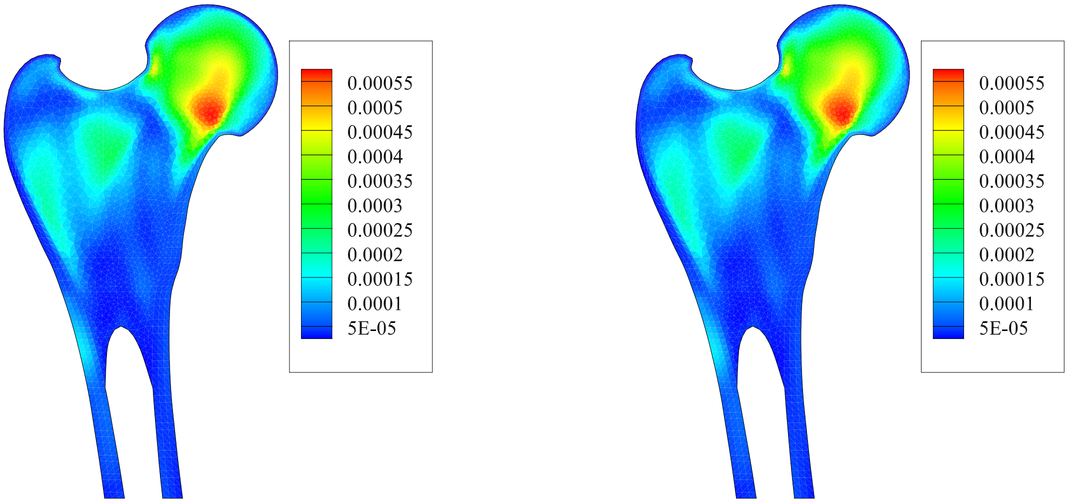

(a) Linear elastic solution of Von-Mises strain (b) Non-linear hyper elastic solution of Von-Mises strain

Figure 5.16 Comparison of linear and non-linear elasticity in Von-Mises strain in 70% of gait cycle

As expected, the maximum strain occurs at 45% of the gait cycle. Additionally, these results indicate that the maximum strain occurs in the bone neck, which is an indicator that the possibility of fracture will occur in this region.

Differences between the linear elastic and non-linear neo-Hookean hyper elastic and Saint Venant-Kirchhoff simulations of the 45% gait cycle are shown in figures(5.17) and (5.18) respectively. The absolute difference is calculated as the value of linear elastic minus the non-linear counterparts and the percentage values are the absolute values divided by the linear values. Results indicate more strain (or plus sign difference) in the linear elasticity than the non-linear simulation in the femoral neck and lesser trochanter, which are the places of interest in terms of the failure analysis. This may be a potential cause of error to suggest a greater probability of failure in the bone when linear elasticity is used for simulation. In generating the data for the percent differences in the figures, the infinitesimal difference between the linear and non-linear and infinitesimal linear strains are neglected and could cause artificial subtracting and rounding errors. In the figures, the percent difference is between -0.5 to 0.5 in most of the domain with a color contrast that shows which area is close to zero and which is further from zero. This difference is a measure that indicates that the cancellous part is the softer material. This potentially justifies the use of non-linear simulation over the linear simulation in aging bones that are regarded spongier or softer.

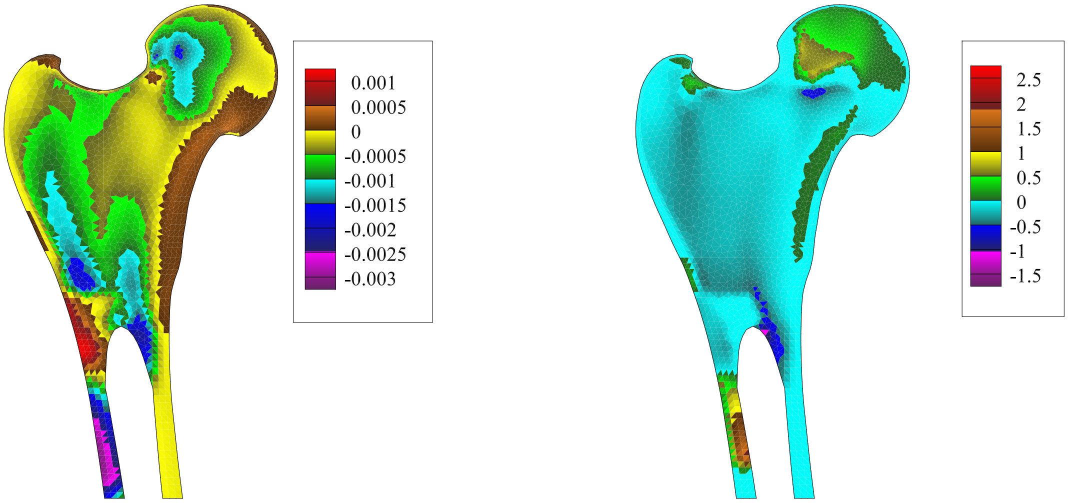

(a) Absolute difference

(b) Percent difference

Figure 5.17 Absolute and percent difference of linear and non-linear neo-Hookean hyper elasticity in Von-Mises strain in 45% of gait cycle

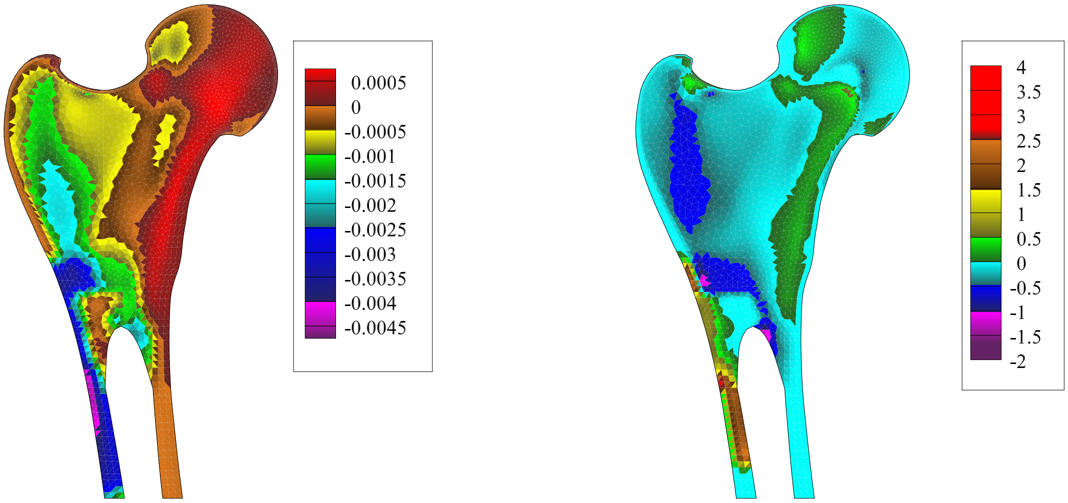

(a) Absolute difference

(b) Percent difference

Figure 5.18 Absolute and percent difference of linear and non-linear Saint Venant hyper elasticity in Von-Mises strain in 45% of gait cycle

CHAPTER 6

UNCERTAINTY QUANTIFICATION IN SIMULATION OF FAILURE IN PROXIMAL FEMUR

In this chapter, the concept of uncertainty quantification(UQ) and the possibilities of using UQ in simulations are discussed. With advances in the simulation techniques and computational power, the investigation concerning the fidelity of the results, regarding the assumptions typically made in the simulation process, is becoming more necessary. With the ability to accurately quantify errors and uncertainties, computer simulations will become much more powerful tools in robust design procedures. The large variation of biomechanical properties in the human population justifies the need for UQ in computational simulation. For this purpose, application of UQ in finding an interval around the deterministic results where the true results are expected is discussed in section(6.5.1). Ranking of the uncertainties through sensitivity analysis is illustrated in section(6.5.2), and finally design and optimization based on UQ is discussed at section(6.6). Equations of failure are defined in the composite materials and maximum failure strains are investigated in one section of the femur. These techniques are susequently illustrated in simulation of proximal femur in section(6.7)

6.1 Introduction

The ability for producing an estimate of the uncertainties in a calculation is an essential procedure in improving the design process. Because of the various assumptions made in the computational simulation process, the calculated results are likely to be different than the substantive outcome. Hence, the ability to introduce error bars or quantify the uncertainty in the simulation is pivotal. These assumptions, and consequently the simulation outcome, may introduce unexpected errors and sometimes unanticipated failure in the behavior of a system. Uncertainty quantification is the procedure of quantitatively characterizing and reducing uncertainties in the simulation. In computational modeling and simulation, uncertainty is regarded as a potential deficiency in any phase or activity of the modeling process, and is due to a lack of knowledge [71]. Conversely, errors are defined as deficiencies of the models or the algorithms employed, such as implementation or round off errors.

Calculating possible differences between the actual and calculated results generates the error bars for the simulation. These error bars can be used further for robust design or optimization under uncertainty, which is a reliable device for managing and compromising between the optimal performance and stability of performance. In spite of the wide spread use of modeling and simulation tools, it remains difficult to provide objective confidence levels in the quantitative information obtained from numerical predictions [72]. For this reason one of the main objectives in UQ is to provide error bars on the simulations results. Some examples of using UQ in computational fluid dynamics, and environmental and biological systems, can be found in [73] and [74], respectively.

6.2 How to handle uncertainties?

Uncertainty quantification is comprised of two steps: understanding the sources of uncertainties, and the propagation process of the uncertainties. These two issues are briefly addressed in the next two sections. The concept of uncertainty analysis is described and the design and optimization under uncertainties is addressed subsequently.

6.3 Sources of uncertainties

Uncertainties related to the physical description of the problem of interest [75] are due to

- initial or boundary conditions.
- geometric parameters of a problem.
- material properties of a problem and from
- mathematical models that describe physical processes.

Uncertainties are related to the physics of the problem of interest. Numerical errors associated with numerical solution of the mathematical problem include

- discretization errors of differential equations governing the problem of interest,
- Finite precision floating point errors and
- residual errors associated with iterative solvers.

In [76] a classification of the uncertainties in the concept of risk assessment is presented. This uncertainty taxonomy classifies uncertainty into epistemic and aleatory. Aleatory uncertainty or variability or stochastic uncertainty is the inherent variation of the physical system and cannot be eliminated or reduced by collection of more information or data. Some examples of this kind of uncertainty are material properties, operating conditions, and manufacturing tolerances. This uncertainty can be defined in the probabilistic frame work.

Epistemic uncertainty is a potential inaccuracy in any phase or activity of the modeling process that is because of lack of knowledge. Examples of this uncertainty, within fluid dynamics, is the turbulence modeling assumptions, and can be reduced with an increased state of knowledge or collection of more data. This uncertainty can be created from assumptions introduced in the derivation of the mathematical model and can not be defined in the probabilistic framework.

Once the sources of uncertainties are quantified, one should determine how these uncertainties propagate through the simulation. These quantities, also known as objective functions, are the primary functions of interest in the simulation and provide information regarding the performance of the system. They are functions of all the independent variables or design variables that describe the sources of uncertainty.

6.4 Uncertainty propagation

As discussed in the previous section, uncertainty quantification involves two steps: determination of the uncertainty sources, and analysis of their propagation throughout the simulation. Uncertainty propagation methods can generally be classified as intrusive and non-intrusive. Intrusive methods require the formulation and solution of a stochastic version of the original model, while nonintrusive schemes require multiple solutions of the original model.

6.4.1 Intrusive propagation

Intrusive UQ methods require reformulating the mathematical equations and re-describing the problem of interest with regard to the uncertainties. This propagation involves reformulation of governing equations and modification to the simulation procedure to incorporate uncertainty directly into the system. As this definition implies, this propagation is problem dependent and is specific for each problem and discipline. Typical example of this type is the Polynomial Chaos expansion based approaches, which represent a stochastic process with expansion of orthogonal polynomials [77]. An example of using the intrusive method in failure analysis of bone described in [78] is discussed later in this chapter. In the next section, some widely used non-intrusive approaches, including Monte Carlo simulation method, Response Surface Methods and sensitivity-based methods or Taylor series approximation are explained.

6.4.2 Non-intrusive propagation

Non-intrusive UQ methods use ensembles of simulations. Simulation ensemble members are created by sampling the uncertain inputs according to various sampling schemes. In non-intrusive approaches there is no need to modify the simulation code and these methods use the computer simulation model as a black-box. The impact of the input uncertainties can then be analyzed for the output quantities of interest or objective functions. For the non-intrusive schemes, Monte-Carlo methods, response surface methods and sensitivity based schemes are commonly used.

6.4.2.1 *Monte-Carlo methods*

Monte Carlo Simulation (MCS) methods are sampling-based procedures [79]. During this procedure, repeated sampling and simulation to compute the statistics of the response quantities of the simulation is performed. Level of accuracy of MCS is dependent on the number of samples and simulations. Thus, MCS methods can give statistics of the results with arbitrary levels of accuracy. For this reason MCS is usually used for validation of new uncertainty analysis techniques.

The basic MCS procedure with probabilistic uncertainties includes three steps:

1. A set of n data points are randomly sampled from the assumed distribution of the data. Unbiased random sampling procedures are discussed in [80].

2. A simulation is performed for each data point or sample to obtain the corresponding system response. This procedure forms n sample pairs $[\mathrm{x}_{(i)}, y_{(i)}]$, where vector x is the vector of design variables and y is the system response.

3. Analyzing the samples by defining the expected value of function $\varphi\left(y\right)$ as

$$\mathrm{E} = E\left(\varphi\left(y\right)\right) = \int \varphi\left(f\left(\mathrm{x}\right)\right) p\left(\mathrm{x}\right) d\mathrm{x} \tag{6.1}$$

   where in equation(6.1), $y = f(\mathrm{x})$ with y being the simulation output and $p(\mathrm{x})$ is the probability density function of vector x. When $\varphi\left(y\right) = y^k$, E is the estimate for the k^{th}

statistical moment. The integral in equation(6.1) can be approximated as

$$\mathrm{E} \approx \tilde{\varphi} \approx \frac{1}{n} \sum_{i=1}^{n} \varphi\left(y_{(i)}\right) \tag{6.2}$$

Thus in equation(6.2) if $\varphi\left(y\right) = y$, the sample average can be defined as

$$\bar{\mu} \approx \frac{1}{n} \sum_{i=1}^{n} y_{(i)} \tag{6.3}$$

And the variance is estimated as

$$\sigma^2 \approx \frac{1}{n-1} \sum_{i=1}^{n} \left(y_{(i)} - \bar{\mu}\right)^2 \tag{6.4}$$

The accuracy of the estimations in equations(6.3) and (6.4) is defined as the standard error or

$$standard\ error = \frac{\sigma}{\sqrt{n}} \tag{6.5}$$

Equation (6.5) indicates that the accuracy the MCS is a function of sample size, which is computationally problematic in complex simulations.

6.4.2.2 Response surface methods

Response Surface Methods (RSM) seeks to determine the relationship between several input variables and one or more response variables or objective functions. The main idea of RSM is to use a sequence of designed experiments to obtain an optimal response. In this procedure, an experimental design is used to select model inputs for developing a response surface replacement for the original model. This response surface is used further in subsequent uncertainty and sensitivity analyses. These methods have been widely studied in [81] and [82]. Both uncertainty and sensitivity analyses are straightforward once the necessary response surface replacement has been developed. Design of experiments or experimental design procedure to be used in response surface fitting have been studied in [81]. In [83] iterative improvements in the response surface fit is utilized. Difficulties in constructing appropriate response surface in problems with nonlinearities or discontinuities may be considered as a drawback of the RSM [74]. It is not feasible to completely present the background and research being conducted in this discipline. Moreover, reviews and the relative merits of competing methods may be found within the cited literature.

6.4.2.3 Sensitivity-based methods

An alternative approach is to use sensitivity-based analysis for propagating this uncertainty throughout the solution [84]. Use of this method offers significant reductions in computational time which has significant benefits in problems with a large number of input variables and for those that involve nonlinear models.

Local sensitivity analyses are mostly based on a Taylor series expansion to the model under consideration. Second order Taylor series for a function of vector x around an adjacent vector x_0 is defined as

$$y\left(\mathrm{x}\right) \approx f\left(\mathrm{x}_0\right) + \sum_{i=1}^{n} \frac{\partial f\left(\mathrm{x}_0\right)}{\partial x_i}\left(x_i - x_0\right) + \frac{1}{2}\sum_{i=1}^{n}\sum_{j=1}^{n} \frac{\partial f^2\left(\mathrm{x}_0\right)}{\partial x_i \partial x_j}\left(x_i - x_0\right)\left(x_j - x_0\right) \tag{6.6}$$

Furthermore, the expected value of $y\left(\mathrm{x}\right)$ can be defined as

$$\bar{\mu} = E\left(y\right) \approx \int_{-\infty}^{\infty} y\left(\mathrm{x}\right) p\left(\mathrm{x}\right) d\mathrm{x} \tag{6.7}$$

On substitution of the equation(6.6) into equation (6.7) gives

$$\begin{aligned}\bar{\mu} = & \underbrace{\overbrace{\int_{-\infty}^{\infty} f\left(\mathrm{x}_0\right) p\left(\mathrm{x}\right) d\mathrm{x}}^{f(\mathrm{x}_\mu)} + \sum_{i=1}^{n} \frac{\partial f\left(\mathrm{x}_0\right)}{\partial x_i} \overbrace{\int_{-\infty}^{\infty} \left(x_i - x_0\right) p(x_i)\, dx_i}^{0}}_{First\ Order} + \\ & \underbrace{\frac{1}{2}\sum_{i=1}^{n}\sum_{j=1}^{n} \frac{\partial f^2\left(\mathrm{x}_0\right)}{\partial x_i \partial x_j} \int_{-\infty}^{\infty}\int_{-\infty}^{\infty} \left(x_i - x_0\right)\left(x_j - x_0\right) p(x_i) p(x_j)\, dx_i\, dx_j}_{Second\ Order}\end{aligned} \tag{6.8}$$

In equation (6.8), $f\left(\mathrm{x}_\mu\right)$ is the value of function $y\left(\mathrm{x}\right)$ at the mean values of variables in vector x.

The term associated with the second order Taylor series can be simplified to

$$\frac{1}{2}\sum_{i=1}^{n}\sum_{j=1}^{n} \frac{\partial f^2\left(\mathrm{x}_0\right)}{\partial x_i \partial x_j} \int_{-\infty}^{\infty}\int_{-\infty}^{\infty} \left(x_i - x_0\right)\left(x_j - x_0\right) p(x_i) p(x_j)\, dx_i\, dx_j = \frac{1}{2}\sum_{i=1}^{n}\sum_{j=1}^{n} \frac{\partial f^2\left(\mathrm{x}_0\right)}{\partial x_i \partial x_j} \sigma_i \sigma_j \tag{6.9}$$

Implementing the computational equation for variance, the variance of $y\left(\mathrm{x}\right)$ is defined as

$$\sigma^2 = E\left(\left(y\left(\mathrm{x}\right) - \bar{\mu}\right)^2\right) = E\left(\left(y\left(\mathrm{x}\right)\right)^2\right) - \bar{\mu}^2 \tag{6.10}$$

and it can be shown that equation(6.10) reduces to

$$\sigma^2 \approx \overbrace{\sum_{i=1}^{n}\left(\frac{\partial f\,(\mathrm{x})}{\partial x_i}\sigma_{x_i}\right)^2}^{First\,Order} + \overbrace{\frac{1}{2}\sum_{i=1}^{n}\sum_{j=1}^{n}\left(\frac{\partial f^2\,(\mathrm{x}_0)}{\partial x_i \partial x_j}\sigma_{x_i}\,\sigma_{x_j}\right)^2}^{Second\,Order} \tag{6.11}$$

Following equations (6.11) and (6.8), if the perturbation is small the mean and variance of the objective function only depends on the first derivative of the objective function y with respect to the design variables x_i. This derivative is referred to as the sensitivity of the objective function with respect to a design variable [82].

A number of techniques exist to calculate these derivatives. Among them are direct differentiation, discrete-adjoint variable approach, complex Taylor series expansion method and finite difference. Description of these methods can be found in [85] and [4].

6.5 Uncertainty analysis

Uncertainty analysis seeks the interval around a result where the true result is expected to lie with a certain degree of confidence. As discussed before, one application of the uncertainty quantification is to define an error bar for computed solution that the true solution resides within. While rooted in experimental procedures, the same techniques can be used to quantify uncertainty in simulations.

6.5.1 Mathematical interval

In general, for experimental uncertainty analysis [86], the result or objective function is determined by a data reduction equation and is a function of k measured design variables.

$$y\left(\mathrm{x}_0\right) - \Delta y \leq y\left(\mathrm{x}\right) \leq y\left(\mathrm{x}_0\right) + \Delta y \tag{6.12}$$

The uncertainty in the result is then a function of the uncertainty in the measured variables, where the true value for the result y is then assumed to lie in the interval. The predominant means of characterizing uncertainty in physical processes is via probabilistic analysis, which requires the probabilistic distributions of the uncertain input parameters or data. The common approach adopted within experimental uncertainty analysis is to use the uncertainty in the input parameters to quantify the uncertainty in the output responses as

$$\Delta y = \sqrt{\sum_{i=1}^{n} \left(\frac{\partial f\left(\mathrm{x}_0\right)}{\partial x_i} \Delta x_i \right)^2} \tag{6.13}$$

Uncertainty propagation of this form has been addressed with interval mathematics [87]. Interval mathematics, as the name implies, is an arithmetic defined on a set of intervals, as opposed to real numbers. The purpose of such analysis is to estimate the bounds on computational output knowing the bounds, or specified interval, of the input.

6.5.2 Ranking of uncertainties

Another application of uncertainty quantification is to rank the uncertainty sources which might dominate the response of the system, i.e. to find the design variables that affect the objective functions the most. As is shown in equations (6.12) and (6.13), the bound of function $y = f(x)$, defined as Δy, is a function of derivatives of y with respect to design variables. Also note that large values of sensitivity derivatives do not necessarily translate into critical uncertainties. This is because the input variability may be very small in a specific device of interest. Having found the most influential design variables, the design procedure can be changed to be more robust. More discussion about how to use uncertainty quantification in the design procedure is presented in the next section.

6.6 Optimization under uncertainty

Another outcome of UQ is to estimate the likelihood of a behavior of a system of interest based on the system uncertainties and the effect of the uncertainties on the specific behavior of the problem. This knowledge can be used in the design procedure of a system or a device. Reliability based optimization and robust design optimization are the two main motivating reasons for applying the science of uncertainty quantification.

Parameters of interest are the system's degree of tolerance to variation of a variable, thus robustness is defined as the insensitivity of the system to the variable. Reliability is defined as the likelihood that a system will perform its intended function for a specified time interval under stated conditions [88], or the likelihood that a component or a complete system will perform its intended function without failure for a specified period of time under stated operating conditions. Accordingly, there are two different uncertainty-based design optimization methods, i.e. robust design and reliability-based design optimization.

Regarding these definitions, two methods for implementing UQ in the design process can be defined. First is to improve the robustness or insensitivity of a system to an uncertain variable represents the robust design process. The second scheme is to improve reliability of the design and decrease the chance of function failure under potential critical conditions, hence to keep the system in normal state with required level of likelihood under extreme events [72].

6.7 Sources of uncertainty in the simulation of proximal femur

Personalized computational simulation of proximal femur requires in vivo computed tomography (CT) data that reflects the morphology of the bone. Taddei et al. [89] found that geometric representation of the bone is a very important factor in calculating stresses and strains in the proximal femur. This highlights the artifact error that might be generated during the CT procedure. Another factor in the simulation is the personalized physiological loading conditions. Due to inter- and intra-patient variations in the quantity and direction of the loading, these are regarded as important sources of uncertainties as well. Wille et al. [78] have discussed this effect using stochastic hip contact force, representing realistic variability of experimental data. Determination of exact material properties is regarded as another obstacle in the modeling process. These parameters are highly variable in human tissues, for example due to inhomogeneous density distribution and between patients because of differences in sex, age or physiological anatomy [90] and [91]. Finally, as previously discussed, constitutive equations for the simulation such as linear and non-linear equations and iso/ortho-tropic behavior represent epistemic source of uncertainty in the simulation which has not been studied.

An excellent overview of probabilistic studies performing uncertainty quantification for computational modeling of the human femur can be found in [78]. The reference specifies the sources of uncertainty and uncertainty propagation scheme exploited in each of the studies in the litterature. There are three studies by Wille et al. [78], Laz et al. [90] and Taddei et al. [89] which are devoted to uncertainty quantification of femurs without stems. In all of these studies single layer, linear elastic, inhomogeneous isotropic material properties were assumed for the bone tissue. In the current research, non-linear transversely isotropic multi-layer behavior of bone is utilized, and uncertainties due to material selection are ascertained.

In all of the aforementioned studies, a stochastic relationship between density and modulus of elasticity representing realistic variability of experimental data is considered. In the study by Wille et al. [78], effect of stochastic hip contact forces is considered as well. In the present work, six material properties consisting of density, the Poisson's ratio, and the shear modulus of cancellous and cortical layers as well as two geometric uncertainties of femoral head offset(A) and femoral head relative position(C) are regarded as the uncertainties.

Monte-Carlo scheme and a probabilistic framework based on polynomial chaos are used in [89] and [78] respectively. Furthermore a probabilistic modeling software is used in [90] for the uncertainty propagation. In the present work, a sensitivity based First-Order Second-Moment (FOSM) scheme is used for the uncertainty propagation. This scheme is computationally less expensive than the other methods listed above, but requires calculation of the sensitivity derivatives of objective functions with respect to the uncertain parameters.

Maximum Von Mises stress, various descriptive statistics of the response variable, estimates of its distribution e.g. probability density function, sensitivity parameters, and probabilities of failure are investigated in the above mentioned references. The focus of this work is to use local sensitivity analysis for the uncertainty propagation in the simulation of failure in proximal femur using a sensitivity based FOSM scheme. The effect of sensitivities on deviation of failure analysis of femur is sought. Thus, in the next section, the equations of failure in multi-layer orthotropic materials are described. Mean, standard deviation and variance of failure modes are investigated for loading in 45% of gait cycle. Sensitivity analysis is performed to identify the most influential factors in the failure analysis. Solution mathematical interval of failure discussed in section(6.5.1) is subsequently analyzed.

6.8 Failure analysis of proximal femur

Hip fracture is an important cause of invalidism in elderly. Annually over 800,000 total hip replacements are conducted worldwide, and the cost of treatment in the United States is estimated to be approximately $7.1 billion annually [92]. Sensitometry which is a common tool in prediction of the hip fracture probability is the process of assessing a patient's risk of hip fracture involving local estimates of bone density. Prediction of femoral fracture load using automated finite element modeling has been investigated in [93]. That study investigates whether automatically generated, computed tomographic (CT) scan-based linear elastic isotropic finite element (FE) models can be used to estimate femoral fracture load in vitro. In contrast, in the present study, a non-linear transversely isotropic finite element analysis is used in the failure analysis of the proximal femur.

6.8.1 Failure criteria

The proximal femur is a multi-layered composite material, thus the equations defined in [94] are used for failure analysis of the bone. Failure criteria for composite laminates can be classified into two groups, independent failure criteria and polynomial failure criteria.

6.8.1.1 Independent failure criterion

This criterion is based on the three modes of failure and failure is assumed to occur if any of the following conditions are satisfied [94]:

$$\begin{aligned} &First\,failure: \ |\sigma_{11}/X| \geq 1, \ Second\,failure: \ \sqrt{\sigma_{13}^2 + \sigma_{13}^2} \geq \sigma_{fs} \\ &Third\,failure: \ |\sigma_{22}/Y| \geq 1, \ Fourth\,failure: \ \sqrt{\sigma_{21}^2 + \sigma_{23}^2} \geq \sigma_{ms} \\ &Fifth\,failure: \ |\sigma_{33}/Z| \geq 1, \ Sixth\,failure: \ \sqrt{\sigma_{31}^2 + \sigma_{32}^2} \geq \sigma_{ms} \end{aligned} \tag{6.14}$$

In these relations, direction 1 refers to the material direction and the other directions are perpendicular to this direction. σ_{ms} is the fiber shear strength and σ_{fs} is the transverse shear strength. X, Y and Z are the normal tensile or compressive strength in the 1, 2 or 3 directions depending on tensile or compressive behavior of σ_{ii}. Equation(6.14) shows six failure criteria. Three of these are in the axial directions, and three represent shear failures. In two dimensional problems that disregard the normal plane, these modes diminish to four. Assuming that σ_{ms} and σ_{fs} are the same, the second and fourth failure criteria will provide similar results.

6.8.1.2 Polynomial failure criterion

One particular form of of this criterion is the Tsai-Wu criterion [94], which is defined as:

$$
\begin{aligned}
&F_i\sigma_i + F_{ij}\sigma_i\sigma_j \geq 1\\
&F_1 = \left(\frac{1}{X_T} - \frac{1}{X_C}\right),\ F_2 = \left(\frac{1}{Y_T} - \frac{1}{Y_C}\right),\ F_3 = \left(\frac{1}{Z_T} - \frac{1}{Z_C}\right),\ F_{11} = \left(\frac{1}{X_T X_C}\right),\ F_{22} = \left(\frac{1}{Y_T Y_C}\right)\\
&F_{33} = \left(\frac{1}{Z_T Z_C}\right),\ F_{44} = \left(\frac{1}{R^2}\right),\ F_{55} = \left(\frac{1}{S^2}\right),\ F_{66} = \left(\frac{1}{T^2}\right),\ F_{12} = -\frac{1}{2}\sqrt{\frac{1}{X_T X_C Y_T Y_C}}\\
&F_{13} = -\frac{1}{2}\sqrt{\frac{1}{X_T X_C Z_T Z_C}},\ F_{23} = -\frac{1}{2}\sqrt{\frac{1}{Y_T Y_C Z_T Z_C}}
\end{aligned}
\tag{6.15}
$$

where subscripts T and C refer to tensile and compressive parameters and R, S and T represent shear strengths in the 23,13 and 12 planes, respectively. This criteria shows the element failure, and the failure mode is identified by the largest contributor to the failure criterion. For example, if the maximum contribution to the failure is because of the term associated with σ_{11}, then the mode of failure is fiber breakage or Mode 1. Mode 2 of failure is due to transverse cracking and occurs when σ_{22} or σ_{12} are dominant.

6.9 Investigation of failure in 45% of the gait cycle in nonlinear simulation of proximal femur

Non-linear hyper elastic constitutive equations discussed in chapter(5) are used to simulate the proximal femur during the 45% of the gait cycle. Material parameters and geometry morphology have additionally been described in the previous chapter.

6.9.1 Mean values of failure in maximum gait cycle

As shown in equation(6.7), the mean or expected value of the failure criteria are a function of mean value of uncertainty parameters. Distribution of the first four failure criteria from equation(6.14) in the maximum gait cycle (45% of gait cycle) are shown in figure(6.1).

As figure(6.1) indicates, the first failure or mode 1 of failure is more likely to occur in the femoral neck and head, while transverse failure caused from transverse axial or shear forces cause inter- or sub-trochanteric failure. Figure(6.2) reflects the dominant failure criteria in the polynomial failure criterion given in equation(6.15) in each element. This criterion illustrates the similar results to figure(6.1). It can be observed that mode 1 of failure is more likely to occur during the gait cycle in the head or neck, while inter- or sub-trochanteric failure is due to shear stresses. This indicates that inter- or sub-trochanteric failure is more likely to occur when falling on the side.

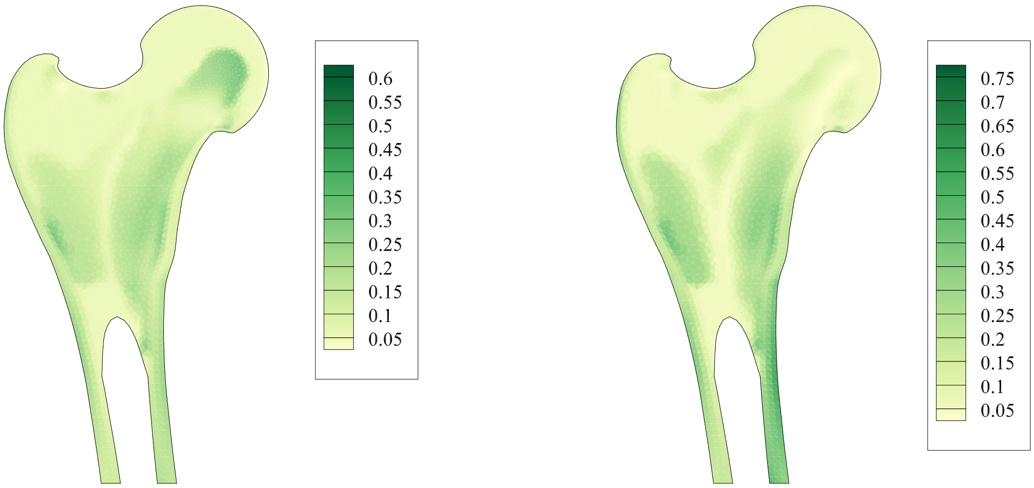

(a) First failure criterion (b) Third failure criterion

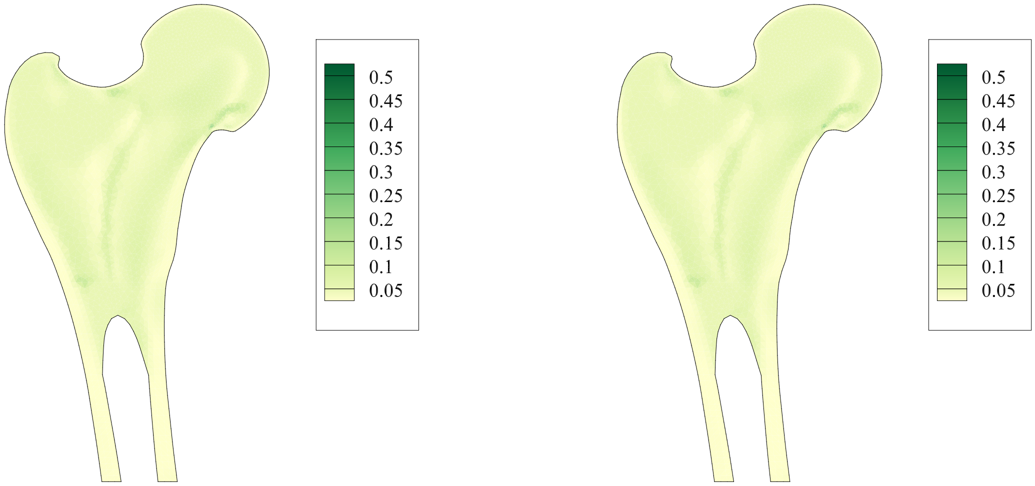

(c) Second failure criterion (d) Fourth failure criterion

Figure 6.1 Distribution of mean of failure criteria in a proximal femur section

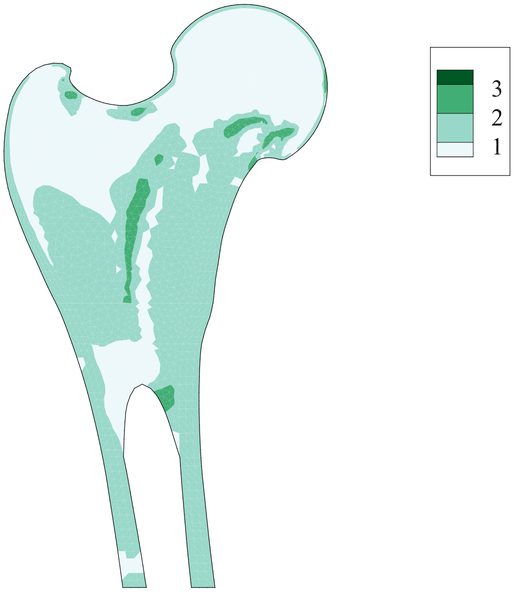

Figure 6.2 Predominant failure criteria according to fifth failure criterion

6.9.2 Sensitivity of failure to uncertain parameters

In sensitivity based methods described in section(6.4.2.3), derivative of objective functions, i.e. failure criteria in the present study, with respect to the uncertain parameters are pre-requisite. In the current work, central finite-difference is used to compute the sensitivities. The perturbation, or step size, used within the finite-difference calculation was numerically studied to investigate the effect on the accuracy of the sensitivity derivatives. Step sizes between 10e-5 and 10e-7 were selected, with no significant change in the derivatives observed. However, if the loading is further increased and, therefore, more non-linearity is introduced, a more detailed step size study is warranted.

Figures(6.3) and (6.4) illustrate the range of sensitivity of the first failure criterion with respect to the uncertainties. As discussed these uncertainties include six material properties consisting of density, the Poisson's ratio, shear modulus of cancellous and cortical layers as well as two geometric uncertainties of femoral head offset(A) and femoral head relative position(C). In a direct comparison, the impact of uncertainties on the failure criteria may be ranked from the most to least critical as density, Poisson's ratio, geometry or femoral head offset and relative position and shear modulus.

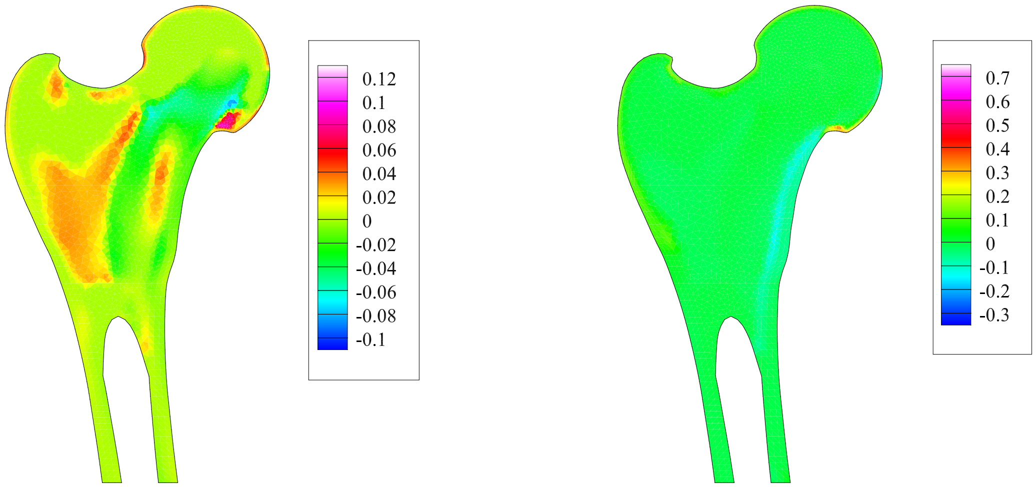

(a) Sensitivity of first failure criterion to Poisson's ratio of cancellous section

(b) Sensitivity of first failure criterion to Poisson's ratio of cortical section

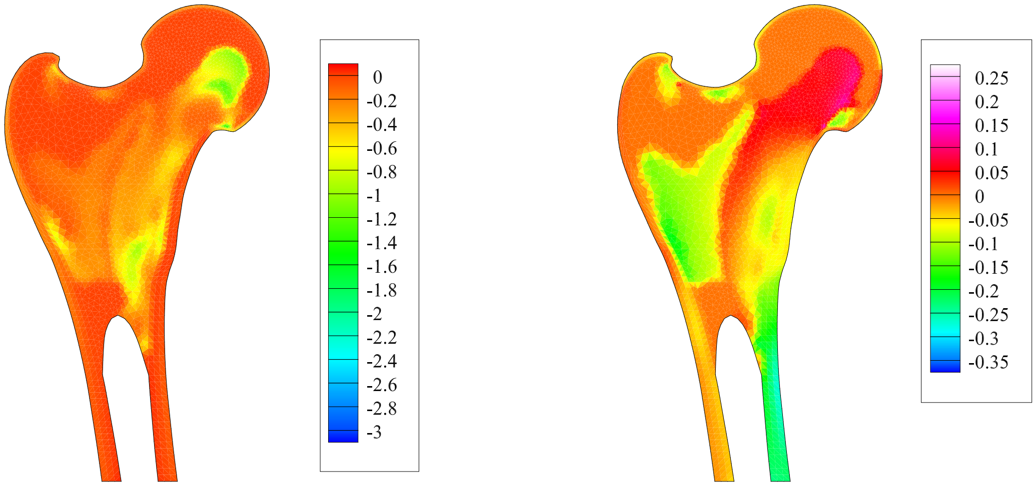

(c) Sensitivity of first failure criterion to density of cancellous section

(d) Sensitivity of first failure criterion to density of cortical section

Figure 6.3 Sensitivity of first failure criterion to Poisson's ratio and density of cancellous and cortical sections

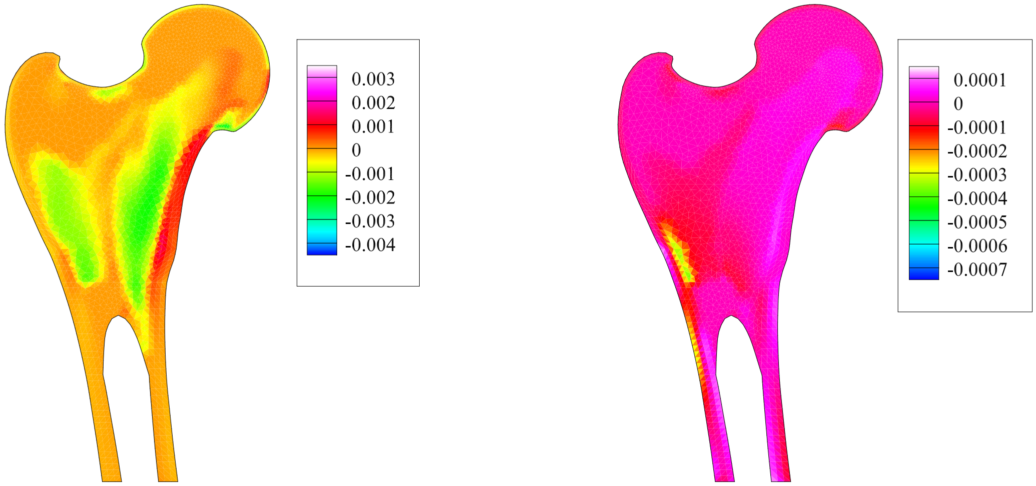

(a) Sensitivity of first failure criterion to shear modulus of cancellous section

(b) Sensitivity of first failure criterion to shear modulus of cortical section

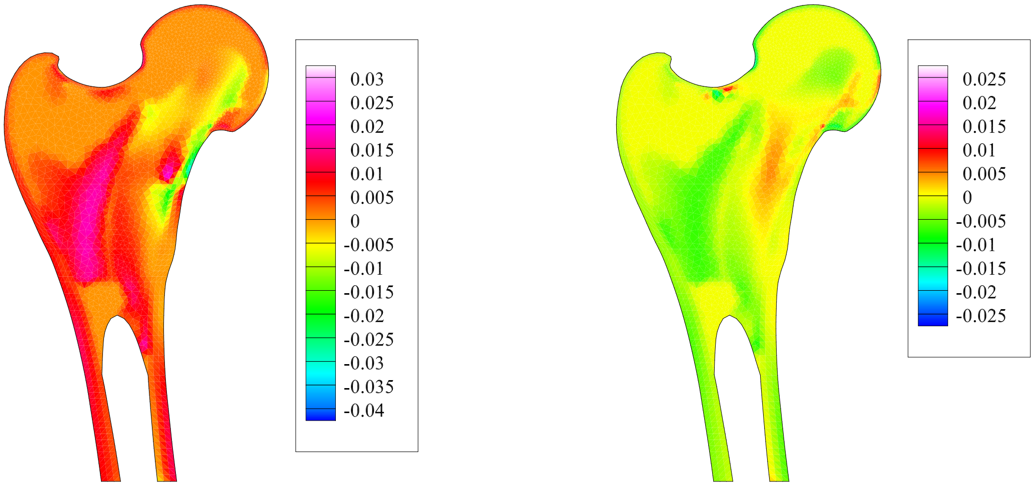

(c) Sensitivity of first failure criterion to femoral head offset (A)

(d) Sensitivity of first failure criterion to femoral head relative position (C)

Figure 6.4 Sensitivity of first failure criterion to shear modulus of cancellous and cortical sections, femoral head offset (A) and femoral head relative position (C) of figure(5.9)

6.9.3 Statistical parameters of sensitivity of failure to uncertain parameters

Following the calculation of sensitivities of failure criteria with respect to the uncertain parameters, equations(6.11) and (6.12) can be used to compute the distribution of variance, standard deviation and maximum and minimum of the failure chance. It is assumed that standard deviation or σ_{x_i} and range of uncertainties or Δx_i is 0.2. In clinical studies these values can be quantified more accurately, based on physical samples, which will produce more reliable results. Figures(6.5) to (6.10) show the distribution of standard deviation, variance, maximum and minimum of first, second and third failure criteria.

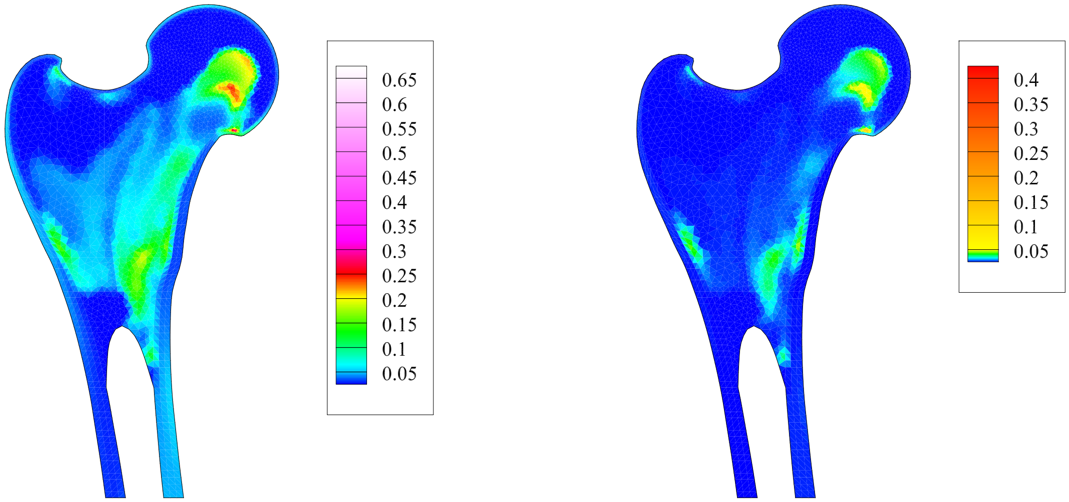

(a) Distribution of standard deviation (b) Distribution of variance

Figure 6.5 Distribution of standard deviation and variance of first failure criterion

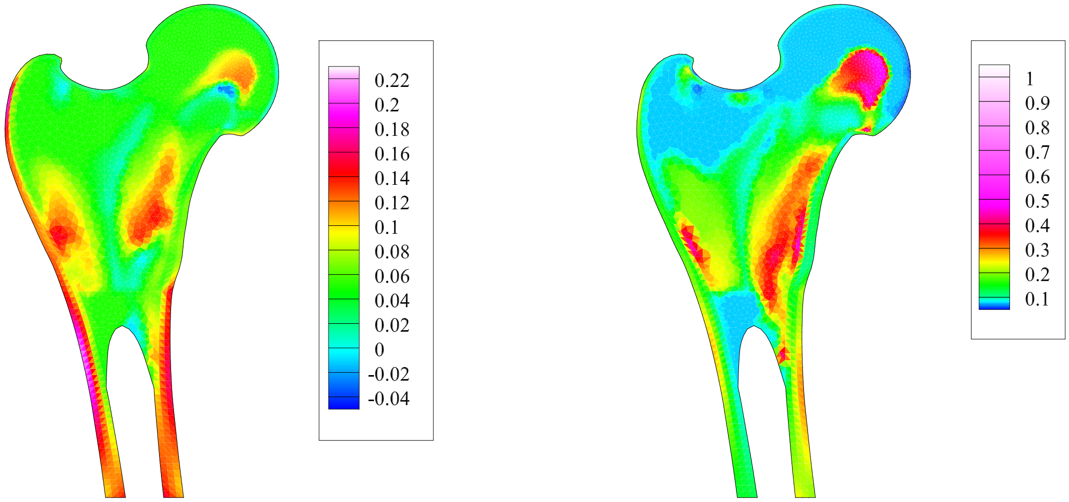

(a) Distribution of minimum values (b) Distribution of maximum values

Figure 6.6 Distribution of minimum and maximum of first failure criterion

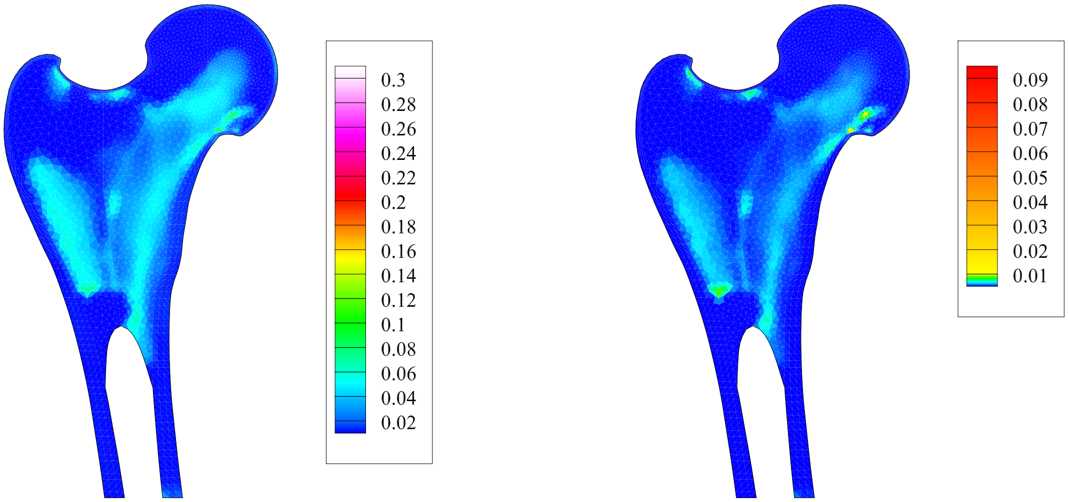

(a) Distribution of standard deviation

(b) Distribution of variance

Figure 6.7 Distribution of standard deviation and variance of second failure criterion

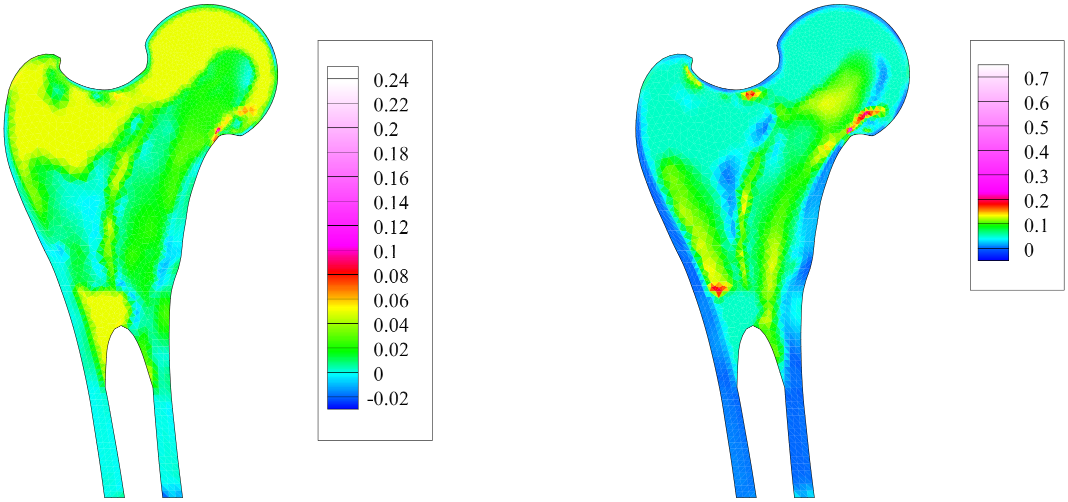

(a) Distribution of minimum values

(b) Distribution of maximum values

Figure 6.8 Distribution of minimum and maximum of second failure criterion

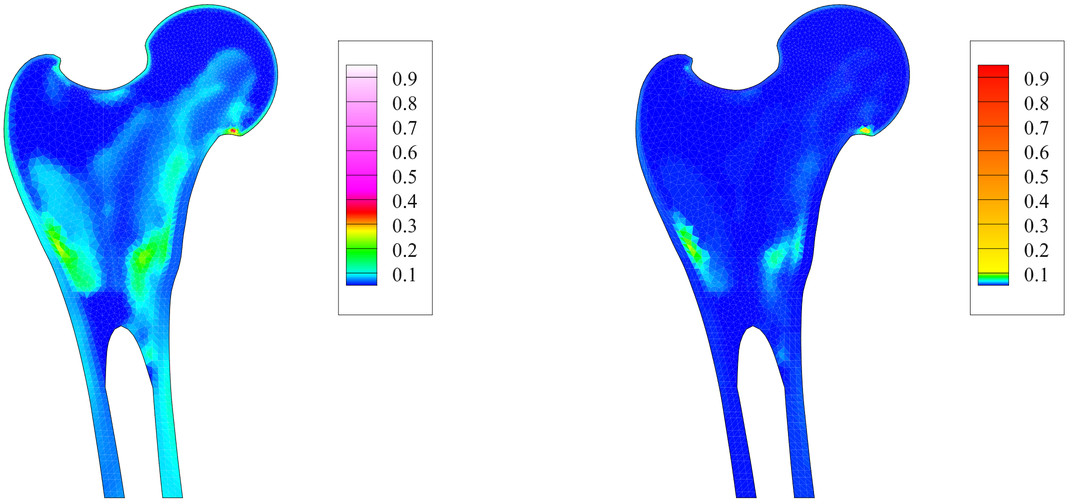

(a) Distribution of standard deviation

(b) Distribution of variance

Figure 6.9 Distribution of standard deviation and variance of third failure criterion

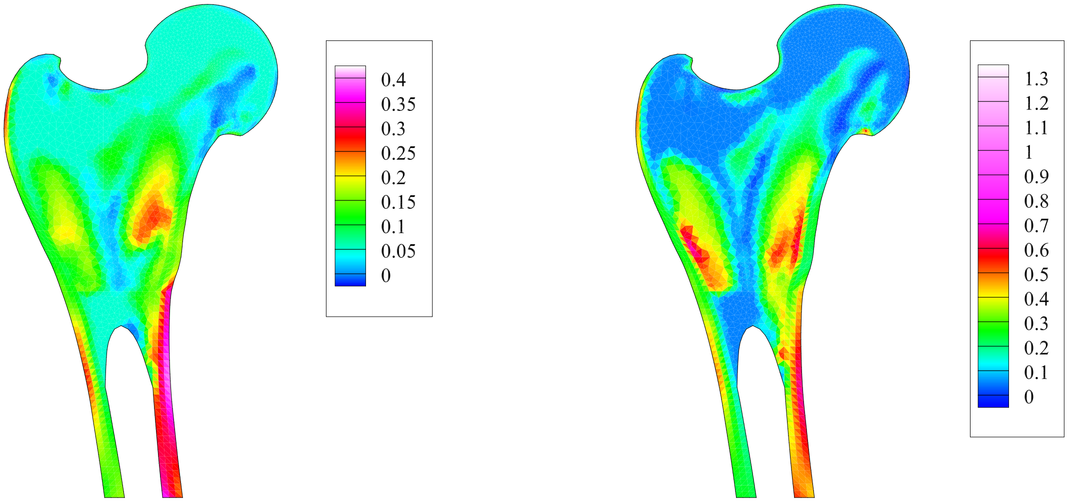

(a) Distribution of minimum values

(b) Distribution of maximum values

Figure 6.10 Distribution of minimum and maximum of third failure criterion

6.10 Uncertainty analysis of proximal femur

The final product of this study is to show the effect of uncertainties on the function of interest. To accomplish this, the proportional sensitivity analysis that shows the portion of each uncertain parameter in equation(6.13) is performed. To do that, absolute values of each uncertain parameter in equation(6.13) or $\left|\left(\frac{\partial f(\mathrm{x}_0)}{\partial x_i}\Delta x_i\right)\right|$ is divided with the summation of all of these variables. This analysis is carried out in elements with the most probability of failure regarding each failure criteria. These elements are situated in the cancellous section of the bone. The analysis are depicted in figures(6.11), (6.12) and (6.13) for first, second and third failure criteria. In these figures, subscript 1 refers to cancellous section and 2 represents the cortical part, also ν, ρ and g are the Poisson's ratio, density and shear modulus. A and C are defined in figure(5.9) and are defined as femoral head offset and femoral head relative position. As can be observed, there is a large contribution from the cancellous density in the failure criteria, subsequently the Poisson's ratio and density of the cortical section and the Poisson's ratio of the cancellous section have the largest impact. The other uncertainties are negligible, and their total effect does not exceed four percent of these dependencies.

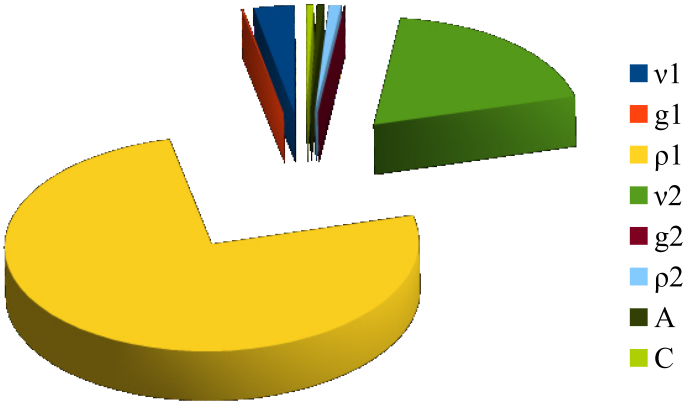

Figure 6.11 Proportional sensitivity of element with maximum first failure criterion to uncertain parameters

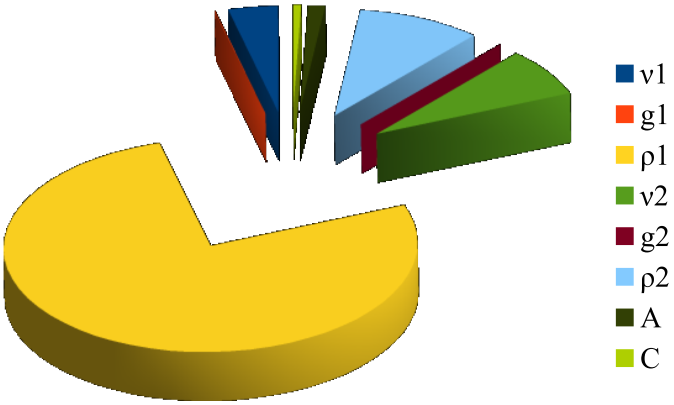

Figure 6.12 Proportional sensitivity of element with maximum second failure criterion to uncertain parameters

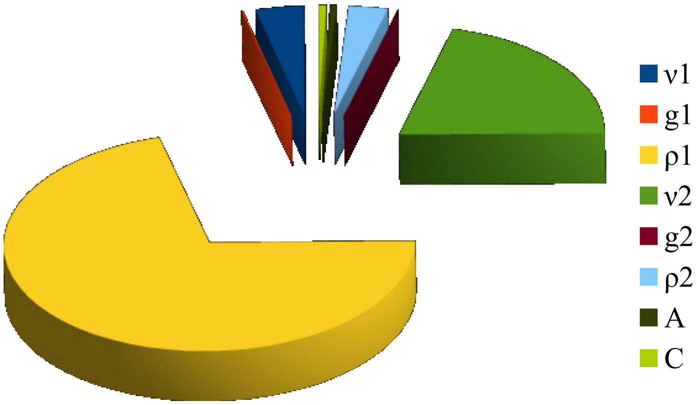

Figure 6.13 Proportional sensitivity of element with maximum third failure criterion to uncertainties

6.11 Conclusion

In this chapter, a brief description concerning uncertainties, uncertainty quantification, and the procedure of utilizing UQ in simulation results are presented. The first two applications i.e. mathematical intervals and ranking of uncertainties are post-hoc analysis that can be applied for any problem. As an example, a sensitivity based scheme for uncertainty quantification of proximal femur is investigated using the FOSM method. Mathematical interval, mean, variance and standard deviation of failure equations based on uncertain data were illustrated. Sensitivity based analysis such as ranking of the influential uncertain parameters in the failure criteria is performed thereupon.

CHAPTER 7

SUMMARY AND FUTURE WORK

A computational structural framework for the simulation of biological tissues is developed in this dissertation. Hard and soft biological tissues, may exhibit either linear or nonlinear material responses and, therefore, the resultant theory and computational implementation are presented. The simulation of linear behavior is presented in Continuous Galerkin (CG) and the Discontinuous Galerkin (DG) finite element approaches, whereas the non-linear equations are solely discussed in the CG platform. Two classes of hyper-elastic non-linear models, i.e. Saint Venant-Kirchhoff and neo-Hookean hyper-elasticity are discussed for the simulation of the non-linear problems. As an example, the hyper elastic formulation for the nonlinear, transversely isotropic behavior of soft and hard tissue is utilized for the simulation and failure analysis of the proximal femur. Both linear and nonlinear material results are compared.

Due to natural variations in biophysical properties from person to person, uncertainty quantification may be used to ascertain the impact on deterministic simulation results when assuming mean values of these properties. Thus, the uncertainty in the failure analysis due to the selected biophysical properties is examined using the First-Order Second-Moment (FOSM) method.

Additionally, within Computational Fluid Dynamics (CFD) it is often necessary to adaptively move the mesh (e.g. moving boundary simulations, shape design optimization, generation of higher-order grids near curved boundaries, etc.). In these regards, linear elasticity is commonly used for adaptation by viewing the mesh as a solid. In some cases, such as for anisotropic meshes or for extremely large boundary movement, this approach to mesh movement has experienced difficulties in producing valid grids for simulation purposes. Thus, using the developed capability, the potential benefits of utilizing isotropic nonlinear material behavior for mesh movement is additionally examined.

Although the non-linear material models are inherently formulated for the 3-dimensional problems, these relations are used in 2-dimensions in this dissertation, opening the opportunity for the usage of these relations in 3-dimensions. Also the DG formulations are implemented for the linear simulations and further implementations of DG for the non-linear elasticity is suggested.

Having found the basis for the simulation of biological tissue, working with real human sample data is suggested for more reliable simulation results. This process may require collaboration with medical laboratories to obtain more accurate material properties and in vivo computed tomography (CT) data that reflects the morphology of the tissues.

APPENDIX A

Converting elasticity tensor to matrix

This realtion shows how to transfer the elasticity tensor T to elasticity matrix M.

$$M = \frac{1}{2}\begin{bmatrix} 2\mathrm{T}_{1111} & 2\mathrm{T}_{1122} & 2\mathrm{T}_{1133} & \mathrm{T}_{1112}+\mathrm{T}_{1121} & \mathrm{T}_{1113}+\mathrm{T}_{1131} & \mathrm{T}_{1123}+\mathrm{T}_{1132} \\ & 2\mathrm{T}_{2222} & 2\mathrm{T}_{2233} & \mathrm{T}_{2212}+\mathrm{T}_{2221} & \mathrm{T}_{2213}+\mathrm{T}_{2231} & \mathrm{T}_{2223}+\mathrm{T}_{2232} \\ & & 2\mathrm{T}_{3333} & \mathrm{T}_{3312}+\mathrm{T}_{3321} & \mathrm{T}_{3313}+\mathrm{T}_{3331} & \mathrm{T}_{3323}+\mathrm{T}_{3332} \\ & & & \mathrm{T}_{1212}+\mathrm{T}_{1221} & \mathrm{T}_{1213}+\mathrm{T}_{1231} & \mathrm{T}_{1223}+\mathrm{T}_{1232} \\ & sym. & & & \mathrm{T}_{1313}+\mathrm{T}_{1331} & \mathrm{T}_{1323}+\mathrm{T}_{1332} \\ & & & & & \mathrm{T}_{2323}+\mathrm{T}_{2332} \end{bmatrix} \tag{A.1}$$

APPENDIX B

Calculation of stress tensor in equation(5.13)

```
pure function delta(i,j)
  integer, intent(in) :: i,j
  real(dp) :: delta

  if(i == j) then
     delta = 1.0
  else
     delta = 0.0
  end if

end function delta



pure function elasticity_aniso_tensor2(gamma, beta, alpha, normal, ff,
    bb, cc, JF)
  real(dp), intent(in) :: bb(2,2), cc(2,2), ff(2,2), normal(3), gamma,
      beta, alpha, JF
  real(dp) :: elasticity_aniso_tensor2(3,3,3,3)
  real(dp) :: ff3d(3,3), bb3d(3,3), cc3d(3,3), AA(3), ll, nnormal(3),
     I1, I4
  integer i, j, k, l
 do i = 1, 3
     do j = 1, 3
        ff3d(i,j) = 0.0
        bb3d(i,j) = 0.0
```

```
       cc3d(i,j) = 0.0
    end do
 end do
 ff3d(3,3) = 1.0
 bb3d(3,3) = 1.0
 cc3d(3,3) = 1.0
do i = 1, 2
    do j = 1, 2
       ff3d(i,j) = ff(i,j)
       bb3d(i,j) = bb(i,j)
       cc3d(i,j) = cc(i,j)
    end do
 end do

 ll = sqrt(normal(1)*normal(1) + normal(2)*normal(2) + normal(3)*
    normal(3))
 nnormal(1) = normal(1)/ll
 nnormal(2) = normal(2)/ll
 nnormal(3) = normal(3)/ll
 do i = 1, 3
    AA(i) = 0.0
    do j = 1, 3
       AA(i) = AA(i) + ff3d(i,j)*nnormal(j)
    end do
 end do
```

```
    I4 = AA(1)*AA(1) + AA(2)*AA(2) + AA(3)*AA(3)
    I1 = cc3d(1,1) + cc3d(2,2) + cc3d(3,3)


    do i = 1, 3
       do j = 1, 3
          do k = 1, 3
             do l = 1, 3
                elasticity_aniso_tensor2(i,j,k,l) = (8.0*gamma*AA(i)*AA(
                   j)*AA(k)*AA(l) &
                     + 4.0*beta*( AA(i)*AA(j)*delta(k,l) + delta(i,j)*AA
                        (k)*AA(l) ) &
                     - 2.0*alpha*( AA(i)*AA(l)*bb3d(j,k) + bb3d(i,k)*AA(
                        j)*AA(l) ) &
                     -4.0*beta*(I4 - 1.0)*delta(i,k)*delta(j,l) )/JF
             end do
          end do
       end do
    end do


  end function elasticity_aniso_tensor2
```

APPENDIX C

Proximal femur loading during the gait cycle

Loading conditions at 10 percent gait cycle according to the coordinate system given in the text with x pointing ventrally, y pointing laterally and z pointing proximally

	Attachment [mm]			*Force at 10% gait cycle [N]*		
Name of force	*x*	*y*	*z*	*x*	*y*	*z*
Joint contact hip	-7.93	-56.60	433.42	-510.63	665.76	-1131.89
Joint contact patella	27.71	-10.70	13.40	-123.18	65.61	-27.03
Joint contact knee						
posterio-lateral1	-5.12	20.99	0.03	0.00	0.00	718.30
anterio-medial1	2.85	-20.04	-0.14	0.00	0.00	239.43
central	0.00	0.00	0.00	-99.66	60.75	-0.01
posterio-lateral2	2.67	24.96	-0.53	-339.36	0.00	0.00
anterio-medial2	2.89	-29.98	-0.29	476.24	0.00	0.00
posterio-medial	-13.16	-16.08	-0.97	0.00	-339.36	0.00
anterio-lateral	24.92	12.84	1.58	0.00	110.34	0.00
Gluteus maximus 1	-5.72	10.25	407.51	71.13	-71.72	75.19
Gluteus maximus 2	-13.13	2.57	349.89	27.33	-58.78	75.97
Gluteus maximus 3	-11.63	10.88	392.17	36.06	-12.13	-27.76
Gluteus medius 1, 2, 3	-4.53	8.61	410.56	161.10	-118.59	149.10
Gluteus minimus 1, 2, 3	0.00	0.00	413.68	136.50	-92.37	36.25
Tensor fasciae latae	6.34	15.38	393.23	3.23	-51.09	-18.95
Piriformis	1.70	-7.48	413.66	22.71	-47.98	42.95
Obturator externus	-5.70	-11.09	407.19	0.00	0.00	0.00
Quadratus femoris	-17.75	-29.26	367.18	20.34	-22.79	32.46
Obturator internus, Gemellus superior, inferior	0.86	-10.42	410.57	11.96	-18.98	20.66
Pectineus	-16.52	-11.14	339.48	0.00	0.00	0.00
Vastus medialis	15.54	-21.93	180.83	82.90	-6.10	-259.22
Vastus intermedius	21.31	-16.80	199.26	0.00	0.00	0.00
Vastus lateralis	16.70	1.23	217.30	0.00	0.00	0.00
Gastrocnemius lateralis	-17.85	26.80	11.43	-22.75	5.96	-52.93
Gastrocnemius medialis	-24.70	-24.50	10.28	0.00	0.00	0.00
Biceps femoris, caput breve	-0.91	-1.59	204.26	-0.10	9.17	-48.81
Adductor magnus caudal	3.59	-27.65	41.85	6.44	-7.45	61.20
Adductor magnus cranial	1.42	-23.97	276.17	30.22	-49.77	63.83
Adductor minimus	7.39	-21.54	174.37	9.53	-20.47	51.26
Adductor longus	-3.18	-5.67	216.09	0.00	0.00	0.00
Adductor brevis 1	-15.62	-6.94	339.59	0.00	0.00	0.00
Adductor brevis 2	-11.37	-11.32	311.71	0.00	0.00	0.00
Psoas major, iliacus	-12.22	-33.50	370.43	0.00	0.00	0.00

Loading conditions at 30 percent gait cycle according to the coordinate system given in the text with x pointing ventrally, y pointing laterally and z pointing proximally

	Attachment [mm]			*Force at 30% gait cycle [N]*		
Name of force	*x*	*y*	*z*	*x*	*y*	*z*
Joint contact hip	-7.93	-56.60	433.42	-399.59	812.5	-1435.34
Joint contact patella	27.71	-10.70	13.40	-14.32	2.73	5.42
Joint contact knee						
posterio-lateral1	-5.12	20.99	0.03	0.00	0.00	807.00
anterio-medial1	2.85	-20.04	-0.14	0.00	0.00	269.00
central	0.00	0.00	0.00	-98.36	108.58	-0.01
posterio-lateral2	2.67	24.96	-0.53	-280.31	0.00	0.00
anterio-medial2	2.89	-29.98	-0.29	475.18	0.00	0.00
posterio-medial	-13.16	-16.08	-0.9	0.00	-280.31	0.00
anterio-lateral	24.92	12.84	1.58	0.00	-19.90	0.00
Gluteus maximus 1	-5.72	10.25	407.51	50.18	-87.92	90.85
Gluteus maximus 2	-13.13	2.57	349.89	10.05	-69.16	85.76
Gluteus maximus 3	-11.63	10.88	392.17	0.00	0.00	0.00
Gluteus medius 1, 2, 3	-4.53	8.61	410.56	128.07	-164.71	201.36
Gluteus minimus 1, 2, 3	0.00	0.00	413.68	152.51	-177.49	78.50
Tensor fasciae latae	6.34	15.38	393.23	35.26	-20.26	-26.34
Piriformis	1.70	-7.48	413.66	15.17	-77.90	68.03
Obturator externus	-5.70	-11.09	407.19	0.00	0.00	0.00
Quadratus femoris	-17.75	-29.26	367.18	0.00	0.00	0.00
Obturator internus, Gemellus superior, inferior	0.86	-10.42	410.57	12.43	-36.77	39.19
Pectineus	-16.52	-11.14	339.48	0.00	0.00	0.00
Vastus medialis	15.54	-21.93	180.83	0.00	0.00	0.00
Vastus intermedius	21.31	-16.80	199.26	0.00	0.00	0.00
Vastus lateralis	16.70	1.23	217.30	0.00	0.00	0.00
Gastrocnemius lateralis	-17.85	26.80	11.43	-126.98	21.72	-159.16
Gastrocnemius medialis	-24.70	-24.50	10.28	-6.77	2.30	-8.42
Biceps femoris, caput breve	-0.91	-1.59	204.26	-4.00	10.97	-60.16
Adductor magnus caudal	3.59	-27.65	41.85	0.00	0.00	0.00
Adductor magnus cranial	1.42	-23.97	276.17	0.00	0.00	0.00
Adductor minimus	7.39	-21.54	174.37	0.00	0.00	0.00
Adductor longus	-3.18	-5.67	216.09	0.00	0.00	0.00
Adductor brevis 1	-15.62	-6.94	339.59	0.00	0.00	0.00
Adductor brevis 2	-11.37	-11.32	311.71	0.00	0.00	0.00
Psoas major, iliacus	-12.22	-33.50	370.43	51.47	-24.37	44.32

Loading conditions at 45 percent gait cycle according to the coordinate system given in the text with x pointing ventrally, y pointing laterally and z pointing proximally

	Attachment [mm]			*Force at 30% gait cycle [N]*		
Name of force	*x*	*y*	*z*	*x*	*y*	*z*
Joint contact hip	-7.93	-56.60	433.42	-466.34	962.62	-1911.22
Joint contact patella	27.71	-10.70	13.40	-342.94	-34.41	164.95
Joint contact knee						
posterio-lateral1	-5.12	20.99	0.03	0.00	0.00	1287.38
anterio-medial1	2.85	-20.04	-0.14	0.00	0.00	429.13
central	0.00	0.00	0.00	-134.61	113.43	-0.02
posterio-lateral2	2.67	24.96	-0.53	-137.02	0.00	0.00
anterio-medial2	2.89	-29.98	-0.29	797.97	0.00	0.00
posterio-medial	-13.16	-16.08	-0.9	0.00	-137.02	0.00
anterio-lateral	24.92	12.84	1.58	0.00	-119.14	0.00
Gluteus maximus 1	-5.72	10.25	407.51	35.10	-87.87	90.95
Gluteus maximus 2	-13.13	2.57	349.89	0.08	-57.73	70.32
Gluteus maximus 3	-11.63	10.88	392.17	0.00	0.00	0.00
Gluteus medius 1, 2, 3	-4.53	8.61	410.56	111.23	-179.68	221.40
Gluteus minimus 1, 2, 3	0.00	0.00	413.68	186.22	-193.69	92.98
Tensor fasciae latae	6.34	15.38	393.23	51.42	-40.70	-40.04
Piriformis	1.70	-7.48	413.66	5.35	-77.90	67.03
Obturator externus	-5.70	-11.09	407.19	0.00	0.00	0.00
Quadratus femoris	-17.75	-29.26	367.18	0.00	0.00	0.00
Obturator internus, Gemellus superior, inferior	0.86	-10.42	410.57	7.07	-35.18	37.20
Pectineus	-16.52	-11.14	339.48	1.30	-1.01	1.12
Vastus medialis	15.54	-21.93	180.83	2.93	0.18	-8.09
Vastus intermedius	21.31	-16.80	199.26	9.13	5.01	-62.06
Vastus lateralis	16.70	1.23	217.30	69.58	-25.73	-215.72
Gastrocnemius lateralis	-17.85	26.80	11.43	-292.75	-37.74	-247.83
Gastrocnemius medialis	-24.70	-24.50	10.28	-5.71	0.04	-4.77
Biceps femoris, caput breve	-0.91	-1.59	204.26	-15.09	11.31	-90.02
Adductor magnus caudal	3.59	-27.65	41.85	0.00	0.00	0.00
Adductor magnus cranial	1.42	-23.97	276.17	0.00	0.00	0.00
Adductor minimus	7.39	-21.54	174.37	0.00	0.00	0.00
Adductor longus	-3.18	-5.67	216.09	1.86	-1.90	2.81
Adductor brevis 1	-15.62	-6.94	339.59	0.00	0.00	0.00
Adductor brevis 2	-11.37	-11.32	311.71	0.00	0.00	0.00
Psoas major, iliacus	-12.22	-33.50	370.43	115.24	-62.89	114.51

Loading conditions at 70 percent gait cycle according to the coordinate system given in the text with x pointing ventrally, y pointing laterally and z pointing proximally

	Attachment [mm]			*Force at 30% gait cycle [N]*		
Name of force	*x*	*y*	*z*	*x*	*y*	*z*
Joint contact hip	-7.93	-56.60	433.42	68.12	4.94	-47.79
Joint contact patella	27.71	-10.70	13.40	-15.95	-8.09	30.49
Joint contact knee						
posterio-lateral1	-5.12	20.99	0.03	0.00	0.00	-22.08
anterio-medial1	2.85	-20.04	-0.14	0.00	0.00	-7.36
central	0.00	0.00	0.00	-14.49	-34.95	-0.01
posterio-lateral2	2.67	24.96	-0.53	-22.84	0.00	0.00
anterio-medial2	2.89	-29.98	-0.29	56.00	0.00	0.00
posterio-medial	-13.16	-16.08	-0.9	0.00	25.71	0.00
anterio-lateral	24.92	12.84	1.58	0.00	22.84	0.00
Gluteus maximus 1	-5.72	10.25	407.51	0.00	0.00	0.00
Gluteus maximus 2	-13.13	2.57	349.89	0.20	-0.45	0.55
Gluteus maximus 3	-11.63	10.88	392.17	0.00	0.00	0.00
Gluteus medius 1, 2, 3	-4.53	8.61	410.56	3.57	-4.89	5.53
Gluteus minimus 1, 2, 3	0.00	0.00	413.68	22.29	28.45	7.97
Tensor fasciae latae	6.34	15.38	393.23	6.43	-3.00	-5.58
Piriformis	1.70	-7.48	413.66	2.89	-6.42	5.44
Obturator externus	-5.70	-11.09	407.19	0.55	-0.41	0.07
Quadratus femoris	-17.75	-29.26	367.18	0.00	0.00	0.00
Obturator internus, Gemellus superior, inferior	0.86	-10.42	410.57	2.15	-3.92	4.14
Pectineus	-16.52	-11.14	339.48	2.38	-1.06	1.32
Vastus medialis	15.54	-21.93	180.83	0.00	0.00	0.00
Vastus intermedius	21.31	-16.80	199.26	0.00	0.00	0.00
Vastus lateralis	16.70	1.23	217.30	0.00	0.00	0.00
Gastrocnemius lateralis	-17.85	26.80	11.43	-19.04	-3.33	-4.72
Gastrocnemius medialis	-24.70	-24.50	10.28	0.00	0.00	0.00
Biceps femoris, caput breve	-0.91	-1.59	204.26	-0.64	0.17	-2.21
Adductor magnus caudal	3.59	-27.65	41.85	0.00	0.00	0.00
Adductor magnus cranial	1.42	-23.97	276.17	0.00	0.00	0.00
Adductor minimus	7.39	-21.54	174.37	0.00	0.00	0.00
Adductor longus	-3.18	-5.67	216.09	11.45	-7.62	13.25
Adductor brevis 1	-15.62	-6.94	339.59	0.40	-0.29	0.26
Adductor brevis 2	-11.37	-11.32	311.71	0.37	-0.28	0.31
Psoas major, iliacus	-12.22	-33.50	370.43	32.41	-7.41	20.43

REFERENCES

[1] Bonet, J. and Wood, R. D., *Nonlinear Continuum Mechanics for Finite Element Analysis, 2nd Edition*, Cambridge University Press, 1997.

[2] Miehe, C., "Aspects of the formulation and finite element implementation of large strain isotropic elasticity," *International Journal of Numerical Methods in Engineering*, Vol. 37, 1994, pp. 1981–2004.

[3] Bonet, J. and Burton, A., "A simple orthotropic, transversely isotropic hyperelastic constitutive equation for large strain computations," *Computer Methods in Applied Mechanics and Engineering*, Vol. 162, 1998, pp. 151–164.

[4] Newman, J. C., Anderson, W. K., and Whitfield, D. L., "Multidisciplinary sensitivity derivatives using complex variables," *Mississippi State University Report MSSU-COE-ERC-98-08*, 1998.

[5] Saad, Y. and Schultz, M., "GMRES: A generalized minimal residual algorithm for solving nonsymmetric linear systems," *SIAM Journal on Scientific and Statistical Computing*, Vol. 7, 1986, pp. 856–869.

[6] Arnold, D., Brezzi, F., Cockburn, B., and Marini, D., "Unified analysis of discontinuous Galerkin methods for elliptic problems," *SIAM Journal of Numerical Analysis*, Vol. 39, 2001, pp. 1749–1779.

[7] Hesthaven, J. and Warburton, T., *Nodal Discontinuous Galerkin Methods*, Springer, 2008.

[8] Reed, W. and Hill, T., "Triangular mesh methods for the neutron transport equation," *Technical Report LA-UR-73-479, Los Alamos Scientific Laboratory*, 1973.

[9] Douglas, J. and Dupont, T., "Interior penalty procedures for elliptic and parabolic Galerkin methods," *Computing Methods in Applied Sciences*, 1976, pp. 207–216.

[10] Arnold, D., "An interior penalty finite element method with discontinuous elements," *SIAM Journal of Numerical Analysis*, Vol. 19, 1982, pp. 742–760.

[11] Engel, G., Garikipati, K., Hughes, T., Larson, M., Mazzei, L., and Taylor, R., "Continuous/discontinuous finite element approximations of fourth-order elliptic problems in structural and continuum mechanics with applications to thin beams and plates, and strain gradient elasticity," *Computer Methods in Applied Mechanics and Engineering*, Vol. 191, 2002, pp. 3669–3750.

[12] Güzey, S., Stolarski, H., Cockburn, B., and Tamma, K., "Design and development of a discontinuous Galerkin method for shells," *Computer Methods in Applied Mechanics and Engineering*, Vol. 195, 2006, pp. 3528–3548.

[13] Lew, A., Neff, P., Sulsky, D., and Ortiz, M., "Optimal BV estimates for a discontinuous Galerkin method for linear elasticity," *Applied Mathematics Research Express*, Vol. 3, 2004, pp. 73–106.

[14] Hansbo, P. and Larson, M., "Discontinuous finite element methods for incompressible and nearly incompressible elasticity by use of Nitsche's method," *Computer Methods in Applied Mechanics and Engineering*, Vol. 191, 2002, pp. 1895–1908.

[15] Eyck, A. T. and Lew, A., "Discontinuous Galerkin methods for non-linear elasticity," *International Journal for Numerical Methods in Engineering*, Vol. 67, 2006, pp. 1204–1243.

[16] Mergheim, J., Kuhl, E., and Steinmann, P., "A hybrid discontinuous Galerkin/interface method for the computational modelling of failure," *Communications in Numerical Methods in Engineering*, Vol. 20, 2011, pp. 1–45.

[17] Becker, G. and Noels, L., "A full-discontinuous Galerkin formulation of non-linear Kirchhoff-Love shells: elasto-plastic finite deformations, parallel computation and fracture applications," *International Journal for Numerical Methods in Engineering*, Vol. 93, 2013, pp. 80–117.

[18] Levy, S., Seagraves, A., Molinari, J., and Radovitzky, R., "Discontinuous Galerkin method applied to fragmentation of heterogeneous materials," *9E Colloque National En Calcul Des Structures, Giens,France*, 2009.

[19] Nitsche, J., "Über ein Variationsprinzip zur Lösung Dirichlet-Problemen bei Verwendung von Teilräumen die keinen Randbedingungen unteworfen sind," *Abhandlungen aus dem Mathematischen Seminar der Universität Hamburg*, Vol. 36, 1971, pp. 9–15.

[20] Babuška, I., "The finite element method with penalty," *Mathematics of Computation*, Vol. 27, 1973, pp. 221–228.

[21] Baker, G., "Finite element methods for elliptic equations using nonconforming elements," *Mathematics of Computation*, Vol. 31, 1997, pp. 45–59.

[22] Babuška, I. and Zlámal, M., "Nonconforming elements in the finite element method with penalty," *SIAM Journal of Numerical Analysis*, Vol. 10, 1973, pp. 863–875.

[23] Arnold, D., Brezzi, F., Cockburn, B., and Marini, D., "Discontinuous Galerkin methods for elliptic problems," *Lecture Notes in Computational Science and Engineering*, Vol. 11, 2000, pp. 89–101.

[24] Bassi, F. and Rebay, S., "A high-order accurate discontinuous finite element method for the numerical solution of the compressible Navier-Stokes equations," *Journal of Computational Physics*, Vol. 131, 1997, pp. 267–278.

[25] Cockburn, B. and Shu, C., "The local discontinuous Galerkin finite element method for convection-diffusion systems," *SIAM Journal of Numerical Analysis*, Vol. 35, 1998, pp. 2440–2463.

[26] Brezzi, F., Marini, D., Pietra, P., and Russo, A., "Discontinuous finite elements for diffusion problems," *Atti Convegno in onore di F. Brioschi, Istituto Lombardo, Accademia di Scienze e Lettere*, 1997, pp. 197–217.

[27] Brezzi, F., Marini, D., Pietra, P., and Russo, A., "Discontinuous Galerkin approximations for elliptic problems," *Numerical Methods for Partial Differential Equations*, Vol. 16, 2000, pp. 365–378.

[28] Baumann, C. and Oden, J., "A discontinuous hp finite element method for convection-diffusion problems," *Computer Methods in Applied Mechanics and Engineering*, Vol. 175, 1999, pp. 311–41.

[29] Bassi, F., Rebay, S., Mariotti, G., Pedinotti, S., and Savini., M., "A high-order accurate discontinuous finite element method for inviscid and viscous turbomachinery flows," *In Proceedings of 2nd European Conference on Turbomachinery, Fluid Dynamics and Thermodynamics, Antwerpen, Belgium*, 1997, pp. 99–108.

[30] Riviére, B., Wheeler, M., and Girault, V., "Improved energy estimates for interior penalty, constrained and discontinuous Galerkin methods for elliptic problems I," *Computers & Geosciences*, Vol. 3, 1999, pp. 337–360.

[31] Cockburn, B., Karniadakis, G., and Shu, C.-W., "The evolution of discontinuous Galerkin methods," *Lecture Notes in Computational Science and Engineering*, Vol. 11, 2000, pp. 3–50.

[32] Castillo, P., "Performance of discontinuous Galerkin methods for elliptic PDEs," *SIAM Journal on Scientific Computing Archive*, Vol. 24, 2002, pp. 524–547.

[33] Epshteyn, Y. and Riviére, B., "Estimation of penalty parameters for symmetric interior penalty Galerkin methods," *Journal of Computational and Applied Mathematics*, Vol. 206, 2007, pp. 843–872.

[34] Wheeler, M. F., "An elliptic collocation-finite element method with interior penalties," *SIAM Journal of Numerical Analysis*, Vol. 15, 1978, pp. 152–161.

[35] Shahbazi, K., "An explicit expression for the penalty parameter of the interior penalty method," *Journal of Computational Physics*, Vol. 205, 2005, pp. 401–407.

[36] Baumann, C. and Oden, J., "A discontinuous hp finite element method for the Navier-Stokes equations," *10th. International Conference on Finite Element in Fluids*, Vol. 175, 1998, pp. 311–41.

[37] Sun, S. and Wheeler, M., “Symmetric and nonsymmetric discontinuous Galerkin methods for reactive transport in porous media,” *SIAM Journal of Numerical Analysis*, Vol. 43, 2005, pp. 195–219.

[38] Liu, W., Chang, H., Chen, J.-S., and Belytschko, T., “Arbitrary Lagrangian Eulerian Petrov-Galerkin finite elements for nonlinear continua,” *Computer Methods in Applied Mechanics and Engineering*, Vol. 68, 1988, pp. 259–310.

[39] Liu, W., Chen, J.-S., Belytschko, T., and Zhang, Y., “Adaptive ALE finite elements with particular reference to external work rate on frictional interface,” *Computer Methods in Applied Mechanics and Engineering*, Vol. 93, 1991, pp. 189–216.

[40] Batina, J. T., “Unsteady Euler airfoil solutions using unstructured dynamic meshes,” *American Institute of Aeronautics and Astronautics Journal*, Vol. 28, 1990, pp. 1381–1388.

[41] Cavallo, P. A., Hosangadi, A., Lee, R. A., and Dash, S. M., “Dynamic unstructured grid methodology with application to aero/propulsive flowfield s,” *American Institute of Aeronautics and Astronautics Journal*, 2002, pp. 1997–2310.

[42] Yang, Z. and Mavriplis, D. J., “A mesh deformation strategy optimized by the adjoint method on unstructured meshes,” *American Institute of Aeronautics and Astronautics Journal*, 2007, pp. 2885–2896.

[43] Stein, K., Tezduyar, T., and Benney, R., “Mesh moving techniques for fluid-structure interactions with large displacements,” *Journal of Applied Mechanics*, Vol. 70, 2003, pp. 58–63.

[44] Persson, P. and Peraire, J., “Curved mesh generation and mesh refinement using Lagrangian solid mechanics,” *47th American Institute of Aeronautics and Astronautics Aerospace Sciences Meeting*, 2009.

[45] Moxey, D., Ekelschot, D., Keskin, Ü., Sherwin, S., and Peiró, J., “High-order curvilinear meshing using a thermo-elastic analogy,” *Computer-Aided Design*, Vol. 72, 2016, pp. 130–139.

[46] Bathe, K. J., Ramm, E., and Wilson, E. L., “Finite element formulations for large deformation dynamic analysis,” *International Journal for Numerical Methods in Engineering*, Vol. 9, 1974, pp. 353–386.

[47] Shamsaei, B. and Boroomand, B., “Exponential basis functions in solution of laminated structures,” *Composite Structures*, Vol. 93, 2011, pp. 2010–2019.

[48] Szilard, R., *Theories and Applications of Plate Analysis*, John Wiley & Sons, 2004.

[49] Burge, R., Dawson-Hughes, B., Solomon, D. H., Wong, J. B., King, A., and Tosteson, A., “Incidence and economic burden of osteoporosis-related fractures in the United States, 2005-2025,” *Journal of Bone and Mineral Research*, Vol. 22, 2007, pp. 465–475.

[50] Fox, K. M., Magaziner, J., Hebel, J. R., Kenzora, J. E., and Kashner, T. M., "Intertrochanteric versus femoral neck fractures: differential characteristics, treatment, and sequelae," *Journals of Gerontology Series A: Biological Sciences and Medical Sciences*, Vol. 54, 1999, pp. 635–640.

[51] Zuckerman, J. D., "Hip fracture," *The New England Journal of Medicine*, Vol. 334, 1996, pp. 1519–1525.

[52] Antonio, T. S., Ciaccia, M., Müller-Karger, C., and Casanova, E., "Orientation of orthotropic material properties in a femur FE model: A method based on the principal stresses directions," *Journals of Gerontology Series A: Biological Sciences and Medical Sciences*, Vol. 34, 2012, pp. 914–918.

[53] Boehler, J. P., *Mechanical behavior of the anisotropic solids*, Nijhoff, 1982.

[54] Vel, S. S. and Batra, R. C., "The generalized plane strain deformations of thick anisotropic composite laminated plates," *International Journal of Solids and Structures*, Vol. 37, 2000, pp. 715–733.

[55] Carrera, E., "C_z^0 requirements-models for the two dimensional analysis of multilayered structures," *Composite Structures*, Vol. 37, 1997, pp. 373–384.

[56] Rawal, B. R., Ribeiro, R., Malhotra, R., and Bhatnagar, N., "Anthropometric measurements to design best-fit femoral stem for the Indian population," *Indian Journal of Orthopaedics*, Vol. 46, 2012, pp. 46–53.

[57] de Sousa, E. B., Fernandes, R. M. P., Mathias, M. B., Rodrigues, M. R., Ambram, A. J., and Babinski, M. A., "Morphometric study of the proximal femur extremity in Brazilians," *International Journal of Morphology*, Vol. 28, 2010, pp. 835–840.

[58] Sen, R. K., Tripathy, S. K., Kumar, R., Kumar, A., Dhatt, S., Dhillon, M. S., Nagi, O., and Gulati, M., "Proximal femoral medullary canal diameters in Indians: correlation between anatomic, radiographic, and computed tomographic measurements," *Journal of Orthopaedic Surgery*, Vol. 18, 2010, pp. 189–194.

[59] Malo, M. K. H., Rohrbach, D., Isaksson, H., Töyräs, J., Jurvelin, J. S., Tamminen, I. S., Kröger, H., and Raum, K., "Longitudinal elastic properties and porosity of cortical bone tissue vary with age in human proximal femur," *Bone*, Vol. 53, 2013, pp. 451–458.

[60] Duda, G. N., *Influence of muscle forces on the internal loading in the femur during gait*, Ph.D. thesis, Technical University Hamburg-Harburg, Hamburg, 1996.

[61] Carter, D. R., Fyhrie, D. P., and RT., R. T. W., "Trabecular bone density and loading history: regulation of connective tissue biology by mechanical energy," *Journal of Biomechanics*, Vol. 20, 1987, pp. 785–794.

[62] Beaupré, G. S., Orr, T. E., and Carter, D. R., "An approach for time-dependent bone modeling and remodeling-theoretical development," *Journal of Orthopaedic Research*, Vol. 8, 1990, pp. 651–661.

[63] Ntuli, T. M., *Apoptosis and Medicine*, InTech, 2012.

[64] Martens, R., Audekercke, R. V., DeMeester, P. D. P., and Mulier, J. C., "The mechanical characteristics of cancellous bone at the upper femoral region," *Journal of Biomechanics*, Vol. 16, 1983, pp. 971–983.

[65] Goulet, R. W., Goldstein, S. A., Ciarelli, M. J., Kuhn, J. L., Brown, M. B., and Feldkamp, L. A., "The relationship between the structural and orthogonal compressive properties of trabecular bone," *Journal of Biomechanics*, Vol. 27, 1994, pp. 375–389.

[66] Rudy, D. J., Deuerling, J. M., Orias, A. A. E., and Roeder, R. K., "Anatomic variation in the elastic inhomogeneity and anisotropy of human femoral cortical bone tissue is consistent across multiple donors," *Journal of Biomechanics*, Vol. 44, 2011, pp. 1817–1820.

[67] Wirtz, D. C., Schiffers, N., Pandorf, T., Radermacher, K., Weichert, D., and Forst, R., "Critical evaluation of known bone material properties to realize anisotropic FE-simulation of the proximal femur," *Journal of Biomechanics*, Vol. 33, 2000, pp. 1325–1330.

[68] Knauss, P., "Material properties and strength behaviour of the compact bone tissue at the coxal human femur," *Biomedical Technology*, Vol. 26, 1981, pp. 311–315.

[69] Halawa, M., Lee, A. J. C., Ling, R. S. M., and Vangala, S. S., "The shear strength of trabecular bone from the femur, and some factors affecting the shear strength of the cement-bone interface," *Archives of Orthopaedic and Traumatic Surgery*, Vol. 92, 1978, pp. 19–30.

[70] Miller, Z., M, M. F., and Arcan, M., "Trabecular bone adaptation with an orthotropic material model," *Journal of Biomechanics*, Vol. 35, 2002, pp. 247–256.

[71] Oberkampf, W., DeLand, S., Rutherford, B., Diegert, K., and Alvin, K., "A new methodology for the estimation of total uncertainty in computational simulation," *American Institute of Aeronautics and Astronautics*, Vol. 1612, 1999, pp. 3061–3083.

[72] Yao, W., Chen, X., a, W. L., v. Tooren, M., and Guo, J., "Review of uncertainty-based multidisciplinary design optimization methods for aerospace vehicles," *Progress in Aerospace Sciences*, Vol. 47, 2011, pp. 450–479.

[73] Roache, P. J., "Quantification of uncertainty in computational fluid dynamics," *Annual Review of Fluid Mechanics*, Vol. 29, 1997, pp. 123–160.

[74] Isukapalli, S. S., Roy, A., and Georgopoulos, P. G., "Stochastic response surface methods (srsms) for uncertainty propagation: Application to environmental and biological systems." *Risk Analysis*, Vol. 18, 1998, pp. 351–363.

[75] Wang, Q., *Uncertainty quantification for unsteady fluid flow using adjoint-based approaches*, Ph.D. thesis, Stanford university, 2008.

[76] Hoffman, F. and Hammonds, J., “Propagation of uncertainty in risk assessments: the need to distinguish between uncertainty due to lack of knowledge and uncertainty due to variability,” *Risk Analysis*, Vol. 14, 1994, pp. 707–712.

[77] Wiener, N., “The homogeneous chaos,” *American Journal of Mathematics*, Vol. 60, 1938, pp. 897–936.

[78] Wille, H., Ruess, M., Rank, E., and Yosibash, Z., “Uncertainty quantification for personalized analyses of human proximal femurs,” *Journal of Biomechanic*, Vol. 49, 2016, pp. 520–527.

[79] Landau, D. P. and Binder, K. A., *A guide to Monte Carlo simulations in statistical physics*, New York: Cambridge University Press, 2005.

[80] Barry, T., “Recommendations on the testing and use of pseudo-random number generators used in Monte Carlo analysis for risk assessment,” *Risk Analysis*, Vol. 16, 1996, pp. 93–105.

[81] Khuri, A. I. and Mukhopadhyay, S., “Response surface methodology,” *Wiley Interdisciplinary Reviews: Computational Statistics*, Vol. 2, 2010, pp. 128–149.

[82] Helton, J. C. and Davis, F. J., “Latin hypercube sampling and the Propagation of uncertainty in analyses of complex systems,” *SAND2001-0417. Sandia National Laboratories, Albuquerque, New Mexico*, 2002.

[83] Engel, D. W., Liebetrau, A. M., Jarman, K. D., Ferryman, T. A., Scheibe, T. D., and Didier, B. T., “An iterative uncertainty assessment technique for environmental modeling. Paper presented at the ties and accuracy,” *6th International Symposium on Spatial Accuracy Assessment, Portland, Maine*, 2004.

[84] Putko, M. M., Newman, P. A., Taylor, A. C., and Green, L. L., “Approach for uncertainty propagation and robust design in CFD using sensitivity derivatives,” *Proceedings: 15th American Institute of Aeronautics and Astronautics Computational Fluid Dynamics Conference 2001-2528*, 2001.

[85] Hou, G. J., Taylor, A. C., and M.Korivi, V., “Discrete shape sensitivity equations for aerodynamic problems,” *International Journal of Numerical Methods in Engineering*, Vol. 37, 1994, pp. 2251–2266.

[86] Coleman, H. W. and Steele, W. G., *Experimentation and uncertainty analysis for engineers*, John Wiley and Sons, 1999.

[87] Alefeld, G. and Herzberger, J., *Introduction to interval computations*, Academic Press, 1993.

[88] Ingram-Cotton, J. B., Hecht, M. J., Duphily, R. J., M., M. Z., Hiramoto, T., and O’connor, C., “Reliability program requirements for space systems,” *Aerospace Report NO.TOR-2007(8583)-6889, US The Aerospace Corporation*, 2007.

[89] Taddei, F., Martelli, S., Reggiani, B., Cristofolini, L., and Viceconti, M., "Finite-element modeling of bones from CT data: sensitivity to geometry and material uncertainties," *IEEE Transactions on Biomedical Engineering*, Vol. 53, 2006, pp. 2194–2200.

[90] Laz, P. J., Stowe, J. Q., Baldwin, M. A., Petrella, A. J., and Rullkoetter, P. J., "Incorporating uncertainty in mechanical properties for finite element-based evaluation of bone mechanics," *Journal of Biomechanics*, Vol. 40, 2007, pp. 2831–2836.

[91] Eberle, S., Göttlinger, M., and Augat, P., "Individual density-elasticity relationships improve accuracy of subject-specific finite element models of human femurs," *Journal of Biomechanics*, Vol. 46, 2013, pp. 2152–2157.

[92] Praemer, A., Furner, S., and Rice, D. P., "Musculoskeletal conditions in the United States," *American Academy of Orthopaedic Surgeons, Chicago, IL.*, 1992.

[93] Keyak, J. H., Rossi, S. A., Jones, K. A., and Skinner, H. B., "Prediction of femoral fracture load using automated finite element modeling," *Journal of Biomechanic*, Vol. 31, 1998, pp. 125–133.

[94] Reddy, Y. S. N., Moorthy, C. M. D., and Reddy, J. N., "Non-linear progressive failure analysis of laminated composite plates," *International Journal of Non-Linear Mechanics*, Vol. 30, 1995, pp. 629–649.

VITA

Behrouz Shamsaei was born on March 21st, 1983 in Isfahan, Iran. He was accepted in National Organization for Development of Exceptional Talents (NODET) for his middle and high school in mathematics and physics in Isfahan. He studied bachelor and master of science in civil and structures in Isfahan University of Technology, Iran. Before joining the university of Tennessee at Chattanooga, he worked in national civil projects for four years in Iran. He awarded his PhD degree in Computational Engineering from the University of Tennessee at Chattanooga in August 2016.